Reactivity of Boron Nitride and Carbon Based Nanomaterials with Water : a study from first principles

Benoit Grosjean

Reactivity of Boron Nitride and Carbon Based Nanomaterials With Water
A study from first principles

by Benoit Grosjean

**Supervised by Marie-Laure Bocquet
and Rodolphe Vuilleumier**

IANNUZZI Marcella, Privatdozentin, University of Zürich, Reviewer
FLEURAT-LESSARD Paul, Professor, Université de Bourgogne, Reviewer
BENOIT Magali, Research Director, CNRS, Examinator
SALANNE Mathieu, Professor, Sorbonne Université, Examinator
RADENOVIC Aleksandra, Associate Professor, École Fédérale Polytechnique de Lausanne, Examinator
BOCQUET Marie-Laure, Research Director, CNRS, Supervisor
VUILLEUMIER Rodolphe, Professor, Sorbonne Université, Supervisor

Contents

Acknowledgements

Abbreviations

AC: Armchair

AIMD: Ab Initio Molecular Dynamics

BN: Boron Nitride

BNNT: Boron Nitride Nanotube

CNT: Carbon Nanotube

CSVR: Canonical Sampling through Velocity Rescaling

DFT: Density Functional Theory

G: Graphene

GDS: Gibbs Dividing Surface

GGA: Generalized Gradient Approximation

hBN: hexagonal Boron Nitride

LDA: Local Density Approximation

LEEM: Low Energy Electron Microscopy

MD: Molecular Dynamics

MSD: Mean Square Displacement

PBC: Periodic Boundary Conditions

PBE: Perdew Burke and Erzenhof functional

PMF: Potential of Mean Force

RMSE: Root Mean Square Error

STM: Scanning Tunnelling Microscopy

vdW: van der Waals

VASP: Vienna Ab-initio Simulation Package

VMD: Visual Molecular Dynamics

WHAM: Weighted Histogram Analysis Method

ZZ: Zigzag

Chapter 1

Introduction

1.1 Carbon and Boron Nitride Based Nanomaterials

The solid state of carbon and its isoelectronic counterpart boron nitride (BN) exhibit the peculiarity of sharing the same allotropic forms. Their most common phases are the diamond and graphitic ones, consisting of respectively sp^3 and sp^2 hybridised atoms. In the latter case a honeycomb network is formed by a hexagonal arrangement of the nuclei distributed in monoatomic sheets superposed in a stacked structure whose cohesion is assured by van der Waals (vdW) forces (see Fig. 1.1a and b). An amazingly rich variety of sp^2 allotropes has been isolated over the past forty years starting from spherical arrangements into so-called buckminsterfullerenes[1] to single-layer hexagonal sheets[2] and cylindrical shapes named nanotubes[3, 4] (see Fig. 1.1c and d).

Each of these sp^2 forms have raised colossal attention as illustrated by the 1996 and the 2010 Nobel Prizes respectively in Chemistry and Physics awarded for the isolation of the first fullerene[1] and graphene, the monoatomic hexagonal carbon layer first isolated by exfoliating a graphite crystal solely 5 years prior to the consecration of its discoverers[2]. The enormous interest did not only originate from the synthesis of unconventional chemical objects but also from their unexpected intrinsic properties linked to their structure at the nanoscale. The attention was indeed followed by tremendous research focus aiming at a better understanding and a tailoring of these nanomaterials for a seemingly boundless myriad of applications. Graphene is emblematic of this phenomenon, with countless

1
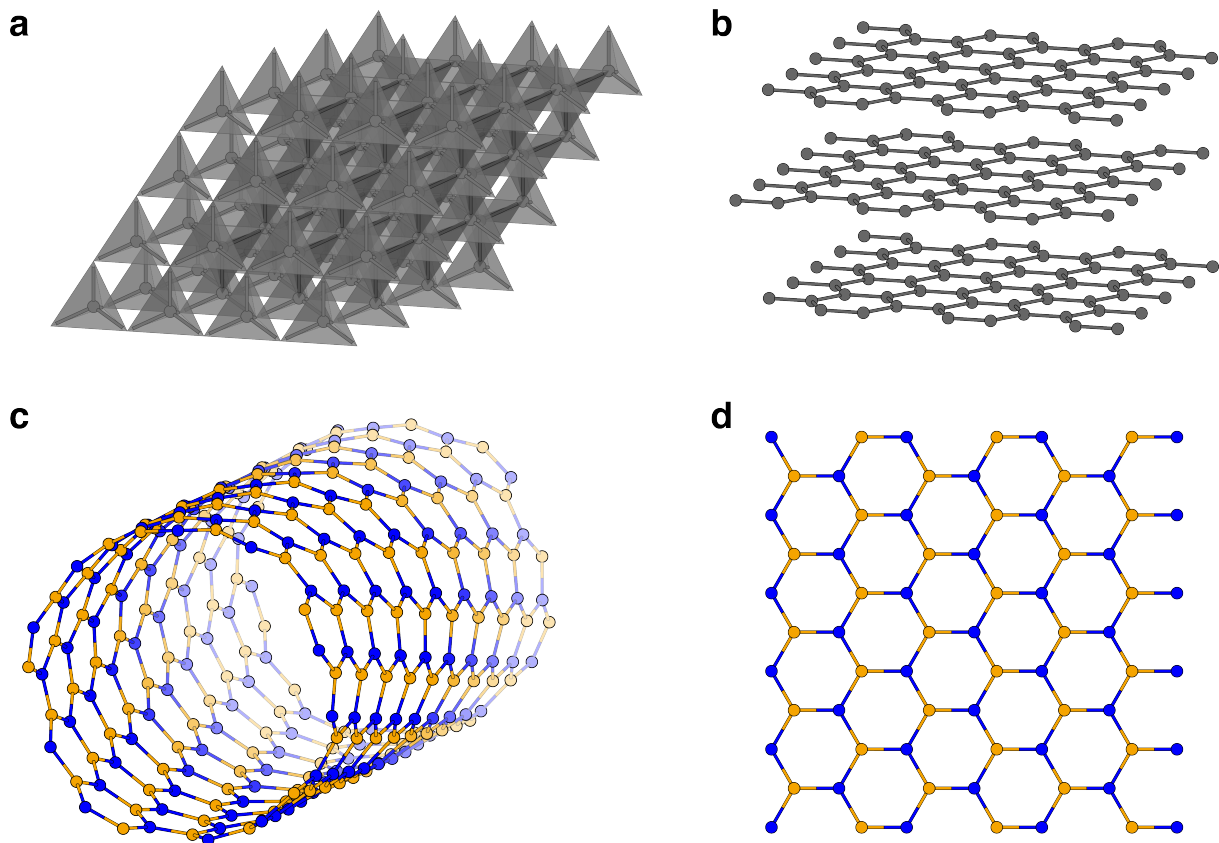
Figure 1.1: Different allotropic forms of carbon (a, b) and boron nitride (c, d): diamond (a), graphite (b), nanotube (c) and single monoatomic layer (d). Boron, carbon and nitrogen atoms are respectively represented in orange, grey and blue.

and ubiquitous envisioned applications from cell growth substrate to electronics, optics, mechanical reinforcement, catalysis and many more[5–8], amounting to more than 15 thousand patents (according to the Dimensions web service while counting patents with the keyword "graphene" in title). An eloquent illustration is to compare the yearly number of scientific publications on graphene since its isolation set side by side with other widely studied materials, for instance the ubiquitous silica and another industrially widely spread oxide, TiO_2 (see Fig. 1.2), with various applications including in the deep and high tech sectors (more than 186 000 patents according to the Dimensions web service).

Works presented here focus on the single-layer and nanotube forms, namely graphene, 2D hexagonal boron nitride (hBN), carbon nanotube (CNT) and boron nitride nanotube (BNNT). These terms hide a diversity of materials that vary for instance in crystal size, chirality, defectiveness and local chemical structure depending on treatments received and the chosen synthesis route. In fact these nanomaterials can be obtained via different meth-
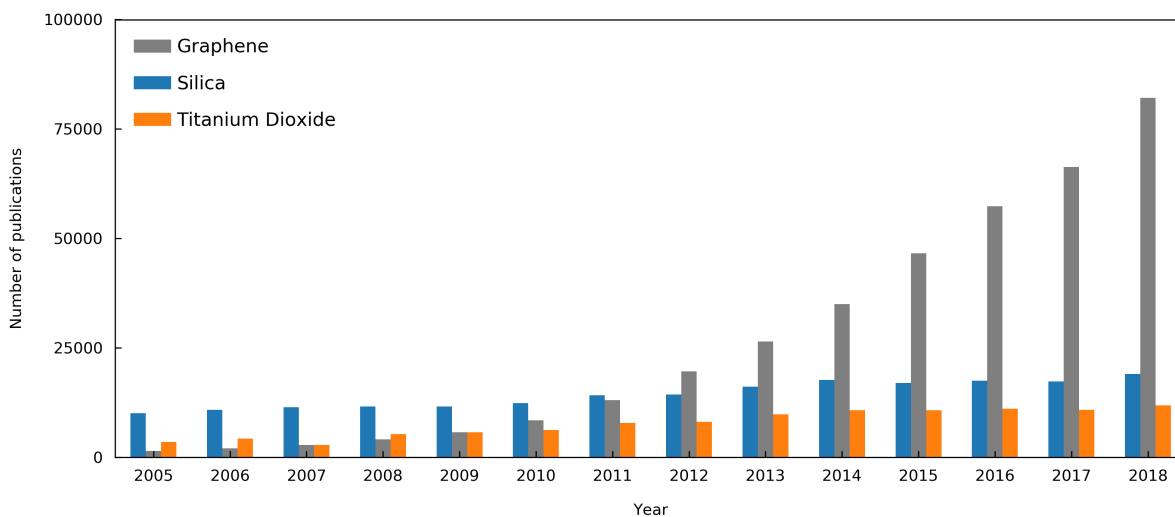
Figure 1.2: Yearly number of publications including in title or abstract the keywords "graphene" (grey), "silica" or "SiO$_2$" (blue) and "TiO$_2$" or "titanium dioxide" or "anatase" or "rutile" (orange). The count of publications was performed using the Dimensions web service.

ods such as mechanical exfoliation of multi-layered materials, chemical vapour deposition, arc discharge, or successive oxidation, dispersion and reduction to cite a few[7, 9, 10].

A common point shared by graphene, hBN, CNT and BNNT is that common knowledge claims their chemical inertness[11, 12]. They are accordingly the object of statements that often remain unreferenced explicitly stating their "chemical inertness" in a myriad of publications[13–28]. This picture remains even though examples of covalent functionalization nowadays fill entire textbooks[8, 9, 29–33], in direct contradiction with the idea of a lack of chemical reactivity. As pointed out by Al Hamdani *et al.*[34], what is implied in the aforementioned statements is a chemical inertness in mild conditions, typically when these nanomaterials are in contact with water under ambient conditions - corresponding to the utilisation conditions of many envisioned applications. In other words, the consensus to date is that nothing significant occurs to BN and carbon based nanomaterials unless they are placed under strong chemical stress.

1.2   What Recent Nanofluidic Experiments Revealed

The reactivity of BN and carbon based nanomaterials with aqueous electrolyte at ambient conditions was recently assessed thanks to nanofluidic transport measurements. Indeed giant unexpected surface charging was highlighted in ionic transport measurement of KCl through multiwall BNNTs[35] and CNTs[36] (multiwall nanotubes being the cylindrical equivalent of graphitic materials), with a surface charge reaching up to 1 $C.m^{-2}$ for BNNT and 0.01 to 0.1 $C.m^{-2}$ for CNT. To our knowledge this is one to three orders of magnitude larger than other reported values including the cases of solids known for exhibiting large surface charges such as silica and clays[37, 38].

More precisely the nanofluidic experimental setup schematised in Fig. 1.3 consists in a single nanotube placed in a SiN mineral membrane separating two reservoirs containing KCl solutions in water at a pH controlled by addition of HCl or KOH. The device is completed by two Ag electrodes placed on both sides of the membrane. To generate a flow through the nanotube one can either apply a gradient of pressure, salinity or electric potential between the two reservoirs. The surface charges were revealed by ionic conductance measurements consisting in measuring for different electrolyte concentration the electric current intensity while applying an electric potential across the setup. At low salinity the conductance of the BNNTs reaches a non-zero plateau while it decreases following a law to the power 1/3 for the CNTs, instead of rapidly diminishing to zero. Values of surface charges were then indirectly derived from the ionic conductance using a Poisson-Nernst-Planck model adapted to the tube geometry while including a Poisson-Boltzmann scheme for the charge equilibration within the interface between the tube and the solution[35, 36].

The surface charge was identified to be negative and strongly depending on pH with highest charges obtained in alkaline conditions. This led the experimentalists to suggest hydroxide adsorption as a source of surface charge for both materials although the differing salinity dependence pointed to different mechanisms and strengths of adsorption.

This conjecture remains however unsupported up to now in terms of the chemical reactivity of these materials and the fundamental origin of this surface charging remains mysteri-
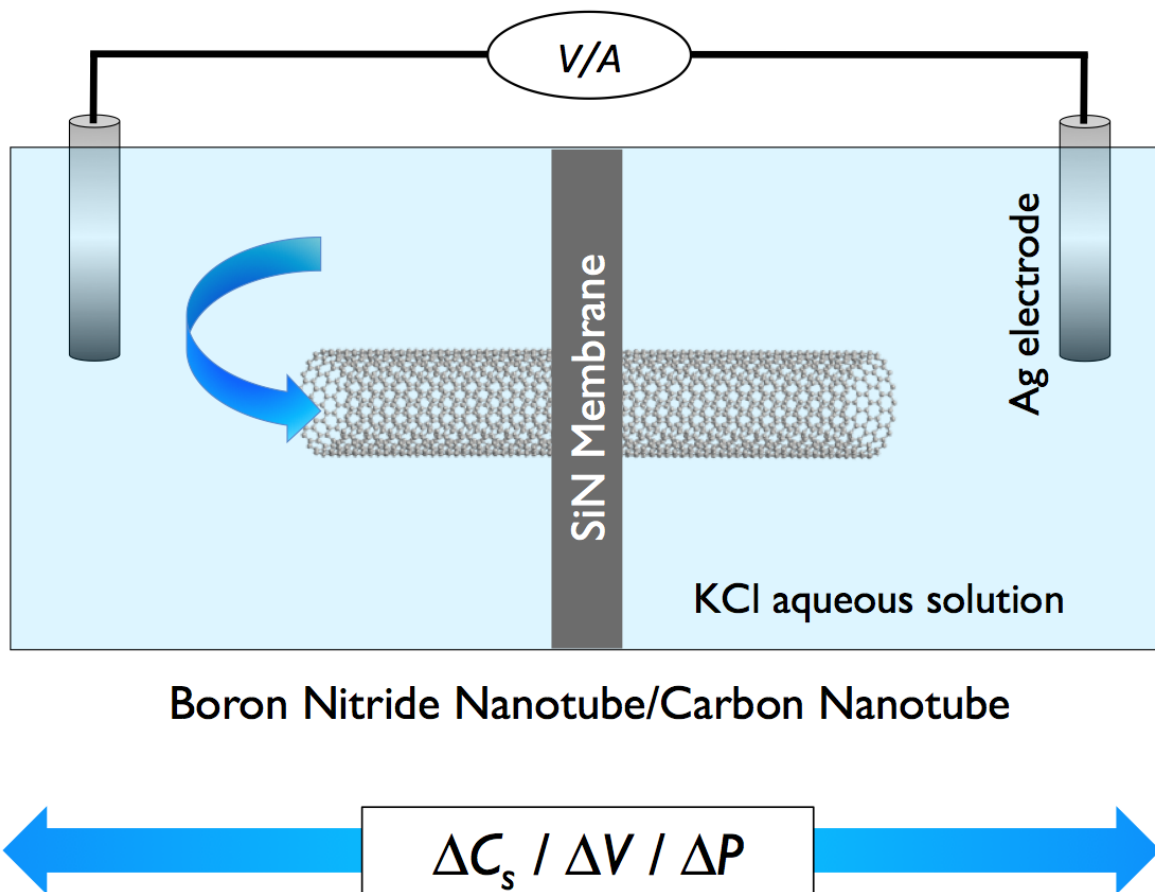
Figure 1.3: Schematic representation of the nanofluidic experimental device: the flow of a KCl solution through a single nanotube embedded in a mineral SiN membrane separating two reservoirs is induced by applying a gradient of either pressure ΔP, electric potential ΔV or salinity ΔC_s while the electric tension V or current intensity A is measured using Ag electrodes in contact with the electrolyte.

ous. In fact recent experimental works showed the covalent hydroxylation of BN but solely in drastic conditions while the BNNTs exhibit charges as high as 0.2 C.m^{-2} in water at neutral pH and room conditions. Functionalization by OH$^-$ is indeed typically achieved either via reduction[39–41] or reaction with oxidative reagents (H_2O_2[42], oxygen radical[43]) or via fluorination[44]. Other methods relying to harsh treatments such as high or elevated temperatures[45–48], hydrothermal conditions[49], ultrasonication[26, 50], ball milling[51–53] or use of plasma[54] have also been developed, ultimately leading to more than a dozen protocols for the hydroxylation of BN that have been recently reviewed[55, 56], with to our knowledge no example of mild conditions[26, 39–54, 57].

Beyond the scope of accomplishing better understanding of the chemical properties of BN and carbon based nanomaterials, the nanofluidic experiments that revealed gigantic

charging of nanotubes carry the hope of applications far from trivial. In fact they led to several patents that aim at taking advantage of this excess potential for desalination purposes or production of renewable energy exploiting salinity gradients via diffusio-osmosis flows[58, 59]. The latter power source known as blue energy presents several promising aspects including a yield possibly higher than standard photovoltaic cells, without the use of highly polluting heavy and rare-earth elements or silicon crystals necessitating extreme production energy costs[60–62].

1.3   Water: a Mixture of H_2O, OH^- and H_3O^+

From the chemical point of view, water is a very particular entity, prone to non-covalent yet partially quantum interactions of significant strength with its surroundings, therefore at times able to strongly modify its environment properties via the formation of hydrogen bonds. On the side of covalent chemistry, as an amphiphilic species, H_2O statistically coexists with its two self-ions, hydroxide OH^- and hydronium H_3O^+, both highly reactive in many respects, possibly leading to hydroxylation, protonation or deprotonation of various compounds. Thus, the common name of water designates in fact a mixture of H_2O, OH^- and H_3O^+ in various proportions. Considered as such, water is therefore a potentially reactive medium prone to exchange hydroxides and protons with chemical species in contact.

Contrary to other protic solvents water is also the stage of the peculiar Grotthuss mechanism through which proton hole and proton excess rapidly transfer via the hydrogen bond network, OH^- and H_3O^+ thus hopping from H_2O to H_2O. Because of it, the acid and base counterparts of H_2O gain further complexity and lay far from the picture of a point charge surrounded by a somewhat spherical layer of solvating molecules with which they interact through electrostatics. Contrary to the standard picture of a solvated ion in water, OH^- and H_3O^+ are indeed transient species existing in a distribution of continuous protonation states along the path drawn by Grotthuss proton transfers. This distribution includes the Zündel and $H_3O_2^-$ ions[63–67] depicted in Fig. 1.4 that correspond to configurations in which a proton is shared between two oxygen centres.
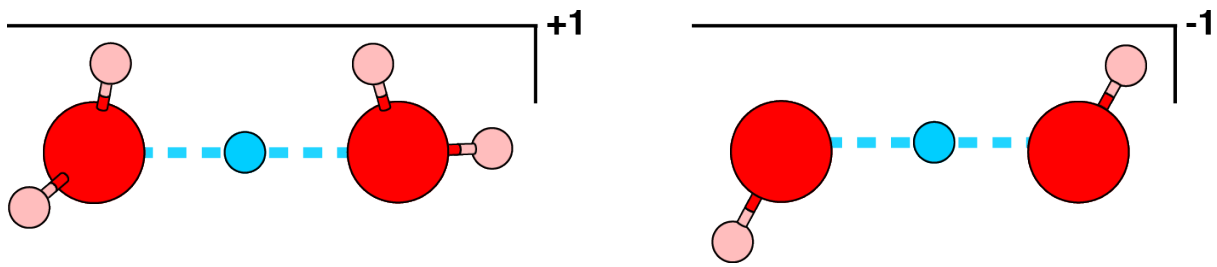
Figure 1.4: Schematic representation of the transient complexes known as the Zündel ion (left) and $H_3O_2^-$ (right) respectively corresponding to a proton excess and hole shared between two oxygen centres. Hydrogen and oxygen atoms are represented respectively in pink and red while the shared proton is in cyan.

Although the Grotthuss mechanism leads both hydronium and hydroxide to diffuse faster than H_2O, the cation does so at higher rates, with diffusion coefficients of respectively about 360.10^{-9} and 200.10^{-9} $m^2.s-1$[68, 69]. The reason for that is a fundamental difference in their solvation in water. The aqueous hydronium is in fact giving three hydrogen bonds to surrounding water molecules, forming a triangular pyramid solely lacking a fourth hydrogen bond partner to form a tetrahedral environment resembling the organisation of bulk H_2O. Proton transfer occurs upon cleavage of one hydrogen bond and modest reorientation of a water molecule in the second solvation shell of the hydronium, with the newly formed H_2O thus finding itself in a solvation geometry close to its preferential one[63, 70–73], to the contrary of the case of the proton hole. Indeed, OH^- prefers to be surrounded by four hydrogen bond donor H_2O arranged in a square planar pattern, with an additional hydrogen bond partner only dynamically present in the solvation shell yielding a square pyramid geometry. Hence when proton transfer occurs both the newly formed OH^- and H_2O are in a solvation situation considerably differing from their preferred ones, leading to immediate return of the proton hole on its starting centre. The square planar complex is found stable on the picosecond scale, until it starts to be deformed towards a tetrahedral geometry, triggering rapid exploration of the water network by series of proton hopes until the negative charge finds itself once more in a stable square planar environment[63–67]. Thus while the solvation shell of the cation is consistent with the arrangement of H_2O molecules, enabling it to continuously hop from oxygen to oxygen, the diffusion of its anionic counterpart is hampered by disruption of its Grotthuss transfer chains when forming inactive configurations. Beyond the effect

on their mobility, this difference between OH^- and H_3O^+ illustrates that non-covalent changes in their environment can have a primordial importance for their reactivity.

1.4   Molecular Simulations

Although the complexity of liquid water can be tackled experimentally in its bulk situation, this is not necessarily the case for interfacial regions or under particular confinement circumstances. Notably in the case at stake one wishes to study the interface formed by water confined in nanotubes with radii down to 3.5 nm in order to rationalise experimental measurements performed on a single tube (typically 500-1500 nm in length) embedded into a mineral membrane in contact with several millilitres of saline water held in centimetre-thick polymer walls. The setup itself makes it hard to access the interface for tools of choice such as sum frequency spectroscopy that furthermore would necessitate averaging of their signal over an extremely restricted area formed by the interface between water and a single tube.

In contrast simulations can model rather indifferently a large variety of systems at the molecular time and length scales regardless of practical difficulties that can be encountered experimentally. The interface of water with carbon surfaces have for instance successfully been modeled, scarcely by first-principles methods[74, 75] and principally by classical ones[76–83] with in particular a study of the behaviour of OH^- at hydrated graphenic surfaces simulated at the semi-empirical level using classical dynamics[84]. However this level of modeling cannot correctly describe OH^- and H_3O^+ in water as it excludes formation and breaking of chemical bonds which occur on the picosecond time scale for these systems. Beyond the aqueous medium the absence of dynamic covalent chemistry in classical models prohibits the study of reactions at the surface of carbon and BN based nanomaterials such as hydroxilation of sp^2 surface atoms. In fact to model such reactivity one has to rely to computationally expensive theories derived from first-principles. In particular the density functional theory (DFT) has been successfully applied to model the reactivity of hBN and graphene with molecular hydrogen, a single H_2O and its radical fragments[34, 85]. Notably the cost of first principles methods is beyond comparison with

that of classical methods which allow for the modelling of greater system sizes and time scales, establishing the possibility to represent an electrolytic interface in contact with a reasonable bulk that most importantly includes all the richness of ions and counter ions that form double electric layers[86]. However with interfacial systems that lack any sort of experimental insight at the molecular scale as in the situation presently discussed, there is no guarantee that the classical descriptions validated and parametrised on bulk phases stand reasonable for the modeling of the interface. While some electrolyte/carbon nanomaterial interfaces benefit from molecular characterisation such as X-ray scattering[87] or nuclear magnetic resonance[88] allowing for adequate tuning of classical models to yield correct representations, it is necessary in other cases to rely on *a posteriori* validations of the empirical model by comparison to experimentally accessible non-molecular properties, for instance electrochemical quantities as obtained by cyclic voltammetry characterising nanoporous carbon electrodes[83, 89–91]. However, nanofluidic systems consisting of nanotubes or 2D materials are very recent and remain arduous to molecularly characterise. Simulation methods based on first-principles overcome the parametrisation issue by relying to frameworks baring greater transferability. Nanofluidic interfaces have lately been successfully described by *ab initio* based molecular dynamics (AIMD) where the nuclei are classically propagated according to forces obtained from first-principles electronic structure theory[74, 75, 92, 93].

1.5 Aim of the Present Work

The first aim of the present work is to provide a conclusive molecular explanation as to the charging mechanism of BNNTs and CNTs in water in room conditions and as to the origin of the clear behavioural charging disparities between the two twin materials. Starting from the hypothesis of a differential adsorption of hydroxides as inferred by the sign and the pH dependency of the experimental surface charges, we extend our simulation study to other BN and carbon based nanomaterials to confront the question of their chemical inertness with respect to aqueous media.

Using DFT and AIMD within slightly differing frameworks and protocols described in

chapter 2, we first show by means of static DFT and an implicit solvation scheme that flat surface models, hBN and graphene, can respectively form and not form a chemical bond with OH^- (see chapter 3)[94]. Extending the study of the same systems with an AIMD description including explicit representation of the water solvent we then show that the anion can physisorb on both interfaces, with implications on transport phenomena beyond providing a proof for the envisioned charging mechanism (see chapter 4)[95]. Building on the experience and insight gained on these systems we take advantage of the predictive power of molecular simulations to extend our study to planar junctions of hBN and graphene sheets, revealing extremely reactive interaction with water molecules leading to their dissociation (see chapter 5)[96]. Finally, moving beyond pristine flat surfaces and the hydroxide in on-going works, we model the interfaces formed by water with CNTs and BNNTS and with defected hBN sheets as well as the reactivity of H_3O^+ in the vicinity of the materials, predicting a physisorption of the cation similar to that of its anionic counterpart (see chapter 6)[97]. As a whole our first-principles simulations together with experiments form a body of evidence showing the far from negligible reactivity of even neutral water with BN and carbon based nanomaterials in room conditions, thus dismantling the consensual picture of chemical inertness associated with these systems.

A large part of the works described here have either been published in scientific journals or is currently undergoing the submission process[94–97].

Chapter 2

Methods

2.1 Ab Initio Simulations

Although full classical molecular dynamics (MD) and hybrid QM/MM simulations are far less costly than *ab initio* techniques, allowing for the simulation of larger systems on longer time scales, they are not necessarily the tool of choice to study certain interfacial phenomena. In fact classical models require the optimisation of numerous parameters on which forcefields depend, and this is generally carried out by fitting experimental measurements corresponding to the bulk, as the interface is harder to probe. To cite a representative example, in 2002 B. Guillot performed a comprehensive comparison of the then available water models and selected seven properties to do so, all of them corresponding to the bulk situation: density, heat of vaporisation, self diffusion coefficient, radial distribution functions, temperature of maximum density, dielectric constant and critical parameters[98]. Yet chemical properties can drastically evolve at the approach of an interface and models highly parametric to resemble the bulk may miss key descriptions of the interfacial region. In particular aqueous interfaces are subtle to model as the water hydrogen network is prone to strong modifications as compared to the bulk liquid situation[99]. Notably, compiling their solid experience of classical simulations of the water/nanoporous graphene interface for reverse osmosis applications[100–102], Cohen-Tanugi *et al.* pointed out in a review article on the description of such systems the issue of defining a proper interaction potential for aqueous ions and the solid surfaces, calling for quantum chemical

studies[80]. Indeed, contrary to empirical and semi-empirical models, *ab initio* methods such as Density Functional Theory (DFT) based ones depend on parametrisations much less system-specific (functional, pseudo-potentials, basis sets, dispersion corrections etc.) which provide the freedom of satisfactorily simulating an interface and a bulk within the same framework, *i.e.* without additional parametrisation. One major advantage of classical and hybrid techniques is the possibility of modeling simultaneously an interface and a proper corresponding bulk while DFT calculations of reasonable cost allow computation of the chemical medium only up to a few nanometers away from the interface, often before bulk properties are met. However in the present case, it is precisely the nanoscale that is at stake with water confined in nanotubes with radius as small as 3.5 nm[36]. Additionally even the most complex classical simulation protocols can only provide a rough and pre-determined reactivity at the interface. Since they yield decent description of chemical reactivity on length scales corresponding to the experimental phenomena we intent to resolve, DFT based methods were chosen for the whole present study, via static calculations and *ab initio* molecular dynamics (AIMD). Static DFT was primarily used to derive the total energy of a given atomic configuration while AIMD runs were mainly computed to obtain free energy profiles, diffusion coefficients and dynamic picture of the chemical systems.

2.2   General Computational Details

Typical input files used for the present study are provided in appendix.

2.2.1   Simulation Cells

Since the tremendous surface charging of tubes is observed over a large range of radii (3.5 to 40 nm)[35, 36], we postulated at first that curvature had little impact on the interaction between the hydroxide and the BN or carbon surfaces, as it was verified later on (see section 3.4 of chapter 3). The nanotubes were accordingly modelled as flat hexagonal layers containing 60 atoms in an orthorhombic cell under periodic boundary conditions
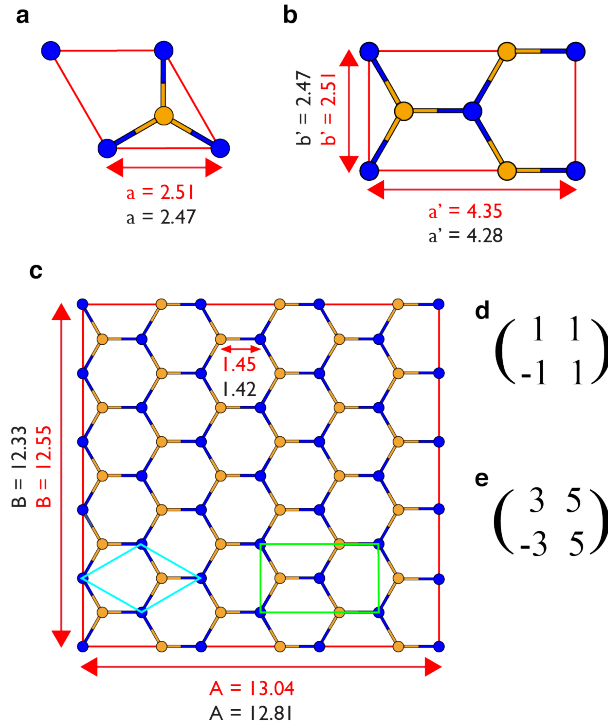
Figure 2.1: a) BN hexagonal primitive unit cell. b) BN orthorhombic primitive unit cell. c) BN supercell adopted for simulations. Distances expressed in Å are written in red (black) for the case of BN (graphene). Boron and nitrogen atoms are respectively displayed in orange and blue. e) is the matrix to transform cell a) into cell b) and e) the matrix to obtain cell c) from cell a).

(PBC) with a 13.04 × 12.55 Å² hBN (12.83 × 12.35 Å² graphene) surface (see Fig. 2.1) separated by 15 or 21 Å of vacuum, implicit or explicit water. The B-N and C-C bond lengths were optimised as to minimise the energy of the simulation cell within the static DFT framework, yielding distances of respectively 1.43 Å and 1.45 Å in agreement with previous calculations with the same method[103]. All the solid parts of simulation cells were generated by exploiting crystallographic constructions using the interface builder of the Quantum Wise Virtual NanoLab software[104]. This is the case for single and multi flat-layers as well as for nanotubes. The latter are labelled by geometry using standard nomenclature referring to the circumferential vector $\boldsymbol{C} = n\boldsymbol{a} + m\boldsymbol{b}$ where $\boldsymbol{a}$ and $\boldsymbol{b}$ are the unit vectors of the primitive hexagonal lattice of the sheet[105]. $\boldsymbol{C}$ represents the relative position of two atoms of the starting hexagonal sheet yielding the nanotube with desired geometry when they are rolled onto each other. A tube can therefore be labelled by the integer pair (n, m) which contains the information of the radius $r = |\boldsymbol{C}|/2\pi$, the chirality and the subsequent metallicity in the case of carbon nanotubes (CNT). $(n, 0)$, (n, n) and

$(n, m \neq n \neq 0)$ respectively designate zigzag, armchair and chiral nanotubes.

Both static DFT and AIMD simulations of charged systems were performed by applying a uniformly charged neutralising background instead of including a counterion in the simulation.

2.2.2   Static DFT

Static DFT calculations were performed with the Vienna Ab Initio Simulation Package (VASP) in its version 5.4.1 [106–108]. As it was proven to correctly describe hBN and graphene[109] as well as their interaction with water[74, 110, 111] the generalised gradient approximation (GGA) of the exchange-correlation energy as proposed by Perdew, Burke and Ernzerhof (PBE) was used for the flat single layers[112]. When van der Waals (vdW) corrections were found necessary the vdW inclusive optB86b-vdW functional[113, 114] was preferred. The wave functions have been expanded in a plane wave basis set with an energy cutoff of 800 eV. The common cutoff for hybrid interfaces is 400 eV in vacuum and taking twice the value is requested for sake of precision when dealing with the implicit solvent scheme described below. To avoid spurious interactions between periodic images as well as between an adsorbate in its reference state far from the surface and the surface, single layers were separated by 15 Å of vacuum or implicit water. The adsorbate was placed at the half of this distance away from the surface to derive an energy reference. The electronic cores were described by the projector augmented wave method[115]. The smearing technique using a Gaussian broadening was applied to achieve electronic convergence. k-point sampling was limited to the gamma point. All values used to derive adsorption energies in chapter 3 (chapter 5) were obtained on configurations which geometry was fully optimised with atomic forces lower than 0.02 (0.05) eV/Å. To mimic the effect of solvent in this first approach, solvation energies were evaluated within the joint density functional theory framework as implemented into VASP by Mathew and Hennig[116] and successfully used recently[117–120]. In this technique the dielectric permittivity of the medium is defined as a functional of the electronic density. Indeed dielectric permittivity approaches asymptotically the bulk water value at P = 1 bar, $\epsilon_b = 78.4$, in the region

where the electronic density is lower than $\rho_{cut} = 0.0025$ Å^3 (the default cutoff charge density), while $\epsilon_b = 1$ in the region when the electronic density is high (inside the slab treated as a solute). The cavitation energies which account for the solvent contributions are calculated with a surface tension parameter of 0.525 meV/Å^2.

Within the framework described above, a single converged DFT cycle for a ~ 250 electrons system costed approximately 10 to 20 hCPU. Different parameters of the DFT simulations, in particular the size of the planewaves basis set were chosen upon convergence of the simulation cell total energy along with computational cost considerations (see Fig. 2.2).
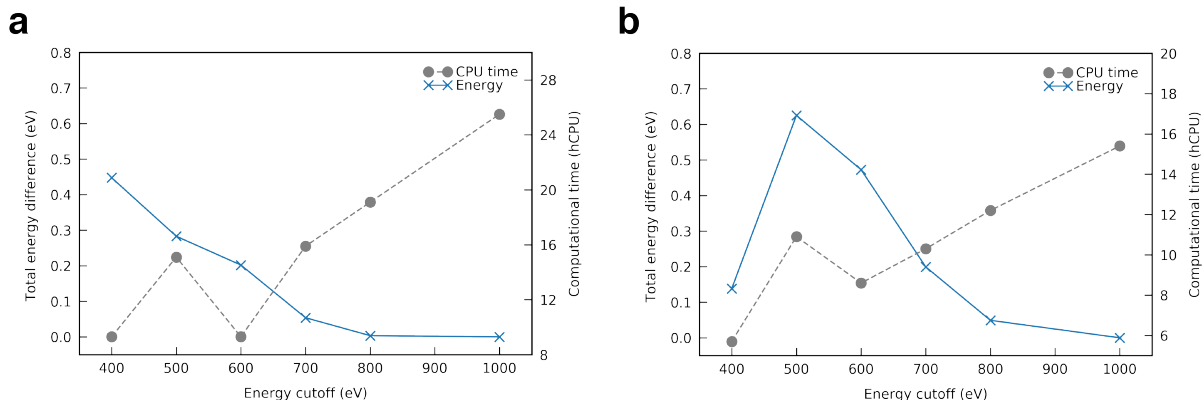
Figure 2.2: Simulation cell total energy (blue plain lines) and corresponding computation time (black dotted lines) for different planewaves kinetic energy cutoff values for a system consisting of an adsorbed hydroxide on hBN (a) or graphene (b). The case with the highest cutoff was chosen as the energy reference.

2.2.3   Ab Initio Molecular Dynamics

AIMD was performed using the CP2K code in its version 3.0 (chapter 4) or 5.1 (chapters 5 and 6)[121]. The computations of the forces were carried out using the implementation of the density functional theory (DFT) of the QuickStep module[122, 123]. DZVP-MOLOPT-SR-GTH basis sets were used[124] along with planewaves expanded to a 600 Ry energy cutoff, chosen over convergence of the DFT forces (see Fig. 2.3). Electronic cores were represented by Geodecker-Teter-Hutter pseudopotentials[125–127]. The PBE functional was used[112] with the D3 dispersion correction scheme[128, 129]. PBE-D3 has indeed been recently shown to provide a good description of the water/graphene interface[111]. The deuterium mass is substituted for all protons to reduce the time step

size needed for energy conservation in our Born-Oppenheimer AIMD and to limit nuclear quantum effects. The anion containing simulation cells did not include a counterion and the systems therefore presented a net charge neutralised by a uniformly charged background. AIMD simulations were carried out with a 0.5 fs timestep in the NVT ensemble at 323 K using Nose-Hoover thermostats[130, 131] with a time constant of 500 fs. At this increased temperature condition the PBE functional predicts a reasonable liquid water structure as it tends to yield a more viscous liquid[132].

Within this framework, simulating a hBN or graphene layer in contact with approximately a hundred water molecules costs between 800 and 1000 hCPU per picosecond of trajectory. The localised basis set and the size of the planewaves were chosen upon convergence of atomic forces for each element over MD runs of one hydroxide in the vicinity of the hBN/water and graphene/water interfaces (see Fig 2.3), computed with a cutoff of 400 Ry and the TZV2P-GTH basis set. 22 snapshots spaced by 500 steps of the BN simulation were considered as long as 12 steps distant of 20 snapshots of the graphene counterpart. The computational time and the cell potential energy were averaged over the hBN snapshots while the convergence of the atomic forces was quantitatively evaluated for each element as the room mean square error (RMSE) as compared to the case computed with the highest precision basis set and cutoff. Tests on the basis set were done with a 800 Ry cutoff while the tests on the cutoff were realised with the TZV2P-GTH basis. The data provided by the BN simulation was used for the atomic forces on B, N, O and H atoms as well as total potential energy and computational cost which were averaged over the 22 snapshots. The graphene simulation provided data for forces acting on C atoms. DZVP-MOLOPT-SR-GTH, the basis set ultimately chosen and used throughout the whole present study lead to a RMSE on atomic forces below 0.02 eV/Å for each element considered.

Radial distribution functions and density profiles normal to surfaces were obtained from MD trajectories by construction of histograms with a bin size of respectively 0.01 and 0.05 Å.

All movies for which a link is provided in the present document were generated using the
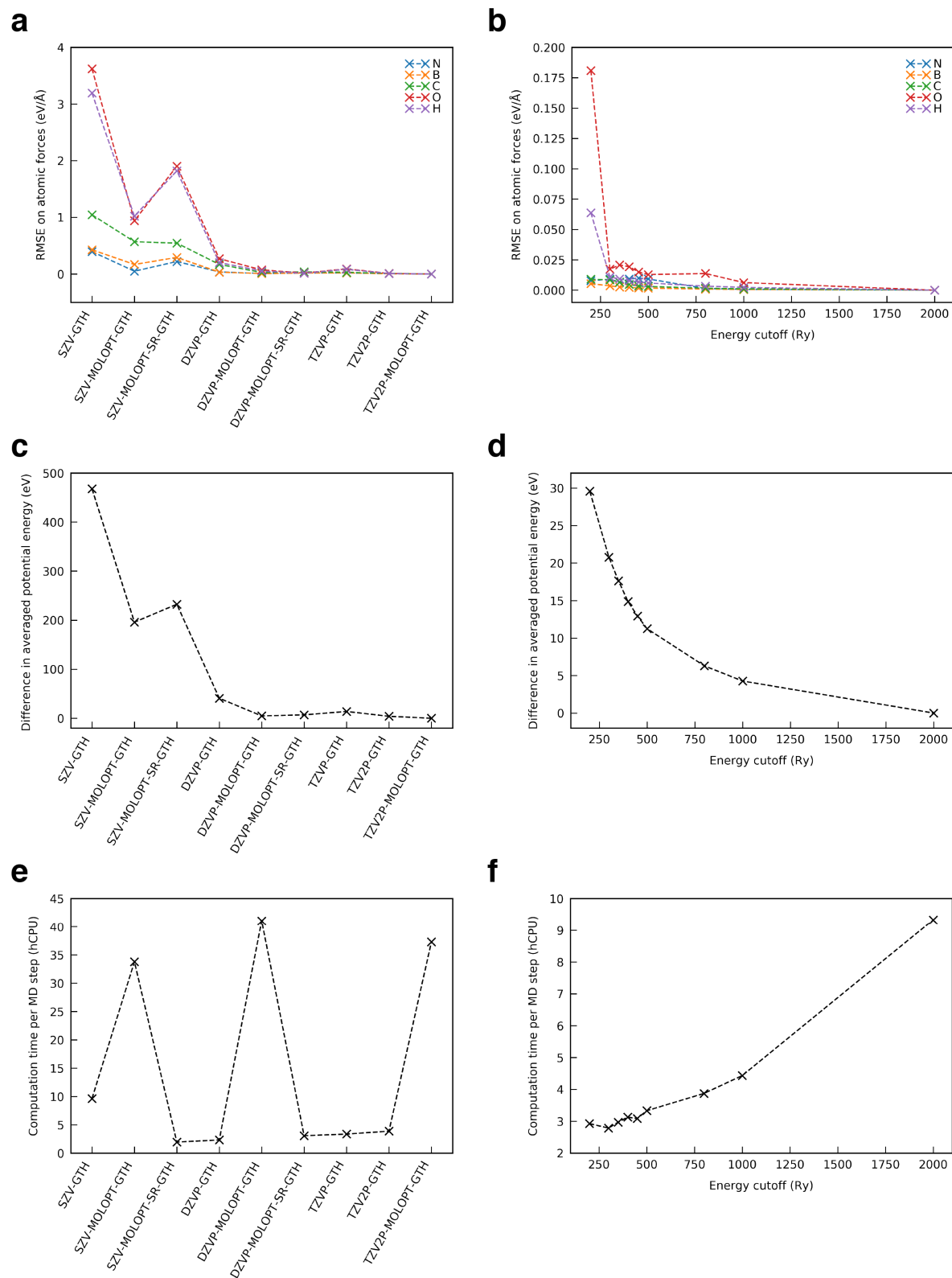
Figure 2.3: Convergence of atomic forces (a, b), of averaged potential energy (c, d) and computational time per dynamic step (e, f) with respect to changes of basis set (a, c, e) and planewaves cutoff energy (b, e, f).

Visual Molecular Dynamics (VMD) software version 1.9.2[133–135] and the Blender free-ware version 2.79. Hydrogen, boron, carbon, nitrogen and oxygen atoms are respectively represented in white, orange, grey, blue and red.

2.3 Methods for Chapter 3

Unless stated otherwise, computational details correspond to the ones described in section 2.2.

In order to derive atomic charges, Mulliken population analysis was performed and as this protocol requires localised basis sets, the Dmol^3 code[136–138] was used on the structures which had their geometry optimised by VASP, relying on a DFT framework as close as possible.

2.3.1 Simulation Cells

The hBN and graphene single-layers simulation cells are described in section 2.2.1. In the double layers systems, the sheets were distant of 3.35 Å and 3.45 Å for BN and graphene respectively. For both single and stacked layers, slab height of 15 Å was used. Dimensions of simulated nanotubes are summarised in table 2.1. Periodic images between tubes were distant by 10 Å.

Geometry	(n, m)	Number of Atoms	Diameter (Å)	Length (Å)
Zigzag	(13, 0)	160	11	12.56
Armchair	(8, 8)	156	10.39 (10.38)	13.05 (13.04)
Chiral	(10, 5)	280	10.57	23

Table 2.1:   Dimensions of nanotubes used for static DFT calculations. Diameter and length in parentheses correspond to BN tubes while the other values are the ones for CNTs.

2.3.2 Adsorption Energies

Energies of adsorption were determined by comparing the DFT energy of the geometry-optimised system consisting of the adsorbate chemisorbed on the single layer and that of the geometry-optimised reference state. Because of the uniformly charge background charge interacting with all the content of the supercell, the reference state consisted in both the substrate and the adsorbate far from it, precisely at a distance of 7.5 Å, to avoid spurious interactions between the surface and the free ion (see Fig. 2.4). The adsorption energy of a first hydroxide, E_{ads1} was therefore computed as $E_{ads1} = E(\text{OH}^-{}_{ads}) - E(surface + \text{OH}^-{}_{free})$ where $\text{OH}^-{}_{ads}$ and $surface + \text{OH}^-{}_{free}$ respectively designates the anion adsorbed on the surface and the system formed by the surface and the OH^- far from it. Similarly, the energy of adsorption of a second hydroxide E_{ads2} was derived as
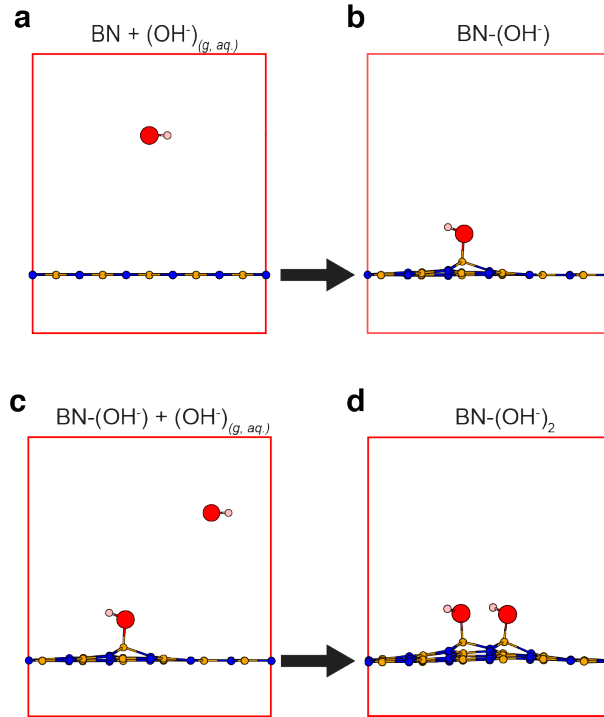
Figure 2.4: (top) Simulation cells for the hBN monolayer (same on graphene not shown) used to determine the energy of the adsorption of the first anionic hydroxide. a) $surface +$ $\text{OH}^-{}_{free}$: surface and one desorbed anionic hydroxide in gaseous or aqueous phase. b) OH^-_{ads}: surface with an adsorbed hydroxide onto either a B atom (BN layer) or a C atom (graphene layer). (bottom) Simulation scheme used to determine the energy of the adsorption of a second hydroxide c) $\text{OH}_{ads} + \text{OH}^-_{free}$: a surface with an adsorbed hydroxide and a desorbed hydroxide in gaseous or aqueous phase. d) 2 OH^-_{ads}: a surface with two adsorbed hydroxides.

$E_{ads2} = E(2\text{OH}^-{}_{ads}) - E(\text{OH}^-{}_{ads} + \text{OH}^-{}_{free})$, where $2\text{OH}^-{}_{ads}$ corresponds to the surface with 2 chemisorbed OH^-.

All the DFT energies were computed on geometries optimised both in vacuum or implicit solvent with each resulting atomic force below 0.02 eV/Å and with a gaussian smearing of 0.2 eV.

2.3.3   Thermodynamic Corrections

Although DFT provides energies at $T = 0$ K, thermodynamic corrections can be applied to yield results at finite temperature to estimate free energies. In particular, the relevant thermodynamic quantity evaluated at room temperature (297.15 K) and pressure (the dielectric permittivity of the implicit solvent being chosen equal to the value for water at $P = 1$ bar) is the Gibbs free energy of adsorption, $\Delta G_{ads}(T, P)$ at $T = 297.15$ K and $P = 1$ bar of OH^- on the single-layers surface in water, defined similarly as the energy of adsorption:

$$\Delta G_{ads}(T, P) = G(\text{OH}^-{}_{ads}) - G(surface + \text{OH}^-{}_{free}) \qquad (2.1)$$

with $G(\text{OH}^-{}_{ads})$, $G(surface + \text{OH}^-{}_{free})$ respectively designating the free energy of the ion adsorbed on the surface and the free energy of the surface with the hydroxide far from it. Since we work in the condensed phase and variations of volume are negligible, we approximate the Gibbs free energy simply as the free energy $A = E - TS$ of the system at temperature T (E is the internal energy as obtained by DFT and S the entropy): $G = A + PV \approx A$. Following a protocol successfully applied in surface science[139, 140], we evaluate the free energy of the system with OH^- adsorbed on the surface using the harmonic approximation as

$$A(\text{OH}^-{}_{ads}) = E + ZPE(\text{OH}^-{}_{ads}) - k_B T \log(Q^{vib}(\text{OH}^-{}_{ads})) \qquad (2.2)$$

with $ZPE(\text{OH}^-{}_{ads})$ the zero point energy, k_B the Boltzmann constant and Q^{vib} the vibrational partition function:

$$ZPE(\text{OH}^-{}_{ads}) = \sum_i \frac{\hbar\omega_i}{2}, \quad Q^{vib}(\text{OH}^-{}_{ads}) = \prod_i \frac{1}{1 - e^{\frac{-\hbar\omega_i}{k_B T}}} \tag{2.3}$$

where $\hbar$ is the reduced Planck constant and ω_i are the vibrational frequencies of the system in the harmonic approximation. The free energy of the reference state is the sum of that of the single-layer and that of the ion far from it: $A(surface + \text{OH}^-{}_{free}) = A(surface) + A(\text{OH}^-{}_{free})$. The substrate is also treated in the harmonic approximation yielding

$$A(surface) = E(surface) + ZPE(surface) - k_B T \log(Q^{vib}(surface)) \tag{2.4}$$

with $ZPE(surface)$ and $Q^{vib}(surface)$ defined similarly as in equation 2.3 with ω_i the surface vibrational frequencies. In the case of the free OH^- there are three additional translational degrees of freedom and a reference should be chosen. As the situation described here is that of a solute in a water solution, we take as reference the standard concentration $c^0 = 1$ mol.L^{-1}. Since OH^- is a non symmetric linear molecular, we have

$$\begin{aligned} A(\text{OH}^-_{free}) = {} & E(\text{OH}^-_{free}) + ZPE(\text{OH}^-_{free}) \\ & - k_B T \log(Q^{stretch}(\text{OH}^-_{free})) \\ & - k_B T \log(Q^{trans}(\text{OH}^-_{free})) \\ & - k_B T \log(Q^{rot}(\text{OH}^-_{free})) \end{aligned} \tag{2.5}$$

with $ZPE(\text{OH}^-_{free}) = \frac{1}{2}\hbar\omega_{stretch}$, $\omega_{stretch}$ corresponding to the stretch frequency of OH^- and where $Q^{stretch}$, Q^{trans} and Q^{rot} are respectively the vibrational, rotational and translational partition functions[141]. The vibrational partition function is

$$Q^{vib}(\text{OH}^-{}_{free}) = \frac{1}{1 - e^{\frac{-\hbar\omega_{stretch}}{k_B T}}} \tag{2.6}$$

while the rotational partition function for a linear non-symmetric molecule is given by $Q^{rot}(\text{OH}^-{}_{free}) = \frac{2Ik_B T}{\hbar^2}$ with I the inertial moment of OH^-[141]. At the standard concen-

OH$^-$ Chemisorbed on	hBN Layer	Graphene Layer
$ZPE(\mathrm{OH}^-_{ads})$	+ 9.5	+ 10.51
$-k_BT\log(Q^{vib}(\mathrm{OH}^-_{ads}))$	- 0.81	- 0.72
$ZPE(surface)$	+ 9.19	+ 10.15
$ZPE(\mathrm{OH}^-_{free})$	+ 0.23	+ 0.23
$-k_BT\log(Q^{vib}(surface))$	- 0.72	- 0.61
$-k_BT\log(Q^{stretch}\mathrm{OH}^-_{free})$	- 4.5 10^{-10}	- 4.5 10^{-10}
$-k_BT\log(Q^{trans}\mathrm{OH}^-_{free})$	- 0.19	-0 .19
$-k_BT\log(Q^{rot}\mathrm{OH}^-_{free})$	- 0.25	- 0.25
E^{sol}_{ads1}	- 0.89	+ 0.33
$\Delta G_{ads}(T = 297.15$ K, $P = 1$ bar)	- 0.46	+ 0.79

Table 2.2: Detailed thermodynamic corrections and the Gibbs free energy of the first adsorption evaluated in eV at 297.15 K and 1 bar. ϵ_b, the dielectric permittivity of the implicit solvent, was given the value of 78.4 corresponding to water at $P = 1$ bar. ZPE stands for the zero point energy, Q corresponds to the various contributions to the partition function and E^{sol}_{ads1} is the DFT energy of first adsorption in implicit water. All energies are in eV.

tration c^0, the translational partition function becomes $Q^{trans}(\mathrm{OH}^-_{free}) = (\lambda^3_D c^0 N_A)^{-1}$, with $\lambda_D = \hbar\sqrt{2\pi/mk_BT}$ the De Broglie wavelength, m the mass of one OH$^-$ molecule and N_A the Avogadro constant. Noteworthily since we did not compute the energy of the substrate and the free OH$^-$ separately, we consider $E(surface + \mathrm{OH}^-_{free}) = E(surface) + E(\mathrm{OH}^-)$.

All the vibrational frequencies ω are obtained via the calculation and diagonalization of the Hessian matrix by finite difference, *i.e.* by evaluating atomic forces while slightly displacing every atom in every non-redundant direction. Values for each thermodynamic contribution computed at $T = 297.15$ K can be found in Table 2.2. It is noteworthy that the most important correction arises from the ZPE term but since we are dealing with differences to compute ΔG_{ads}, all minor terms play a role.

2.3.4   Charge Neutralisation by a Counter-Ion

To confirm the relevance of the use of a uniformly charged background to achieve cell neutrality, adsorption energies were compared within this framework and when including a potassium cation as counter-ion in the simulations. The energies were found remarkably close between the two cases. Since the presence of a counterion far from the hydroxide

| | With Potassium | | Without Potassium | |
	hBN	Graphene	hBN	Graphene
E_{ads}^{vac} (eV)	- 1.44	- 0.44	- 2.3	- 0.50
E_{ads}^{sol} (eV)	- 0.83	+ 0.38	- 0.89	+ 0.33
K - O distance (Å)	7.71	7.71	-	-
K - Surface distance (Å)	4.84	4.78	-	-

Table 2.3: Adsorption energy of a hydroxide on BN and graphene layers in vacuum (E_{ads}^{vac}) and in implicit water (E_{ads}^{sol}) with and without a potassium counterion present in the supercell. The distance between the counterion and the oxygen atom of the hydroxide as well as the distance of the potassium to the surface are also displayed. When including the counterion the energies where derived from the geometries optimised without the cation.

and the surface is only relevant if a solvent is present, one should especially compare adsorption energies obtained within the implicit water approach. In water, the differences in adsorption energies between the systems with and without the potassium cation were found to be less than 70 meV, as displayed in Table 2.3.

2.4 Methods for Chapter 4

Unless stated otherwise, computational details correspond to the ones described in section 2.2.

2.4.1 Simulation Cells

Construction of Starting Configurations

The hBN (graphene) single layer / water interface was modelled using a 13.04 Å× 12.55 Å× 21.0 Å (12.83 Å× 12.35 Å× 21.0 Å) orthorhombic cell containing 60 surface atoms arranged in a hexagonal monolayer, one hydroxide anion and 97 (94) water molecules under periodic boundary conditions (see Fig. 2.5). This corresponds to surfaces separated by a $\sim$ 16 Å thick and 0.57 M hydroxide aqueous solution yielding pH 13.8. Simulations in bulk water were performed in a 12.42 Å side cubic cell containing 63 water molecules and one charged hydroxide. The very first water configuration was an output of a more than 60 ps long trajectory of a 12.42 Å side cubic cell containing 64 water molecules simulated within a similar framework. It was used to build interface systems since the size of the 60

atoms hexagonal layers roughly corresponded to the 12.42 × 12.42 Å² section of the water box. A 2.5 Å interfacial distance between water and the surface atoms was considered and water molecules were added or displaced to reach the desired system with a liquid density of 1. Water density profiles were obtained after 5 ps of equilibration during 50 ps production runs of the hBN/water and graphene/water simulation cells. A hydrogen atom was deleted in the last configuration of each trajectory to yield simulation cells containing a hydroxide anion. For biased trajectories, the hydroxide was fixed at a chemisorption distance of 1.5 Å from a surface atom by freezing the surface site and the hydrogen oxygen O^*. Its hydrogen coordination was restrained as described below during an equilibration run of 5 ps before yielding the starting configuration of the biased simulations. The simulation cells of the free trajectories containing a surface and OH^- were initiated using the restrained equilibration of the biased runs at appropriate ion-surface distances.
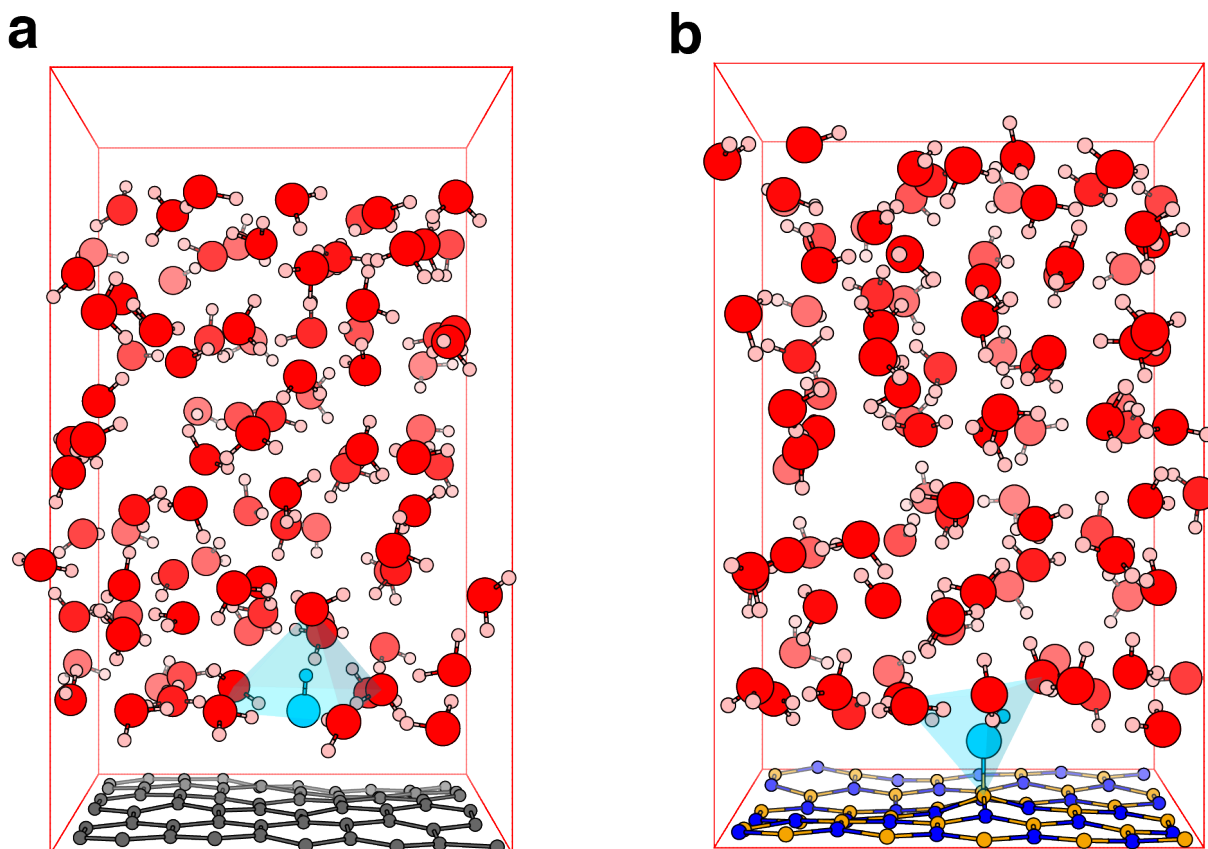
Figure 2.5: Simulation cells of a hydroxide at the graphene/water (a) and hBN/water (b) interfaces. Hydrogen, boron, carbon, nitrogen and oxygen atoms are respectively represented in pink, orange, grey, blue and red. The hydroxide is displayed in cyan within a polyhedron of the same colour representing the geometry of its local chemical environment.

Pressure Evaluation

The rather arbitrary 2.5 Å criterion for the position of the interface was confirmed to be *ad hoc* by evaluation of the pressure in the cell, with the target value of 1 bar within error bars. In fact mean pressures of 0 ± 95 MPa and 73 ± 93 MPa were thereby derived for the hBN and graphene simulation cells, respectively. The errors correspond to standard deviations derived by block analysis (see section 2.4.3) and are in the range of pressure variations within NVT AIMD simulation cells reported in literature[142]. To derive those pressures, the atomic forces were recomputed on 200 snapshots distant by 0.1 ps in the 20 ps free trajectories of the physisorbed hydroxide, after adding an additional 10 Å vacuum separation between water and one side only of the surface. The pressure was then evaluated as the average over those 200 snapshots of the sum of the normal component of the forces acting on the surface atoms divided by the simulation cell section area. The overall structure of water was found unaffected by the slab geometry when comparing the radial distribution functions of the liquid between the interfacial systems and bulk water.

2.4.2 Simulation Protocols

Free Trajectories

The simulation of a free hydroxide in bulk water was performed on a 12.42 Å $\times$ 12.42 Å $\times$ 12.42 Å unit cell containing 63 water molecules and 1 OH^-. The system was equilibrated for 5 ps before a 50 ps production run was computed. The last snapshot of the restrained trajectory with the appropriate restraint parameter and anion-surface distance (see section 2.4.2) was used as the starting atomic configuration for non-biased simulations. We started from pre-equilibrated systems at the considered distances: the 20 ps trajectory of a free physisorbed anion on graphene (hBN) was computed starting from a configuration obtained with $D_{O^*-A^*}$ and n^* respectively equal to 3.2 Å and 1.3 (3.6 Å and 1.3). For the chemisorption case, $D_{O^*-A^*}$ and n^* were respectively equal to 1.5 Å and 1.0 for both graphene and BN.

Biased Trajectories

The potential of mean force (PMF) of the aqueous hydroxide anion with respect to its distance to a hBN or graphene layer is obtained by thermodynamic integration over the component normal to the surface of the force acting on the oxygen O^* of OH^-, $F_{O^*}^\perp$ (see section 2.4.3). To obtain $\left\langle F_{O^*}^\perp \right\rangle_r$, the mean force of interest for a surface-anion distance r, molecular dynamics are performed with constraining this distance by freezing a surface atom A^* and the hydroxide oxygen O^*. Starting close to the material, the anion is progressively displaced until it reaches 6 Å. Trajectories are computed for each value thereby spanned by r. However, this requires to keep track of the elusive anion prone to proton exchange with solvating water molecules. To prevent proton hops, the hydrogen coordination of the hydroxide oxygen n_{O^*-H} is restrained around a target value n^* by applying a harmonic potential W of the form:

$$W = k(n_{O^*-H} - n^*) \tag{2.7}$$

with $k = 0.05$ Ha a force constant and using the definition of the coordination proposed by Iannuzzi et $al.$[143]:

$$n_{O^*-H} = \sum_{i=1}^{N} \frac{1 - \left(\frac{r_i}{R_0}\right)^{12}}{1 - \left(\frac{r_i}{R_0}\right)^{20}} \tag{2.8}$$

where i runs over every hydrogen atom of the simulation box (N in total); with r_i the distance between hydrogen i and O^*. R_0 is a switch distance set to 1.2 Å which corresponds to the minimum between the first and second peak of the radial distribution function $g(r)$ of hydrogen atoms around O^* computed for a free OH^- in bulk water. This is illustrated in Fig. 2.6 in which the $g(r)$ is displayed in black and the switch function (see equation 2.8) in blue.

Because of the dependency of n_{O^*-H} on the first solvation shell (see Fig. 2.6, non-zero values of the blue curve between 1.2 and 2 Å), the hydrogen coordination target of the restraint n^* (see equation 2.8) does not necessarily correspond to the desired number of hydrogen atoms in the covalent shell of O^*. In fact, $\langle n_{O^*-H} \rangle$ varies along with the
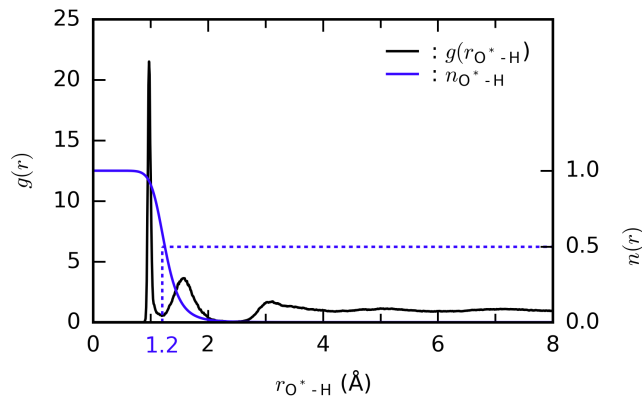
Figure 2.6: The radial distribution function $g(r)$ of hydrogen atoms around the hydroxide oxygen O* is plotted in black. The corresponding contribution to the hydrogen coordination n_{O^*-H} is displayed in blue.

hydroxide-surface distance $D_{O^*-A^*}$ and more generally with the environment of OH$^-$, as illustrated in Fig. 2.7 in which histograms of n_{O^*-H} are displayed for different cases. One can observe a clear difference between the histogram of a free OH$^-$ chemisorbed on hBN (orange curve) and that of the free anion in bulk water (black curve). The latter exhibits a peak centered at 1.3 that corresponds to the standard picture of an anion isolated within a solvation shell. However a part of this distribution crosses the one of H$_2$O in bulk water (green curve) around 1.8 and that overlap corresponds to configurations where the hydroxide is in the form of a transient H$_3$O$_2^-$ species in which a proton is shared between the hydroxide and a water molecule (see the inset in the black circle). In this second situation, the coordination of the anion resembles that of a bulk water molecule (green curve) and proton transfer is prone to occur. We therefore wish to avoid those configurations, by centering the coordination distribution either on the peak of the chemisorbed anion (around 1.0) or on the peak of the standard solvated hydroxide (around 1.3). Configurations excluding proton transfer were therefore obtained, as illustrated by the distribution for the anion in bulk water with its coordination restrained to 1.3 (red curve). Since two coordination values were to be considered to represent the system in which the anion is either chemisorbed or in bulk water or in-between, two dynamics are performed for each finite value of $D_{O^*-A^*}$ with n^* respectively set to 1.0 and 1.3. For each distance probed, the MD runs are the object of a further analysis before computation of the PMF can be performed (see 2.4.3).
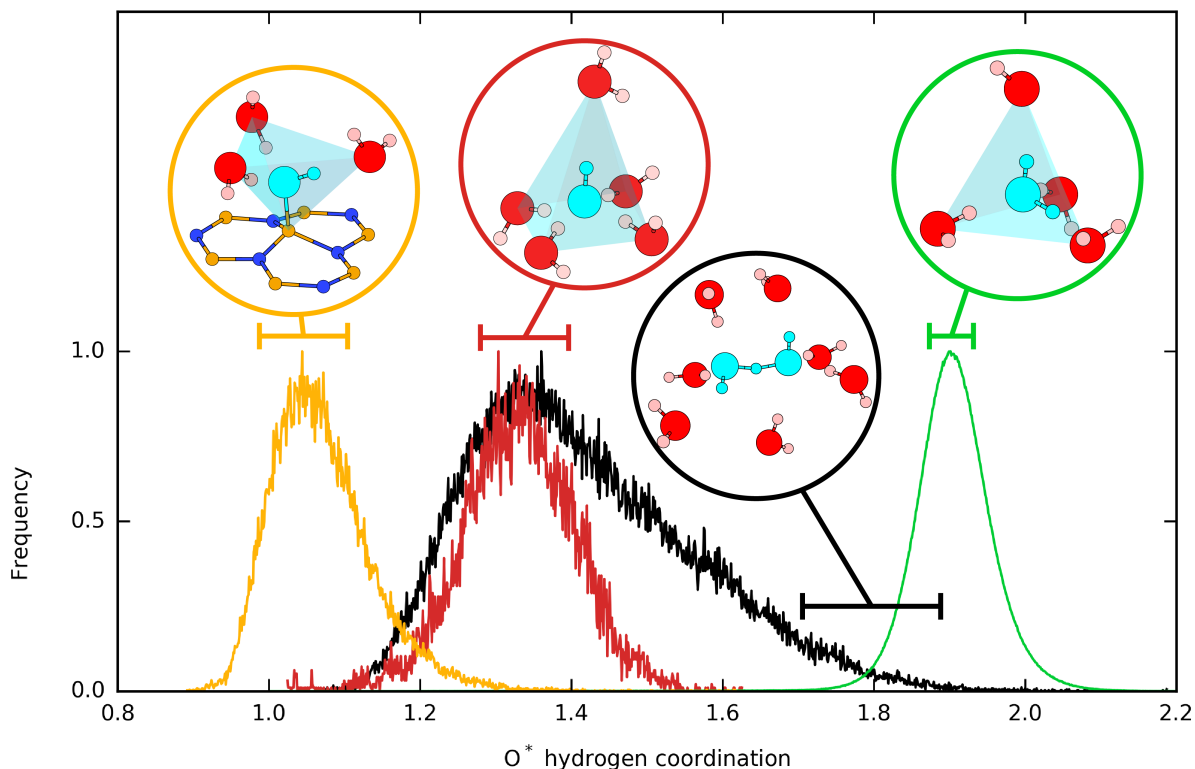
Figure 2.7: Histograms of the hydrogen coordination of a free hydroxide chemisorbed on hBN (orange line), of a free hydroxide in bulk water (black line), of a coordination restrained hydroxide in bulk water (red line) and of bulk water molecules (green line). Insets exhibit the solvation geometry of corresponding configurations. Oxygen and hydrogen atoms are respectively displayed in red and pink. The solvated species (H_2O, OH^- and $H_3O_2^-$) are represented in cyan. The unrestrained hydroxide oxygen O^* was identified as the closest oxygen atom to one hydrogen only. Each histogram was normalised so that its maximum would be 1.0.

To probe the desired range of values for $D_{O^*-A^*}$, successive dynamics were performed with the hydroxide translated by 0.1 or 0.2 Å using the last atomic configuration of the previous run. For each distance, the system was equilibrated for 0.5 ps plus an additional 0.5 ps if restraint parameters were modified. For each value of $D_{O^*-A^*}$ and for each value of the restraint target, production runs were then performed. Two sets of MD trajectories have thus been computed with the restraint parameter n^* respectively set as 1.0 and 1.3 (see equation 2.7). Production runs of 2 to 3 ps were performed with the first target value and between 4 and 6 ps for the second one. Every configuration in which proton transfer occurred were excluded from data analysis.

Atoms frozen during a trajectory computed with CP2K leads it to print out null forces acting on them, yet in the present case the force acting on O^* was precisely the one of

interest, required for the thermodynamic integration. It was then necessary to recompute the atomic forces in the configurations obtained over the course of biased trajectories while removing the restraints and constraints. Thanks to the high correlation between successive MD snapshots, re-evaluating DFT forces on solely 1 out of 10 configurations provided a satisfactory statistic. However the trajectories being obtained with the bias included, the unbiased forces were not the data from which the sought potential of mean force could be derived. The ultimate quantity of interest is indeed the biased forces corresponding to the snapshots they allowed to obtain. We could retrieve the quantity of interest as follows:

$$\boldsymbol{F}_{O^*}^{b} = \boldsymbol{F}_{O^*}^{ub} + \boldsymbol{B}_{O^*} \qquad (2.9)$$

where $\boldsymbol{F}_i^b$, $\boldsymbol{F}_i^{ub}$ and $\boldsymbol{B}_i$ respectively designate the biased force, the unbiased force and the biasing force applied to atom i. The bias applied to O^* can be retrieved from the sum of those applied to each hydrogen:

$$\boldsymbol{B}_{O^*} = -\sum_{j \in H} \left(\boldsymbol{F}_{H_j}^{b} - \boldsymbol{F}_{H_j}^{ub} \right) \qquad (2.10)$$

so that the force to be ultimately used in free energy analysis can be directly computed from simulations outputs as:

$$\boldsymbol{F}_{O^*}^{b} = \boldsymbol{F}_{O^*}^{ub} + \sum_{j \in H} \left(\boldsymbol{F}_{H_j}^{b} - \boldsymbol{F}_{H_j}^{ub} \right) \qquad (2.11)$$

2.4.3 Analysis

Weighted Histogram Analysis Method

The two sets (one for each restraint coordination target) of computed trajectories were combined using the Weighted Histogram Analysis Method (WHAM) of Kumar *et al.*[144], within a homemade implementation. The extension of this method proposed by Souaille

and Roux[145] was applied independently for each given value of $D_{O^*-A^*}$ to appropriately re-weight every snapshot of the two dynamics and combine them into a WHAM trajectory along which observables could be computed:

$$\langle A \rangle = \frac{1}{\sum\limits_{i,l} w_{i,l}} \sum_{i=1}^{2} \sum_{l=1}^{n_i} w_{i,l} A_{i,l} \tag{2.12}$$

where A is an observable, i refers to one of the two trajectories of length n_i (both simulated at a given value of $D_{O^*-A^*}$), l indicates the lth snapshot of the ith trajectory and $w_{i,l}$ designates the weight obtained by WHAM for the lth snapshot of trajectory i. Numerically this re-weighting is performed by self-consistently determining the set of N free energy shifts $\{f\}$ between N trajectories from a set of N equations:

$$k^{th} \text{ equation: } e^{-\beta f_k} = \sum_{i=1}^{N} \sum_{l=1}^{n_i} \frac{e^{-\beta W_k(R_{i,l})}}{\sum\limits_{j=1}^{N} n_j e^{-\beta(W_j(R_{i,l})-f_j)}} \tag{2.13}$$

with $\beta = 1/k_B T$ and where k, i and j corresponds to the kth, i^{th} and j^{th} trajectories, with n their length in number of snapshots. $R_{i,l}$ corresponds to the lth atomic configuration of trajectory i while W_k and W_j represent the energy bias function with the parameters (force constant, centre of the harmonic bias) as set in the trajectory k and j, respectively. Each value of $\{f\}$ was converged within 1 meV. Finally the weight $v_{i,l}$ of the lth snapshot of trajectory i is obtained as:

$$v_{i,l} = \left[\sum_{j=1}^{N} n_j e^{-\beta(W_j(R_{i,l})-f_j)} \right]^{-1} \tag{2.14}$$

so that ultimately normalising the total weight of the N trajectories analysed to 1, the weight $v_{i,l}$ is replaced by:

$$w_{i,l} = \frac{v_{i,l}}{\sum\limits_{j=1}^{N} \sum\limits_{k=1}^{n_j} v_{j,k}} \tag{2.15}$$
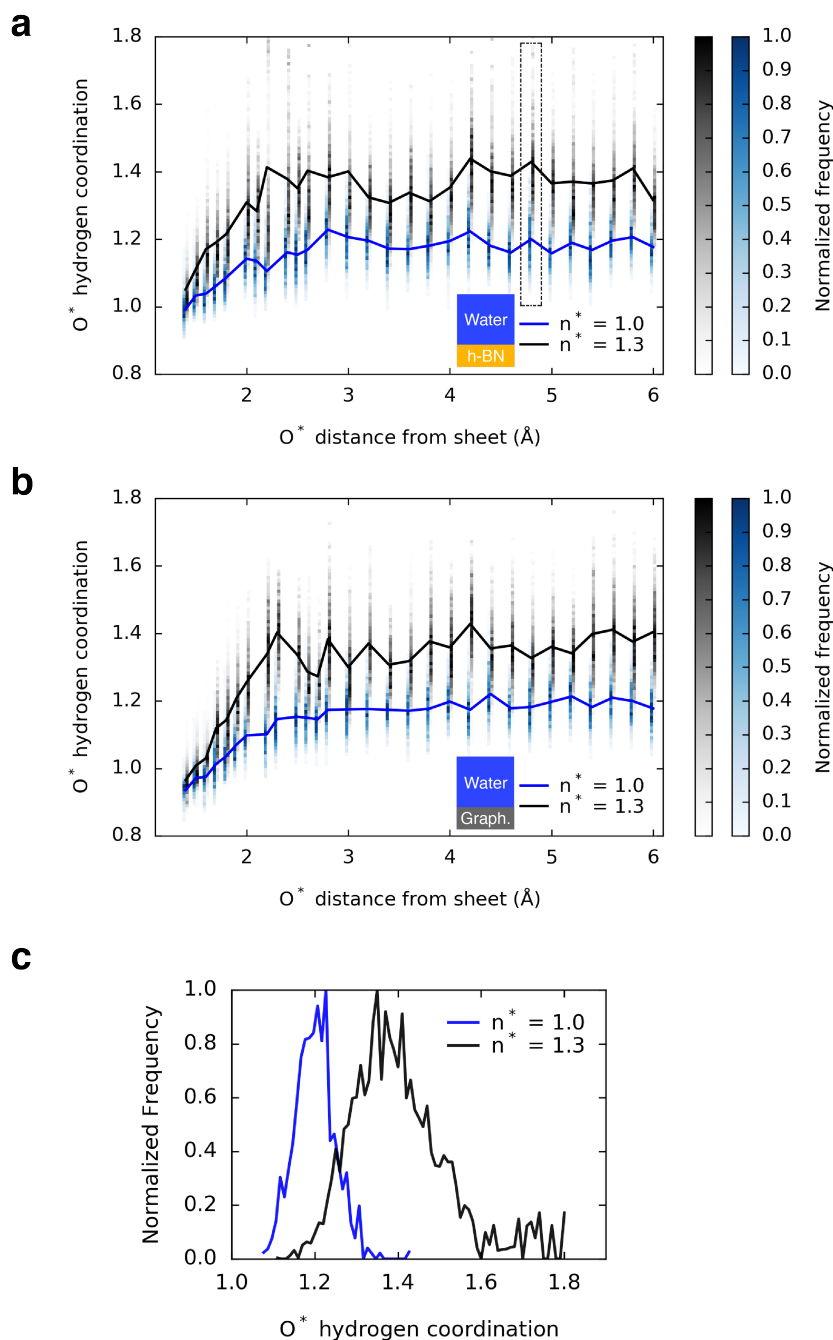
Figure 2.8: Mean hydrogen coordination of OH$^-$ at the water/hBN (a) and water/graphene (b) interfaces for the two sets of MD trajectories respectively corresponding to a coordination restraint target n^* of 1.0 (blue) and 1.3 (black). Coordination histograms for each anion-surface distance are represented by vertical lines which colour indicates the frequency of a particular coordination value following the colour scales. c) Overlap of two histograms obtained at a distance OH$^-$-BN of 4.8 Å as identified by a dotted frame in a). Each histogram was normalised so that its maximum would be 1.0.

The two sets of MD trajectories can be visualised by the associated mean hydrogen coordination (see Fig. 2.8a and b) while one can represent the WHAM trajectory with the WHAM derived mean hydrogen coordination $\langle n_{O^*-H} \rangle$, as displayed by white curves in Fig. 2.9. The WHAM method enables us to smoothly interpolate the two trajectories obtained with $n^* = 1.3$ and $n^* = 1$ with weights depending on the distance $D_{O^*-A^*}$.

To illustrate the convergence of the WHAM process, the overlap of the coordination histograms of the two recombined MD runs (see Fig. 2.8) for each distance is displayed in Fig. 2.8 a and b by representing the histograms vertically with the associated probabilities visualised by colour scales.

One Dimensional Potential of Mean Force

The 1D PMF was derived using thermodynamic integration. Once the trajectories recombined along the hydrogen coordination dimension by WHAM, the average $\left\langle F_{O^*}^{\perp} \right\rangle_r$ of the component normal to the surface of the force acting on O^* was computed for every given value r of $D_{O^*-A^*}$ using equation 2.16. These averages were then integrated to yield the free energy of OH^- at a distance d from the surface as a potential of mean force (PMF), taking as reference the situation in which the anion is at the furthest distance from the surface.

$$\mathrm{PMF}(d) = \int_{\mathrm{bulk}}^{d} \left\langle F_{O^*}^{\perp} \right\rangle_r dr \tag{2.16}$$

The overall PMF computation strategy is illustrated in Fig. 2.9: the anion-surface distance was probed by blue moon sampling as this variable was fixed during each MD run (blue arrow). To perform umbrella sampling along the hydrogen coordination dimension (white arrow), two sets of trajectories with different restraint targets were computed (two white horizontal lines). For each given anion-surface distance, the two trajectories were recombined using WHAM allowing for the computation of the relevant mean forces on which thermodynamic integration was performed (red arrow). The WHAM trajectory is represented by the mean hydrogen coordination displayed as a white curve.
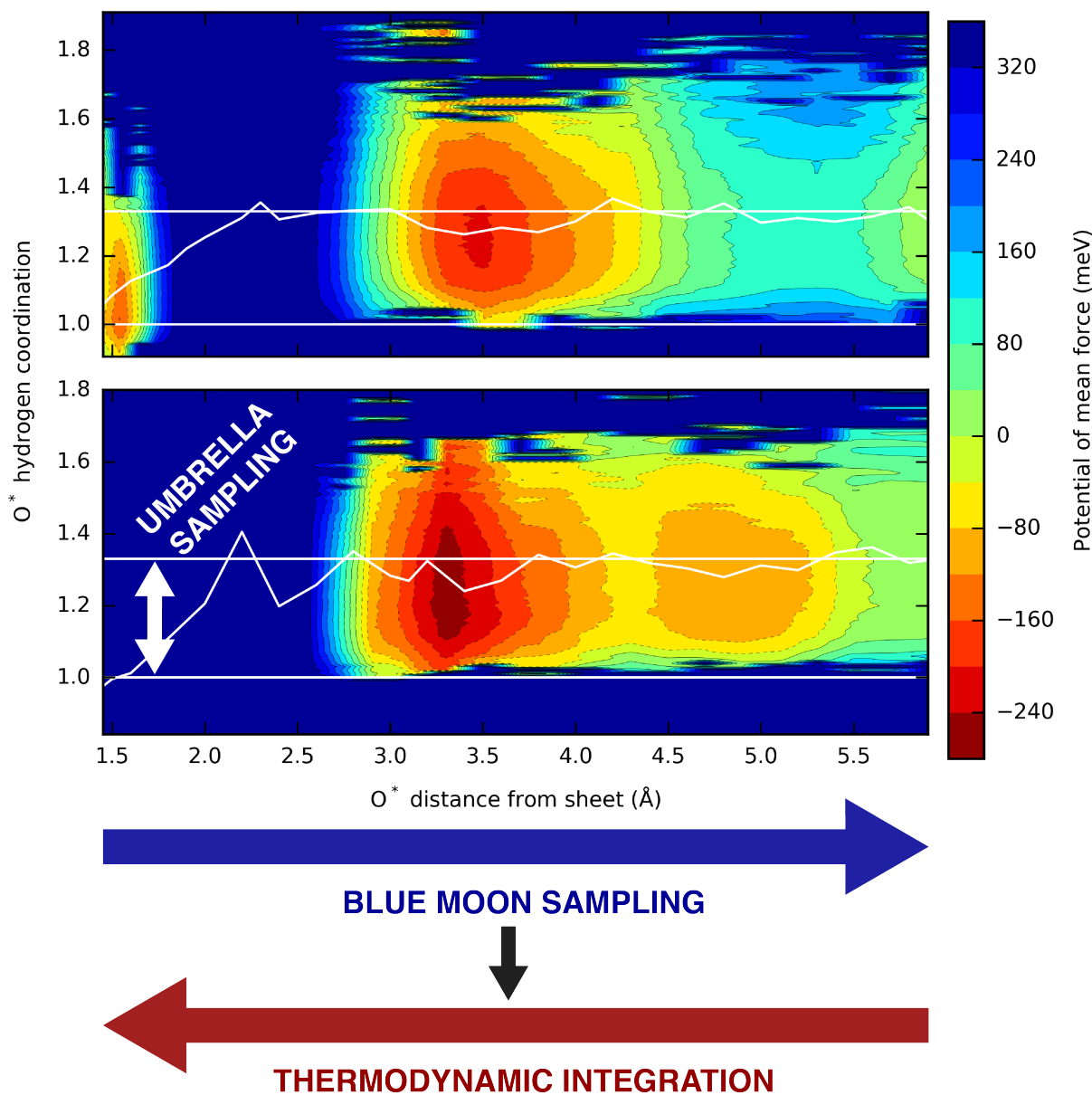
Figure 2.9: Free energy profiles of OH⁻ with respect to its hydrogen coordination and its distance from a single layer hBN (top) and graphene (bottom). White horizontal lines represent the two sets of MD trajectories, computed for a coordination target of 1.0 and 1.3. The WHAM mean hydrogen coordinations are displayed by white curve, thus representing the WHAM trajectory obtained by umbrella sampling between the two sets of dynamics. The blue arrow represents the direction of blue moon sampling - along the anion-surface distance - along which the thermodynamic integration (red arrow) is performed starting from the furthest distance from the surface.

Estimation of errors

Since successive MD snapshots are highly correlated, the error on observables computed as statistical averages along the trajectory were derived by artificially reducing the overall data correlation as we resorted to block analysis which consists in dividing the trajectory into a varying number of blocks n_b of identical length[146]. Once the average of each block is computed, the mean of all the block averages is derived alongside its standard deviation σ_{blocks}. An estimation of the deviation on the trajectory σ_{traj} can be obtained by linear regression as it can be approximately linked with σ_{blocks} and n_b in the following relation:

$$\sigma_{blocks}^2 \approx \sigma_{traj}^2 \times (n_b - 1) \tag{2.17}$$

In the case of observables computed on the WHAM trajectory, we considered blocks of identical total WHAM weight instead of identical snapshot length. To estimate the standard deviation $\sigma_{PMF}(i)$ of the ith point of the PMF, the square of the deviations σ_r of $\left\langle F_{O^*}^{\perp} \right\rangle_r$ obtained for each intermediate distance r were summed:

$$\sigma_{PMF}(i)^2 = \sum_{k=1}^{i} \left(\sigma_{r_k} \frac{r_k - r_{k+1}}{2} \right)^2 \tag{2.18}$$

where $r_{k=1}$ corresponds to the furthest distance from the surface. The deviations σ_{r_k} were obtained using the above-mentioned WHAM corrected block analysis.

Two-Dimensional Potentials of Mean Force

Combining the PMF obtained by thermodynamic integration with $P(n|r)$ the coordination probability distributions for a given value r of $D_{O^*-A^*}$, one can reconstruct two-dimensional PMFs as displayed in Fig. 2.9:

$$PMF(n,r) = -k_B T \log(P(n,r)) + \alpha \tag{2.19}$$

where $T = 323$ K, k_B is the Boltzmann constant, α is a constant, n refers to the coordination and P to probabilities. The probability to find the system at (n,r) is obtained as

follows:

$$P(n, r) = P(n|r).P(r) \tag{2.20}$$

where $P(r)$ is directly derived from the one-dimensional PMF described above:

$$P(r) = C.e^{-\frac{1}{k_B T} \text{PMF}(r)} \tag{2.21}$$

where C is a constant that vanishes along with α upon normalisation of the total probability.

The energy surface thus obtained supports the necessity of probing the coordination of the hydroxide as a reaction variable. In fact, one can observe on the upper map of Fig. 2.9 that the two energy minima of the case of hBN are found at significantly different coordination values.

For analysis purposes the treatment used to derive a two-dimensional PMF was also applied to the oxygen coordination of the hydroxide n_{O^*-O}. The latter was defined similarly as n_{O^*-H} with the R_0 parameter set to 3.2 Å (see equation 2.8), corresponding to the minimum between the second and third peak of the radial distribution function $g(r)$ of oxygen atoms around O^* computed for a free OH^- in bulk water. The 12 and 20 exponents in equation 2.8 were respectively switched to 40 and 100 to yield a coarser function allowing for a clearer physical interpretation of n_{O^*-O}.

Self-Diffusion Coefficients

The diffusion coefficients were computed using the Einstein equation with the mean square displacements (MSD) derived from the unbiased MD trajectories:

$$\frac{1}{2d} \left\langle X^2(t) \right\rangle = Dt \tag{2.22}$$

where d is the dimensionality of the displacement X, D is the diffusion coefficient and t designates time. The mean displacement of N_{part} particles along a t_{max} long trajectory is obtained as follows:

$$\langle X^2(t) \rangle = \frac{1}{N_{\text{part}}} \sum_{i=1}^{N_{\text{part}}} \sum_{t=0}^{t_{\text{max}}} \frac{1}{n_\tau} \sum_{\tau=0}^{t_{\text{max}}-t} (X_i(\tau) - X_i(\tau + t))^2 \tag{2.23}$$

where n_τ is the number of snapshots between 0 and $t_{\text{max}} - t$. The diffusion coefficients were obtained by linear regression over equation 2.22. The coefficient for H_2O molecules in bulk water was found to be 0.49 ± 0.15 $10^{-5}.cm^2.s^{-1}$, in the range of the literature values derived by AIMD[147, 148]. In that case, the length of the trajectory (50 ps) and the number of particles considered (64) yielded a statistic large enough to compute the coefficient by dividing the trajectory into five blocks of 10 ps each. A value was derived on each block by linear regression between 0.3 and 10 ps. The final coefficient is an average of the 5 thus derived values with the corresponding standard deviation taken as the error. Nonetheless a different procedure was adopted for the diffusion of the hydroxide since the MSD of only one particle is considered, yielding a too small statistic to relevantly divide the data into blocks. Linear regressions on the MSD were performed over a 5 ps interval sliding between 0.3 and 45 ps for OH^- in water and between 1 and 15 ps for the anion close to the surfaces. The diffusion coefficients were averaged over all these regressions and the corresponding standard deviation was taken as an estimate of the error. This multiple linear regression process is illustrated in Fig. 2.10.
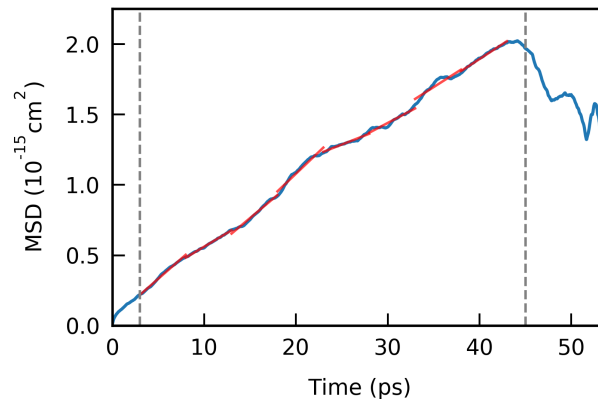
Figure 2.10: Mean square displacement over time of a hydroxide in bulk water (blue line). Its diffusion coefficient is estimated by multiple linear regressions over 5 ps between the limits marked by vertical dotted lines. Only a few linear regressions are displayed by transparent red segments although the regression interval continuously slides between the boundaries at 0.3 and 45 ps.

Gibbs Dividing Surface and Surface Excess

The derivation of the position of the Gibbs dividing surface (GDS), r_{GDS} was adapted from Bonthuis *et al.*[149], considering the interface between water and the atomic surface at which the liquid density is canceled out:

$$r_{\mathrm{GDS}} = \int_0^{r_{\mathrm{bulk}}} \left(1 - \frac{\rho_{\mathrm{H_2O}}(r)}{\rho_{\mathrm{H_2O}}(r_{\mathrm{bulk}})} \right) dr \qquad (2.24)$$

where r designates the distance to the surface and $\rho_{\mathrm{H_2O}}$ is the water density corresponding to the blue curves in Fig. 4.2. The average of the density profiles between 5 Å and the furthest point from the surface (10.5 Å) is taken as the bulk value allowing to define r_{bulk} as the furthest distance from the interface for which this density value is reached. r_{GDS} yielded 1.8 Å for both graphene and hBN.

Adapting from the expression of Horinek and Netz[150], the surface excess of hydroxide Γ was derived as

$$\Gamma = [\mathrm{OH}^-]_{\mathrm{bulk}} \int_{1.45\text{Å}}^{5.9\text{Å}} \left(e^{-\frac{\mathrm{PMF}(r)}{k_B T}} - 1 \right) dr \qquad (2.25)$$

where $T = 300$ K, $[\mathrm{OH}^-]_{\mathrm{bulk}} = 0.57$ M (corresponding to pH = 13.8) is the bulk concentration of hydroxide extrapolated for water in ambient conditions considering the molecular ratios of OH^- to $\mathrm{H_2O}$ molecules in the simulation cells. Positive surface excesses of 38.5 C.m^{-2} (399 μmol.m^{-2}) and 6.2 C.m^{-2} (64 μmol.m^{-2}) were respectively obtained for graphene and hBN. The surface charges thus derived are higher than experimental values[35, 36] since equation 2.25 corresponds to the case of infinite dilution with no counter-ions, contrary to the experimental situation. This issue will be addressed in section 4.4 of chapter 4 while deriving an analytic model of the ionic conductance.

2.5   Methods for Chapter 5

Unless stated otherwise, computational details correspond to the ones described in section 2.2.

2.5.1   Simulation Cells

Both DFT and AIMD simulations were performed using orthorhombic cells containing a hexagonal sheet consisting of 72 carbon, 36 boron and 36 nitrogen atoms. To model the junctions of the zigzag and armchair type, 14.77 Å × 25.58 Å and 12.78 Å × 29.55 Å single layers were respectively used, separated by 15 Å of vacuum for static DFT calculations and 21 Å of explicit water for AIMD trajectories. The top views of the neutral Lewis structures of the three investigated cells are displayed in Fig. 5.2. The first and the second cell parameters are respectively parallel to the heterojunction and perpendicular to the surface. The hBN and graphene primitive lattice parameters a (2.51 Å and 2.47 Å respectively) evaluated within the present DFT framework exhibit a mismatch of 0.04 Å, in agreement with previous calculations using a similar method[94, 103]. The lattice parameter of hBN was chosen to construct the cell, therefore inducing strain in the counterpart network. Because of the lattice mismatch, only a large supercell containing thousands of surface atoms could prevent inducing strain in the layer. It is noteworthy that such materials are grown epitaxially over a substrate which lattice can also be a source of strain[151, 152].

To build the AIMD simulation cells containing the single-layer in contact with water, we relied on a different approach than the one described in section 2.4.1. Taking advantage of the *ad hoc* definition of the 2.5 Å position of the hBN/water and graphene/water interfaces, 195 H_2O were randomly placed in a cell corresponding to a 16Å water separation between periodic images of the surface, while making sure water molecules were at least 2 Å apart from one another. This was done using the Packmol software[153]. The water cell was then juxtaposed to the surface with a 2.5 Å vacuum separation (on each side of the single layer) to yield the 21 Å high final slab (see Fig. 2.11). Since Packmol only takes into account a criterion of minimal distance between molecules, excluding any chem-
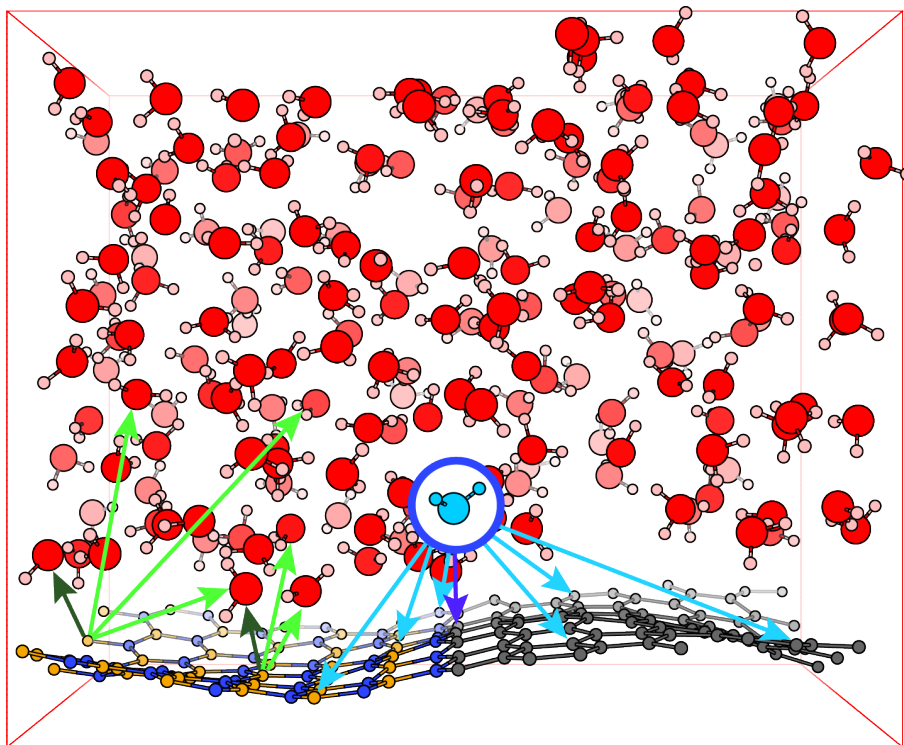
Figure 2.11: AIMD simulation cell of the zigzag junction in contact with water. Hydrogen, boron, carbon, nitrogen and oxygen atoms are respectively represented in pink, orange, grey, blue and red. During biased trajectories, the H_2O of interest, represented in cyan, has its distance to the surface estimated by evaluating the length between its oxygen and every single surface atom (cyan arrows) and finding the minimal one (blue arrow). Simultaneously the distance of every other oxygen to every boron site is evaluated (green arrows). If the boron-oxygen length is found below 2 Å (dark green arrows), a harmonic biasing force is applied to prevent them from binding. Only a few examples of distances are displayed among the thousands numerically evaluated.

ical consideration, the simulation cell required a tedious equilibration process. Replacing the Nose-Hoover thermostat, the so-called canonical sampling through velocity rescaling (CSVR) thermostat developed by Bussi *et al.*[154] was used with a time constant of 0.5 fs to yield a brutal thermostat. In a first step the system was heated up until it reached 600 K, temperature at which it was kept for 1 to 2.5 ps before cooling down to 323.15 K in a second step with the same thermostat. In a final step the thermostat was switched to the one used for the production runs and the system was thermalized for 1 to 3 picoseconds. This construction procedure was validated by measuring a pressure of 2 ± 3 MPa within the cell following the protocol detailed in section 2.4.1 and applied to 200 snapshots distant by 0.05 ps of a 10 ps representative trajectory.

The starting point of the metastability free trajectories were constructed by adding the

adsorbates and restraining them close to the surface for 2.5 ps. The final step of such a trajectory was used as the starting configuration for the unfavourable chemisorption test after displacing the adsorbed H and thermalizing the system for 1 to 3 ps while restraining the adsorbed water molecule at 1.6 Å from the surface. Similarly to the case of the free energy simulation procedure described in section 2.4.2, starting configurations of biased trajectories were successively obtained after 0.05 to 1 ps of the previous run. The final snapshots of the system with the H_2O restrained at 3.0 and 3.2 Å from the surface were used as the starting point of the free trajectories described in sections 5.4.

The increase size of the simulated systems as compared to the cells used in the AIMD study of the adsorption of OH^- on hBN and graphene raised the computation cost to about 2000 hCPU/ps.

2.5.2   Static DFT

Since static DFT was used to study the co-adsorption of OH^- and H^+ over a limited range (a single surface hexagon) allowing for possible hydrogen bonds to form between the adsorbates, the PBE functional was abandoned for the vdW inclusive so-called optPBE one developed by Klimeš, Bowler and Michaelides[155]. DFT energies used in analysis were obtained after optimising the geometry of systems until forces acting on each atom dropped below 0.05 eV/Å.

Adsorption energies E_{ads} were determined using a similar definition as described in section 2.3.2, with the notable difference that since dealing with neutral systems the reference state could be split into the surface and the H_2O molecule both alone in a simulation cell (see Fig. 2.12):

$$E_{ads} = E(H_2O_{ads}) - E(H_2O_{free}) - E(surface) \qquad (2.26)$$

where the successive terms correspond respectively to the adsorption energy, the energy of the surface and the co-adsorbed OH^- and H^+, the energy of the free water molecule and the energy of the pristine surface, each derived either in vacuum or implicit water.
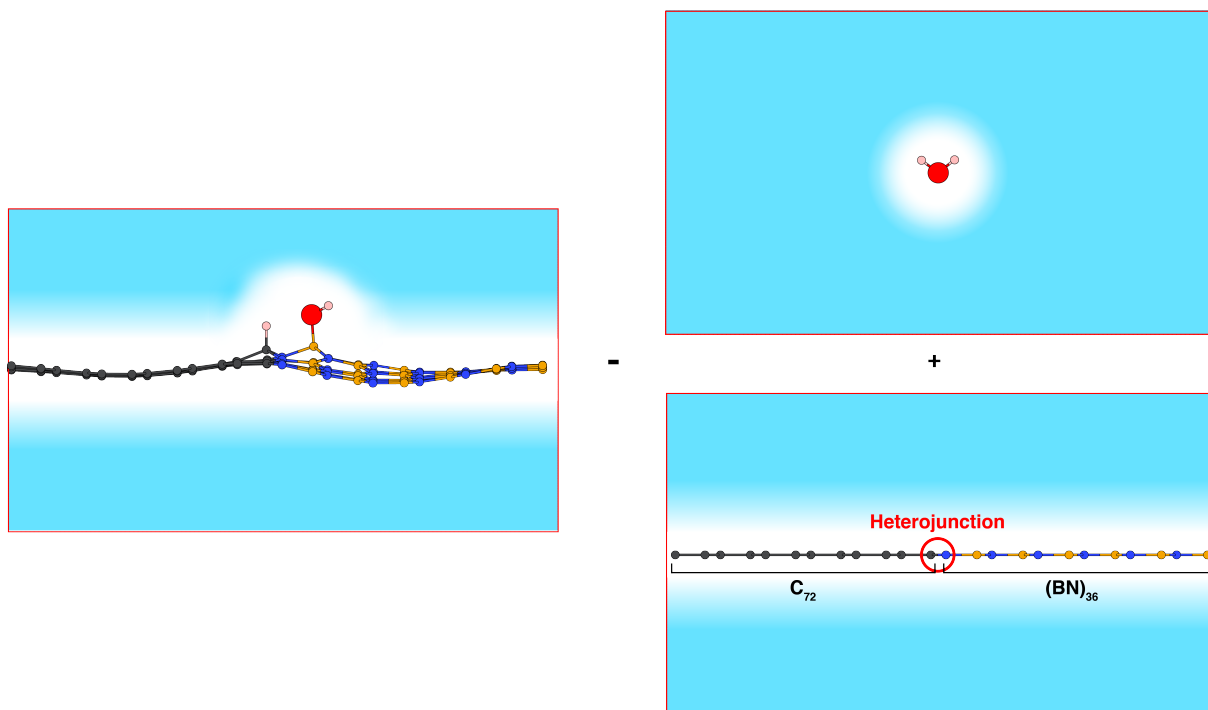
Figure 2.12: **Adsorption Energies Calculation Scheme** Side views of simulations cells used to derive dissociative adsorption energies of H_2O at hBN/graphene heterostructures in either vacuum or implicit water (represented in light blue). Surface with a hydroxide and a proton respectively chemisorbed on a boron and a carbon atom (left), pristine surface (bottom right) and single H_2O molecule (top right). Hydrogen, boron, carbon, nitrogen and oxygen atoms are respectively represented in pink, orange, grey, blue and red. The dissociative adsorption energy corresponds to the difference of the total energies of the right cell with the two left cells.

2.5.3   Derivation of the Free Energy Profile

To obtain the potential of mean force of a water molecule close to the junction, the distance of one particular water oxygen to the surface was restrained using a harmonic bias with a force constant of 0.1 Ha/Bohr. This collective variable was defined as the oxygen distance to the closest surface atom. The target of the restraint was progressively moved from 1.4 Å to 3.6 Å along successive trajectories of 5 ps. The two oxygen-hydrogen bond of the target H_2O were restrained by a harmonic potential centered at 1 Å with a force constant of 0.025 Ha/Bohr. Simultaneously, harmonic biases with a force constant of 0.1 Ha/Bohr were applied to each combination of another oxygen atom and any boron atom to prevent adsorptions (see below).

Restraints were defined and applied using the open-source and community developed PLUMED 2.4 library[156, 157] as implemented in the CP2K 5.1 code. $d_{O^*-surf.}$, the

distance of the interest oxygen atom O* to the surface was defined as the distance to the closest surface atom using the following continuous function as definition:

$$d_{\mathrm{O}^*-surf.} = \frac{\beta}{log\left(\sum_i \frac{\beta}{d_{\mathrm{O}^*-i}}\right)} \tag{2.27}$$

where β is a parameter taken equal to 500, i designates an atom of the surface and d_{O^*-i} the distance between atom i and O*. The derivability of this function is required in order to define a bias. When compared to a discontinuous definition of the distance to the surface (*i.e.* the distance to the closest surface atom), values can slightly vary from the definition of equation 2.27. We chose β in order to minimise the differences obtained with the continuous and the non-continuous definitions. Due to numerical limitations, β can not be set too high (*e.g.* more than 1200).

If below 2 Å, the distances between all boron atoms and all oxygen atoms different from O* are restrained by a harmonic potential with a force constant of 0.1 Ha/Bohr, using the "LOWER_WALLS" functionality of PLUMED. A representative example of a PLUMED input file can be found in Appendix, with only one "lower wall" defined instead of all of them.
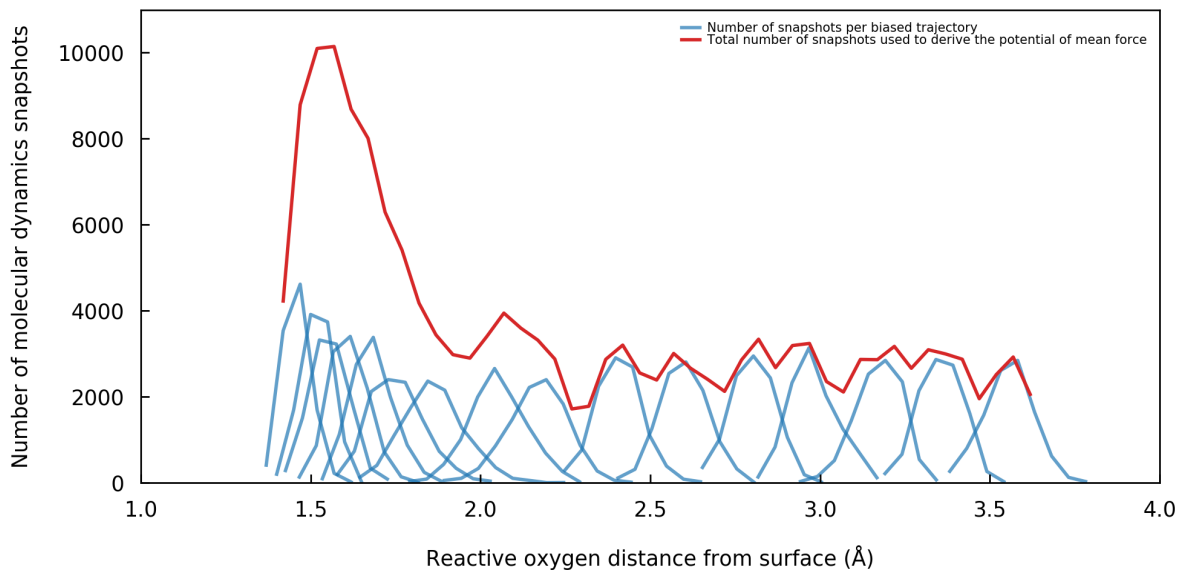
Figure 2.13: Evidence of convergence of the umbrella sampling. Histograms of the probed reactive oxygen distance from surface in terms of number of molecular dynamics snapshots for each biased trajectory (blue) and on overall (red).

To derive the free energy profile, the biased trajectories were analysed using a home implementation of the WHAM algorithm as described in section 2.4.3. A bin size of 0.05 Å was chosen to compute the histograms. Extreme parts of the profile corresponding to bins including less than 1100 snapshots were removed from the analysis. The energy minimum of the basin around 3.3 Å was taken as the reference. Evidence of convergence of the WHAM analysis used to derive the PMF of Fig. 5.4b is displayed in Fig. 2.13.

2.6 Methods for Chapter 6

Unless stated otherwise, computational details correspond to the ones described in section 2.2.

2.6.1 AIMD of the Nanotubes/Water Interfaces

Simulation Cells

The nanotubes simulated correspond to 2 nm diameter (15 ,15) armchair tubes modelled by 300 atoms. The BN nanotube (BNNT) and its carbon counterpart (CNT) were placed in $27.76 \times 27.76 \times 12.55$ and $27.34 \times 27.34 \times 12.30$ Å^3 simulation cells respectively to avoid spurious interactions between periodic images, thus yielding a simulated tube length of 12.55 and 12.30 Å (see Fig. 2.14).

Following the construction procedures detailed in sections 2.4.1 and 2.5.1, the tubes were generated using Virtual NanoLab and later filled using Packmol to create a cylinder of water with such dimensions that a minimum distance of 2.5 Å would exist between the liquid and the solid. Several water densities were tried out in the quest to yield a satisfactorily pressure within the tubes, with a total number of water molecules between 100 and 150. The increased size of the systems raised the computational cost up to 1400-1900 hCPU/ps. Before applying the MD equilibration procedure, VASP was used to perform 100-150 steps of static DFT geometry optimisation on the simulation cells. The systems were then heated up to 600 K for 2.5 ps, cooled down to 323.15 K for 2.5 ps using CSVR thermostat before 0.5 ps of equilibration using the Nose-Hoover thermostat.

a   **b**
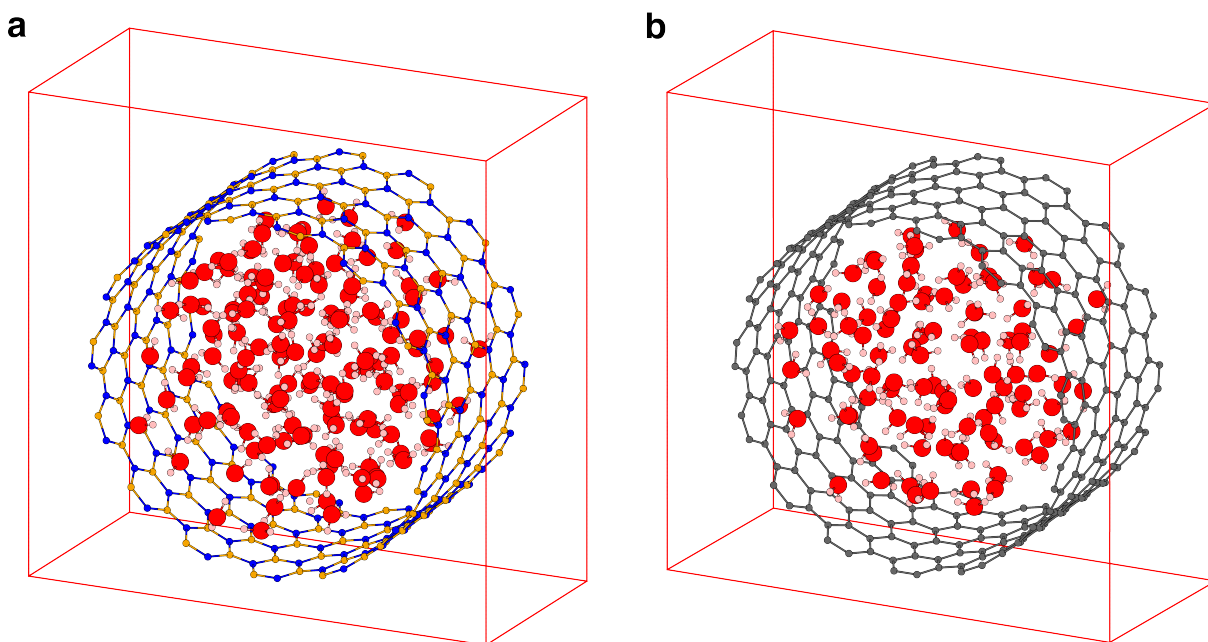
Figure 2.14: AIMD simulation cells of 2 nm in diameter BNNT (a) and CNT (b) filled with respectively 143 and 101 H_2O molecules. Hydrogen, boron, carbon, nitrogen and oxygen atoms are respectively represented in pink, orange, grey, blue and red.

If the difference in number of water molecules from a different simulation did not exceed 15, the last configuration of the previous calculation was used as the starting one for the new trajectory after removing the supernumerary H_2O, leading to shorter equilibration times.

2.6.2   AIMD of the Hydronium at the Interfaces

Simulation Cells

The last configuration of the 50 (47) ps trajectory used to derive water density profile at the hBN/water (graphene/water) without a hydroxide were modified by removal of a OH^- fragment within the first water layer to yield a cell containing the surface, 97 (94) H_2O and one hydronium cation at 3.08 (3.12) Å from the surface, yielding a pH = 0.24. Following the procedure described in section 2.5.1, the hBN (graphene) cell was heated up to 600 K for 3.2 (2.8) ps then cooled down to 323.15 K using a CSVR thermostat during 7 ps before 2 ps of ultimate equilibration with a Nose-Hoover thermostat were performed. During the whole thermalization process the oxygen of the hydronium and a surface atom were frozen while a harmonic restraint centered at 1 Å with a force constant

of 0.05 Ha/Bohr was applied to each of the the three O-H bonds of the cation. The biases were removed at the end of the equilibration to perform the 20 ps free trajectories.

Derivation of the Free Energy Profiles

To determine the PMF of approach of the hydronium to the hBN (graphene) layer, the configuration corresponding to 19.9 (5.5) ps of the free trajectory was taken at the starting point, with a cation-surface distance of 2.64 (2.76) Å. The ion-surface distance as defined in section 2.5.3 was restrained using a harmonic potential with a force constant of 0.05 Ha/Bohr while simultaneously restraining the three O-H bonds of H_3O^+ at 1 Å using the same value for the force constant. The ion-hBN (ion-graphene) distance was first restrained to 2.6 (2.8) Å. It was successively shifted by steps of 0.2 Å until spanning a range of 2.0 to 6.2 Å. The starting configuration of each of the biased trajectory corresponds to 0.5 ps of the previous run, with an additional 0.5 ps equilibration before the 5 and 2.5 ps of data production for hBN and graphene, respectively. The biased trajectory were analysed using the WHAM protocol as described in section 2.4.3.

The orientation of the hydronium along the biased trajectory was measured as the cosine of the angle formed by the closest surface atom to the oxygen, the oxygen itself and the geometrical centre of the three hydrogen atoms. Within this definition, a cosine of +1 and -1 respectively corresponds to the cation with its oxygen pointing away and to the surface.

2.6.3   Reactivity of a hBN Point Defect in Water

All DFT calculations were performed with authorised spin-polarised states as the nature of the defect was not clear at first. This raised the cost of AIMD simulations to about 1500 hCPU/ps.

The last step of the 20 ps unbiased trajectory of a H_3O^+ on top of a hBN sheet was used as the starting point for simulations of the defected ionic material with removal of a boron atom below the cation positioned at 3.08 Å away from the surface. Because of the very high reactivity of the defect towards water, before each free trajectory the system had to

be thermalized with the oxygen of the hydronium frozen, and the three O-H bonds of the cation restrained to 1 Å by a harmonic potential with a force constant of 0.05 Ha/Bohr. Simultaneously, pending nitrogen atoms had their hydrogen coordination restrained to 0, using the bias defined in section 2.4.2 under equation 2.8 with a force constant of 0.05 Ha. To ensure pending nitrogen atoms would not stray away from the BN plane and form strong hydrogen bonds with surrounding water molecules, thus pre-placing the system in a reactive state, the three surface atoms were frozen in an in-plane position upon equilibration. Systems were thermalized in this manner for 1 to 3 ps before each free trajectory.

Chapter 3

Chemisorption of Hydroxide on hBN versus Graphene From Static DFT

A large part of this work has been published in 2016 in the *Journal of Physical Chemistry Letters*[94]. Methodologies and computational details are described in chapter 2, sections 2.2.1 and 2.3.

3.1   Motivation

As previously described (see section 1.2 of chapter 1), recent nanofluidic experiments revealed a tremendous negative charging of boron nitride nanotubes (BNNT) and carbon nanotubes (CNT) while in contact with aqueous saline solutions[35, 36]. Surprisingly the magnitude of the surface charge as well as the charging behaviour with respect to salinity were found to differ between the two crystallographically similar materials. The magnitude of the maximum charging - ranging from 0.1 C / m^2 for C to 1 C/m^2 for BN depending on the solution pH - rules out point defects as the sole origin of the measured surface charging. $1C/m^2$ would indeed correspond to 1 out of 3 surface atoms covered by a monovalent ion. These experimental results therefore call for two challenging questions: (i) what are the potential chemical species present in basic and saline solutions that could adhere on the surface and strongly charge the pristine nanotubes? (ii) how can we explain the different charging behaviour of graphene and BN ideal nanotubes?

A recent DFT study has investigated the dissociation barrier of a water molecule in contact with pristine graphene and BN nano sheets and concluded that the process is highly endothermic with a larger barrier on graphene than on BN[34]. They also proposed facile ways to enhance the dissociation, either via including substitutional defects or either via pre-adsorption of H, again the presence of defects. Here we also consider pristine nano sheets and take into account the presence of hydroxide ions in water. We then demonstrate that adding one electron to these 2D materials permits to tune the adsorption strength of one hydroxide: a strong ionic adsorption on BN and a weak ionic adsorption on graphene. Our atomistic results corroborate the acidity (pK_a) of the BN sheet, pointing to the hydroxide anion as the best candidate to explain the charging of BN material immersed in a saline electrolyte.

3.2   Energetics of First Adsorption

To study the first adsorption of OH^- on one B (or C) atom of the sp^2 BN (graphene) layer, the first chemisorption energy E_{ads1} was computed through the protocol described in section 2.3.2 of chapter 2. The total energy of the adsorbed state was compared to that of the reference state corresponding to the surface and the OH^- at 7.5 Å away from it in such way that a negative energy characterises a favourable adsorption process (see Fig. 2.4.

Table 3.1 summarises the energetics computed within periodic DFT for the first OH^- adsorption on pristine BN and graphene monolayers subjected to different environments. In vacuum the adsorption is strongly favourable with -2.3 eV on the BN layer, while it is less favoured on the graphene layer (-0.5 eV). Comparatively the neutral adsorption computed with spin-polarised calculations leads to similar moderate values (around -0.6 eV) in full agreement with previous studies[34, 158]. Interestingly the adsorption values do not depend on the inclusion, or not, of van der Waals corrections (see $E_{ads1}(vdw)$ in Table 3.1). Indeed, in the final adsorption state the species are short-range bonded precluding vdW interactions, and in the initial desorbed state the species are positioned to avoid any spurious vdW interaction.

OH^- $(OH\cdot)$	BN layer	Graphene layer
E_{ads1}	-2.3 (-0.63, M = 1)	-0.5 (-0.57, M=1)
E_{ads1}^{sol}	-0.89	+.33
$E_{ads1}(vdw)$	-2.1	-0.52
$E_{ads1}^{sol}(vdw)$	-0.9	+.33

Table 3.1: Adsorption energies (in eV) of the first OH^- species onto BN and Graphene layers in vacuum and in implicit water. Negative (positive) values mean favourable (unfavourable) cases. For the adsorption in vacuum, values in parentheses are spin-polarised calculation for the uncharged system, *i.e.* the radical $OH\cdot$ adsorption that induces magnetism in graphene with M the electron magnetism.

In contrast, the adsorption values in implicit water denoted E_{ads1}^{sol} are greatly reduced by $\sim$1 eV, maintaining a favourable adsorption value for BN while turning to an unfavourable adsorption value for graphene. Notably, including the solvent in the DFT modeling permits us to discriminate both materials regarding the adsorption of one anionic hydroxide: BN will spontaneously attach, while graphene should remain inert at least at low temperatures. We note in passing an alternative way to model the adsorption of a charged ligand with zero net charge in the supercell: the insertion of a counterion such as one potassium cation in the vacuum space at long distance from both the adsorbate and the surface. The resulting energetics including the potassium cation are very similar to the charged procedure used here (see section 2.3.4 of chapter 2). Hence the discriminative energetics between the two materials are robust against different modeling schemes of the charging effect.

The detailed geometries of the adsorbed structures are displayed in Fig. 3.1. Side views permit to visualise the sp^3 rehybridisation of the bonding atom inducing an out-of-plane buckling somewhat larger for BN than for graphene. The bonding distances between the O atom and the anchoring site on the substrates are 1.5 Å for BN and 1.54 Å for graphene, typical for single C-O bonds. A pyramidalization angle θ_p[159] can be determined and amounts to 18° for BN and 15° for graphene corresponding to 93 % and 77 % of sp^3 hybridisation respectively. The geometrical differences are not as striking as the energy differences but confirm a weaker adsorption of OH^- on graphene than on BN.

We have investigated the spatial distribution of the additional electron using the Mulliken charge analysis (see section 2.3). It strongly differs between BN and graphene nanosheets
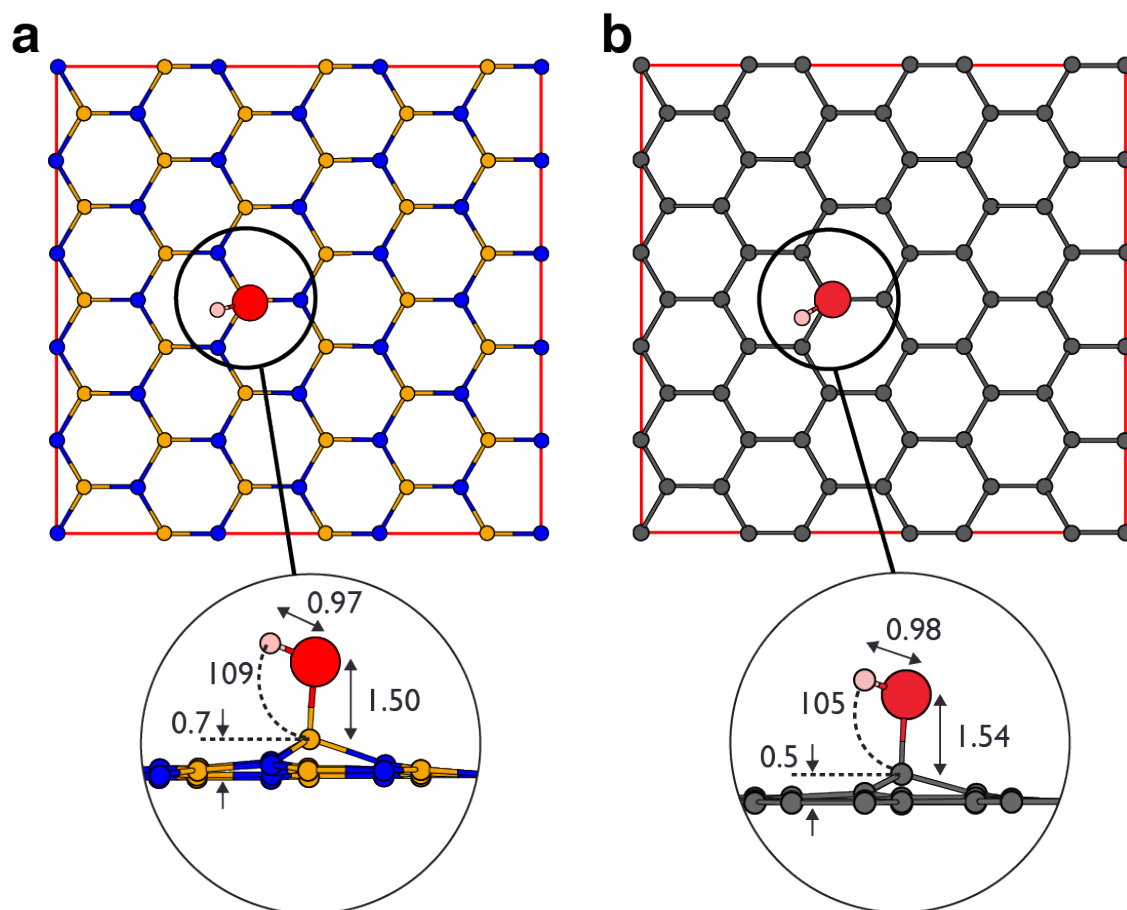
Figure 3.1:   DFT adsorption structures. Top views of BN (a) and graphene (b). Insets with side views of the bonding site for each material with key distances and angles expressed in Å and degrees, respectively. Hydrogen, boron, carbon, nitrogen and oxygen atoms are respectively displayed in pink, orange, grey, blue and red.

(see Table 3.2). According to this analysis the grafted C atom on graphene gains only 0.06 electron, and the rest of the C atoms remain practically non charged. On graphene the additional charge is totally delocalized over the nanosheet, and the possible charge-activating role to bind hydroxyl is therefore masked. In contrast on BN the grafted B gains 0.22 electron and becomes less positively charged than the rest of electron-deficient B atoms. The additional charge on BN is therefore substantially localised on the ligand, and the grafted atom and the local reduction of the binding B atom can explain its improved reactivity. The difference of magnitude for E_{ads1} between graphene and BN as well as evidences of the additional charge distribution therefore points toward a OH^- interaction with BN arising from a significant effect of electrostatics. The disparity between the two twin materials would therefore be in connection with their metallic or ionic character.

Adsorption State	Supercell Charge	BN Layer					Graphene Layer			
		$< Q_\mathrm{N} >$	$< Q_\mathrm{B} >$	$Q_{\mathrm{B}*}$	Q_O	Q_H	$< Q_\mathrm{C} >$	$Q_{\mathrm{C}*}$	Q_O	Q_H
Raw Surface	0	-.35	.35	-	-	-	0	-	-	-
Adsorbed	0	-.35	.35	.17	-.4	.23	0	-.06	-.38	.15
Desorbed	0	-.35	.36	-	-.49	.28	0	-	-.55	.28
Adsorbed	-1	-.35	.33	.13	-.52	.19	-.01	-.06	-.42	.12
Desorbed	-1	-.35	.35	-	-.98	.24	-.01	-	-.78	.25

Table 3.2: Mulliken atomic charges expressed in elemental charge. $< Q_i >$ is the average atomic charge of atoms i and Q_i^* is the atomic charge of the adsorption site. Values are presented for adsorbed and desorbed states of a hydroxyl and a hydroxide on both materials, as well as charges of the pristine surfaces.

3.3   Towards Experimental Conditions

In a quest for determining a maximum surface coverage of hydroxide to yield effective surface charges, we studied the adsorption of a second OH^- ion onto BN and graphene monolayers. Figure 3.2 displays the second adsorption energy in vacuum E_{ads2} (solid lines) as a function of the distance L from the first adsorption site. Circles mark the successive next-nearest neighbours. Because only every two atoms are available for OH^- adsorption on hBN, there are two times more such sites on graphene as compared with BN.

As shown on Fig. 3.2, the addition of a second OH^- ion on the nearest neighbour located in the same hexagon destabilises the adsorption energy by typically ~ 1 eV as compared with the single ion adsorption. It remains favourable for BN (point B) but becomes readily unfavourable for graphene (point A). The second adsorption energy is then found to decrease as a function of the distance L from the first ion. The value reaches a plateau in energy for large distances L, slightly above the first adsorption energy. Typically the plateau is reached roughly beyond $L = 3$ Å for graphene and beyond $L = 5$ Å for BN. Now considering the effect of the solvent, one may observe that it leads to a global destabilising shift for the second adsorption energy, typically ~ 0.3 to 0.5 eV. The difference in energy between the first adsorption and the plateau is however reduced as compared with vacuum. One may attribute this effect to the screening of charge.

Nevertheless all the adsorption energies discussed here are obtained within a static DFT framework at $T = 0$ K, far from experimental conditions: ambient temperature and
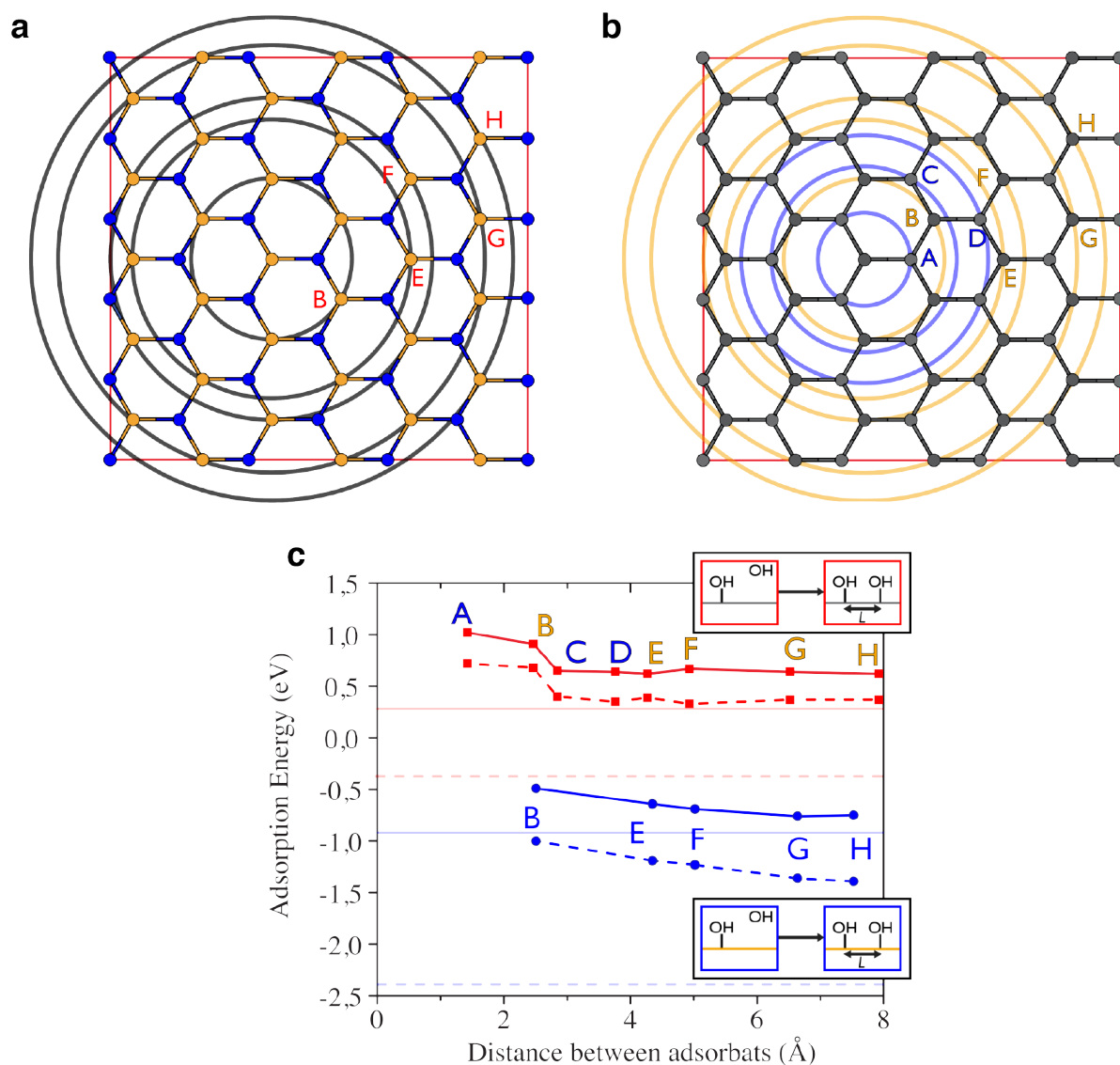
Figure 3.2: a) Circles display possible sites (labelled with letters) for the second adsorption of OH^- at a given distance from the first adsorption site labelled A. b) Same for graphene. c) Adsorption energy of a second hydroxide versus the distance between the two adsorption sites. Results for BN are displayed by circles connected by blue lines while results for graphene are represented by squares connected by red lines. Horizontal lines represent the adsorption energies for single OH^- ions (blue for BN, red for graphene). Plain and dashed lines respectively correspond to adsorptions in implicit water and in vacuum. Boron, carbon and nitrogen atoms are respectively represented in orange, grey and blue.

OH$^-$	BN Layer	Graphene Layer
T(K)		297.15
ϵ_b ($P = 1$ bar)		78.4
E_{ads1}^{sol}	-0.89	+0.33
correction	+0.43	+0.46
$\Delta G_{ads1}(T, P)$	-0.46	+0.79

Table 3.3: Thermodynamic corrections and the Gibbs free energy of first adsorption evaluated in eV at 297.15 K and 1 bar. ϵ_b designates the dielectric permittivity of the solvent. All energies are expressed in eV.

pressure. Yet the DFT energies can be corrected to be relevant at finite temperatures. In the following we therefore compute the thermodynamics of adsorption of OH$^-$ on the BN or graphene layers by taking advantage of successful approaches adapted to solid interfaces[139–141] as described in detail in section 2.3.3 of chapter 2. The correction terms that link E_{ads1}^{sol} to the Gibbs free energy of first adsorption ΔG_{ads1} were evaluated at $T = 297.15$ K and considering a solute standard concentration $c^0 = 1$ mol.L^{-1}. The thermodynamic corrections are summarised in Table 3.3.

As a result, we find a favourable $\Delta G_{ads1} = $ -0.46 eV for BN and a non favourable $\Delta G_{ads1} = +0.79$ eV for graphene. Thermodynamic corrections also worsen the scenario for the carbon material. This result rules out a charging mechanism based on the chemisorption of hydroxides on graphene but permits us to envision it for BN.

We further quantified how the predicted adsorption energies ΔG_{ads1} compare with the surface charge data extracted from the BN measurements by Siria *et al.*[35]. To reason in terms of predominance of chemical species one can extend the definition of pK$_a$ to characterise the exchange of a OH$^-$ instead of a proton, via the autoprotolysis equilibrium of water. In the present case, such pK$_a$ can directly be derived from ΔG_{ads1}:

$$pK_a = 14 + \frac{\Delta G_{ads1}}{k_B T \log(10)}. \tag{3.1}$$

with k_B the Boltzmann constant. As an ultimate result equation 3.1 predicts pK$_a = 6$ for BN and pK$_a = 27.7$ for graphene. The former agrees well with the post-treatment of experimental data[35], in which the electrostatic potential at the surface was evaluated using the Poisson-Boltzmann model, yielding pK$_a = 5.5$ for BN. The value we derive for

graphene is non realistic, precluding the same charging mechanism for graphene.

Our results support the strong reactivity of BN monolayer in the presence of hydroxide anions contained in saline water, with significant surface charge even at neutral pH[35]. The contrasted result on graphene confirms the differential chemical behaviour between the two materials. This echoes the experimental results using nanofluidic tools where much smaller adsorption is found on CNT and planar graphitic surface[36, 160, 161]. Still the presence of a surface charge on CNTs may suggest that other species than OH⁻ could adsorb onto the graphene surface and charge it or that the water self-anion approaches it in a non-covalent manner *i.e.* via physisorption.

To get closer to an estimation of the surface charge using data derived from simulations, a key parameter is the maximum coverage for the ions on the surface. Such a quantity enters the global thermodynamics when considering for example the charge-pH relationship in the experiments. The adsorption equilibrium

$$Surface + \text{OH}^-_{aq} \rightleftharpoons Surface - \text{OH}^-_{ads} \tag{3.2}$$
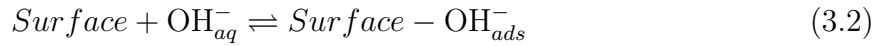
is usually modelled by a Langmuir adsorption model, which introduces a maximal fraction $\theta_{max} < 1$ of B or C atoms (for hBN or graphene respectively) that constitute possible adsorption sites. This value for θ_{max} fixes the maximal charge expected on the surface, which is an interesting quantity *per se*. Denoting θ the fraction of bonded B or C atoms to an adsorbed OH⁻, the chemical potential of the anion at the surface is then modelled as

$$\mu_s = \Delta G_{ads1} - e\phi + k_B T \log\left(\frac{\theta}{\theta_{max} - \theta}\right), \tag{3.3}$$

where ϕ is the electrostatic potential at the surface. The chemical potential of OH− in the bulk at the concentration [OH⁻] expressed in mol.L⁻¹ is fixed at equilibrium by its bulk value:

$$\mu_b = k_B T \log[\text{OH}^-] \tag{3.4}$$

so that

$$\frac{\Delta G_{ads1}}{k_B T} - \frac{e\phi}{k_B T} + \log\left(\frac{\theta}{\theta_{max} - \theta}\right) = \log[\text{OH}^-] \tag{3.5}$$

The equilibrium condition then becomes

$$\log\left(\frac{\theta}{\theta_{max} - \theta}\right) = \frac{e\phi}{k_B T} + \log(10)\,(\text{pH} - \text{pK}_a) \tag{3.6}$$

which relates the surface coverage to pH of the solution and the electrostatic potential at the surface.

A rough estimate for θ_{max} can be done for BN on the basis of our DFT calculations. To this aim, we performed preliminary investigations of further adsorption of subsequent hydroxides on the surface keeping the same minimum favourable distance revealed in Fig. 3.2. First results are presented in Fig. 3.3. Considering a third adsorption on the same hexagon leads to an energetically unfavourable configuration (b). The adsorption of three adsorbates in a row is energetically favourable, although the zigzag configuration (c) is less favourable than the straight segment (d). Finally completing the lines with a fourth adsorbate becomes non-favourable (e and f). Of course these are first configurations and the stability of many other configurations should be evaluated, yet it allows a first estimation of θ_{max}. On the basis of these results, one may estimate that 3 hydroxides can be grafted at most in a rectangle of $(L+l_{3\text{OH}-})\times L$, which amounts to a surface of 50 Å^2, with $l_{3\text{OH}-}$ the distance between 3 hydroxides adsorbed in a line pattern (see Fig. 3.3d). This corresponds to a site density of 0.06 per Å^2, and the associated full coverage site density is ~ 0.18 per Å^2 (30 B atoms per supercell). This leads to $\theta_{max} \simeq 0.33$ and $\Sigma_{max} \simeq 0.96$ Cm^{-2}. These values are in good agreement with the values reported for the maximum charge measured on BN surfaces[35].

In conclusion we have investigated comparatively within *ab initio* DFT framework a monolayer of BN and graphene embedded in implicit water and in contact with one hydroxide anion. We predict a contrasted chemical reactivity for graphene and BN: a chemisorption of OH$^-$ on BN while this mechanism is ruled out on graphene. This striking difference between the two pristine materials is linked to their electronic structure. Furthermore, on the basis of atomistic thermodynamics including all the vibrational contributions to energy and entropy, we have derived a free energy of adsorption of -0.46 eV on BN which corresponds to a pK$_a \simeq 6$, in quantitative agreement with experimen-
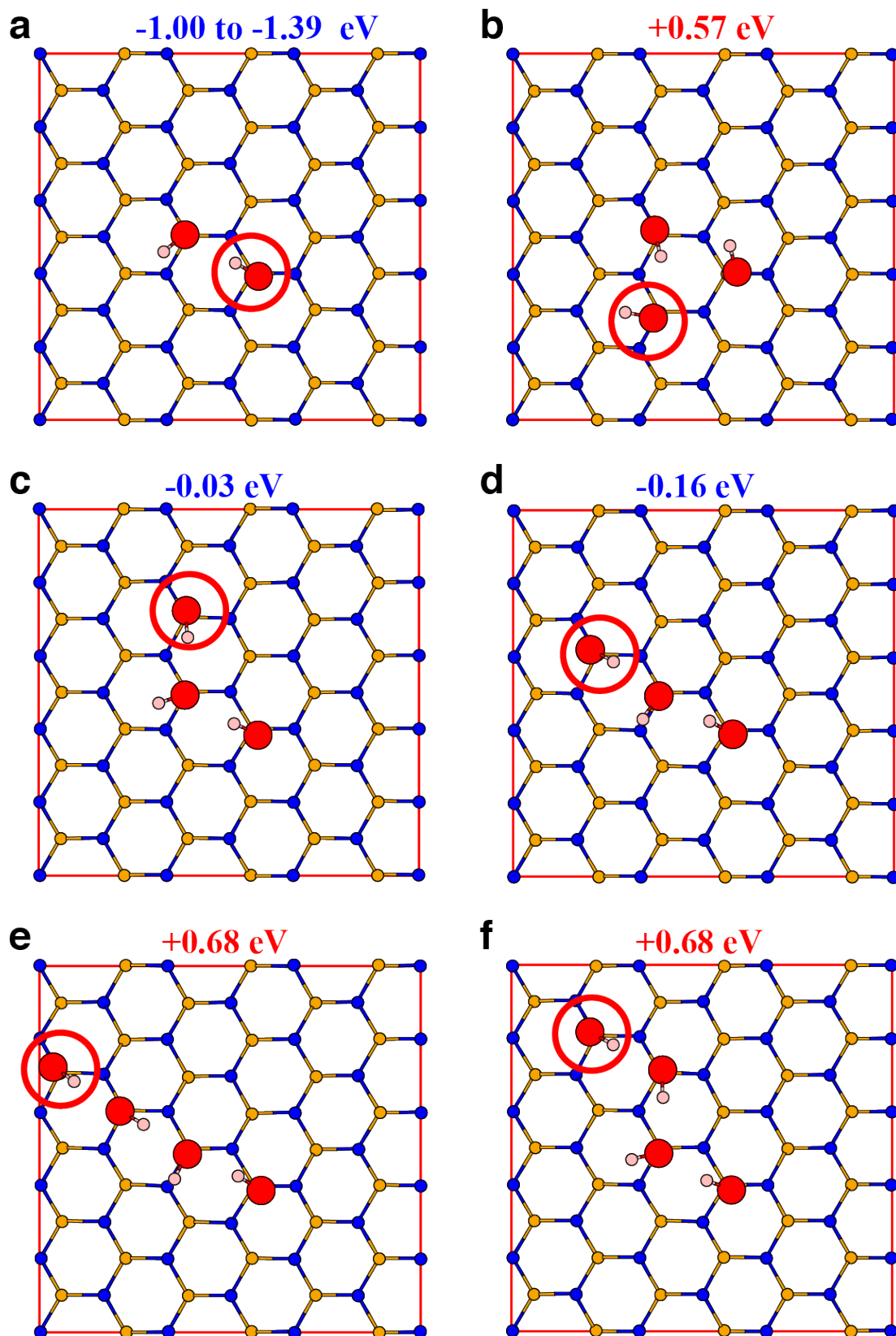
Figure 3.3: Beyond the second adsorption on BN monolayer: from two adsorbates in the same honeycomb (a) exploration of three adsorbates (b,c and d) and four adsorbates (e, f). The indicated energy is the adsorption energy of the last adsorbate, which is identified by a red circle. Hydrogen, boron, nitrogen and oxygen atoms are respectively represented in pink, orange, blue and red.

tal measurements[35]. Hence this charging scenario is viable on BN and our study leans strong support to the recently-revealed non-inertness of the BN material in contact with aqueous saline phase. On the other hand, the case of graphene requires further investigations. Indeed planar graphitic surfaces show minute surface charge (as deduced from surface conductance measurements)[160, 161] while the experiments on carbon nanotubes still exhibits a surface charge[36], although much weaker as compared to BN tubes[35]. This suggests the possibility of either adsorption of other charged species on the carbon surfaces or a too strong approximation being made while modeling the CNT by a single flat layer.

3.4   Effect of Stacking and Curvature

Experimentally the surface charge is observed on multiwall nanotubes *i.e.* consisting of nested tubes[35, 36] interacting via vdW interactions. As either vdW stacking or curvature or both can reasonably be expected to affect adsorption properties the impossibility of carbon charging via chemisorption of hydroxides might be an artefact due to working on flat single layers. To address this issue and establish if the OH$^-$ interaction with carbon is enhanced in different sp^2 structures, the adsorption energies in vacuum were also derived for double layers graphite and BN as well as single wall CNTs and BNNTs of various chiralities and are summarised in Table 3.4. A minute effect of the addition of another

Substrate	Adsorption Strength (eV)
BN Single-Layer	-2.23
Graphene Single-Layer	-0.5
BN Double-Layer	-2.25
Graphene Double-Layer	-0.47
Armchair BNNT, internal	-3.27
Armchair BNNT, external	-3.87
Armchair CNT, internal	-0.21
Armchair CNT, external	-1.08
Zigzag CNT, internal	-0.16
Chiral CNT, internal	-0.14

Table 3.4: Adsorption energies in eV in vacuum of a single hydroxide on different BN and carbon substrates.

BN (graphene) layer in a AA' (AB) stacking (see Fig. 3.4) was obtained with a difference below 30 meV as compared to adsorption energies on single layers.

Zigzag, armchair and chiral geometries were considered by modelling respectively (13, 0), (8, 8) and (10, 5) tubes with a corresponding diameter of about 1 nm, therefore yielding an extreme estimate of the curvature effect, the radius of tubes used in nanofluidic experiments ranging from 3 to 40 nm[35, 36]. Although the geometry of the experimental set-up allows solely for adsorption on the inner wall of the central tube, the effect of both concave and convex curvature was determined by adsorbing the OH$^-$ respectively inside and outside the modelled nanotubes (see Fig. 3.5). Because the chirality of tubes can be crucial for the metallicity of the CNT and therefore for its reactivity but is expected to have minor effect on the adsorption properties of the ionic BNNT, different tube geometries were only tested for the carbon material. Finding a negligible effect of chirality on the internal adsorption strength on a CNT, external adsorption was only studied for the armchair tube. Including or not spin-authorised states in the DFT calculations for the different geometries of CNTs lead to identical adsorption energies. Interestingly a strong effect of the curvature was observed with a significant difference in magnitude between the two twin materials. An enhancement of the adsorption strength of about 1 eV was observed for BN against a maximum one of about 0.5 eV for its carbon counterpart. Furthermore the internal or external character of the adsorption respectively lead to a enhancement and a decrease in reactivity of the CNTs towards OH$^-$ while in both cases the BNNT was found more reactive than the flat BN surface. This is likely due to the ionic and covalent natures of the two materials. Curvature changes the cost of hybridising a surface atom into a sp^3-like configuration by pre-hybridising it for an adsorption on the outer surface of the tube. However for internal adsorption the curvature hybridises surface atoms in the wrong direction and while this leads to the need for a stronger distortion of covalent bonds in the case CNT hence an increased cost, it might be that a boron site solely necessitates to stray away from its flat configuration to be activated as ionic bonds are less directional than covalent ones. The observation of the effect of pre-hybridising the adsorption site is consistent with recent DFT findings which reveal an enhancement of
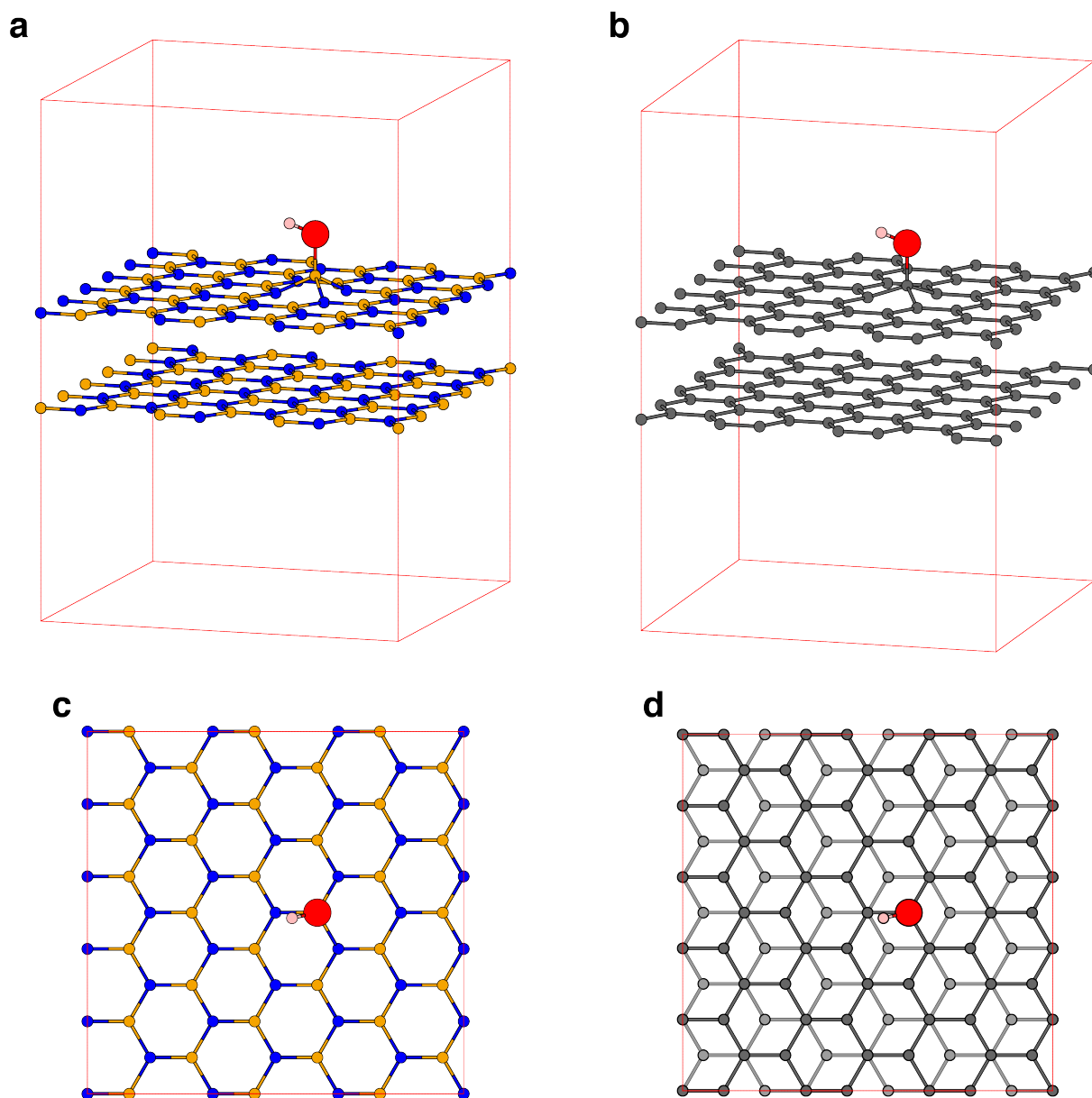
Figure 3.4: Side (a, b) and top (c, d) views of a hydroxide adsorbed on BN (a, c) and graphene (b, d) double layers in AA' and AB stacking respectively. Hydrogen, boron, carbon, nitrogen and oxygen atoms are respectively represented in pink, orange, grey, blue and red.

the adsorption strength of a radical hydroxyl on hBN and graphene single-layers when a hydrogen is chemisorbed on a neighbouring atom and on the opposite side of the surface, causing the OH$^.$ adsorption site to pre-hybridise[34].

While the strong effect on the energetics of chemisorption of OH$^-$ on BN strengthens the conclusion of the present static DFT study, the shift of adsorption energies in the case of carbon nanomaterials is towards the wrong direction but for the reaction on the outside of CNTs, with the latter case leading to a reactivity enhancement of $\sim$0.5 eV, still insufficient to dramatically change the Gibbs free energy of adsorption ($+$ 0.79 eV) into a favourable value.

Thus by studying the effect of stacking and curvature of the carbon nanomaterials on adsorption energies we ruled out a charging mechanism based on the chemisorption of hydroxides. As stated above another plausible origin could be due to interaction with other dissolved species such as CO_2 acid/base ions. A few static DFT tests on these species were performed and yet incomplete they pointed toward an insufficient interaction with the surfaces to explain their charging. Additionally the simplicity of the experimental solutions (KCl in water with a pH regulated by HCl and KOH) as well as the very clear dependence of the experimental surface charge with pH remains major advocates for the involvement of hydroxides at the carbon/water interface. We therefore envision that OH$^-$ could charge the surface without forming chemical bonds with it *i.e.* via a physisorption state which would require comprehensive description of the water solvent to be correctly modelled. Such simulation necessitates a dynamic picture of the chemical system which static DFT is unable to capture to the contrary of molecular dynamics as illustrated by the following chapter.
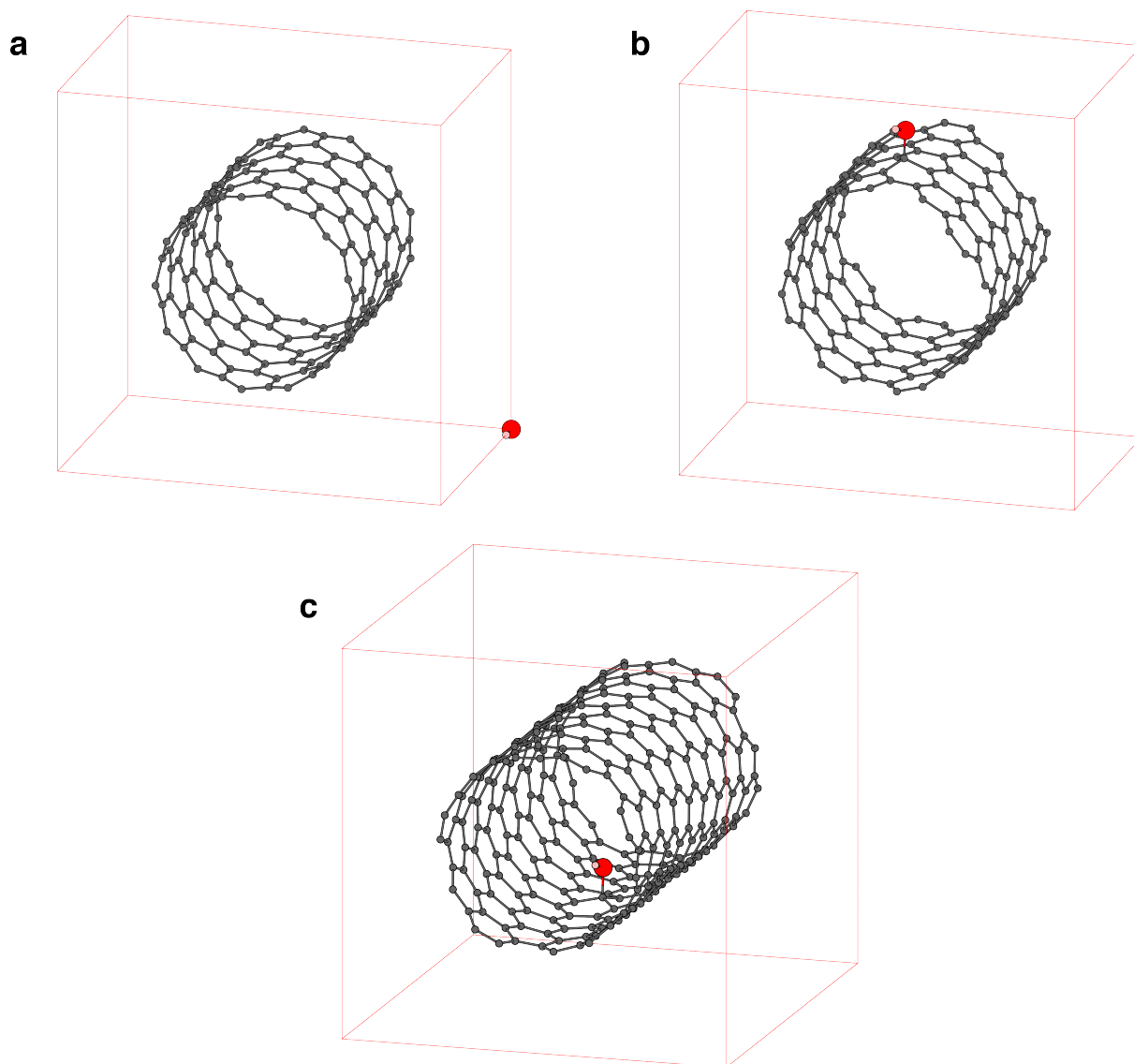
Figure 3.5: Simulation cells of a zigzag CNT in the adsorption reference state (a), arm-chair CNT in the external adsorption state (b) and chiral CNT in the internal adsorption state (c). Hydrogen, carbon and oxygen atoms are respectively represented in pink, grey and red.

Chapter 4

Ab Initio Molecular Dynamics of OH$^-$ at the Interfaces

A large part of this work has been published in 2019 in *Nature Communications*[95]. Computational details and methodologies, in particular concerning the derivation of potentials of mean force, are described in chapter 2, sections 2.2 and 2.4.

4.1 Motivation

In the preceding chapter we have shown using static DFT calculations in implicit water and adapted thermodynamic corrections that aqueous OH$^-$ chemisorbs on hBN under ambient conditions but is not expected to form a chemical bond with graphene therefore leaving unresolved the question of the charging of carbon nanomaterials in contact with water. As pointed out the implicit solvation scheme misses the description of hydrogen bonds, primordial for an accurate description of liquid water. Molecular dynamics (MD) can provide explicit representation of such solvent and previous theoretical explorations of the behaviour of hydroxide ions at hydrated graphenic surfaces were developed at the semi-empirical level using classical dynamics simulations[84]. However this level of modelling cannot correctly describe OH$^-$ in a hydrogen-bonded water network as it is eager to capture a proton from neighbouring water molecules via the Grotthuss mechanism. One key challenge in this quest is therefore to properly simulate interfacial OH$^-$ ions in

water, whose identity remains elusive due to the Grotthuss mechanism: this requires an electronic description of the charged hydroxide species, as well as the surrounding water molecules and the reacting surface. Only computationally expensive *ab initio* molecular dynamic (AIMD), where the nuclei are classically propagated according to forces obtained from an *ab initio* electronic structure theory, are able to comprehensively reproduce the subtleties of the chemistry of OH⁻ at interfaces as illustrated by the numerous AIMD studies of the intrinsic reactivity of hydroxide in bulk water [63–67, 162–167], which made considerable progress lately. Despite a dependence on the type of density functional theory (DFT) functional, the current consensus is that of OH⁻ generally forming two hydration states in bulk water with three or four hydrogen bonds donated to the hydroxide oxygen respectively (the latter state being called hypercoordinated). Proton transfer is facilitated when OH⁻ is receiving three hydrogen bonds, but hindered with four bonds. However simulating accurately the free energy of adsorption of hydrated hydroxide at interfaces is challenging and has been limited to date to the water/air interface[166, 168, 169]. Herein we report AIMD-based calculations of the free energy of a hydroxide at the water-graphene and the water-BN interfaces, considering that the clear experimental pH dependency of the surface charge infers a charging due to the anionic self-ion of water rather than its hydronium counterpart. Using advanced biasing methodologies we compute the potential of mean force (PMF) of the OH⁻ approaching both interfaces from a fully solvated situation mimicking that of bulk water to the chemisorption of the anion, in order to comprehensively describe the distribution of hydroxides in the interfacial region and connect it to the chemisorption results of the preceding chapter.

4.2   Potential of Mean Force

4.2.1   Protocol

The difficulty to compute a PMF as a function of hydroxide-surface distance using restrained sampling methods lies in the reactive nature of OH⁻. As illustrated in MD movies described in section 4.3, frequent proton transfers from a solvating water molecule result
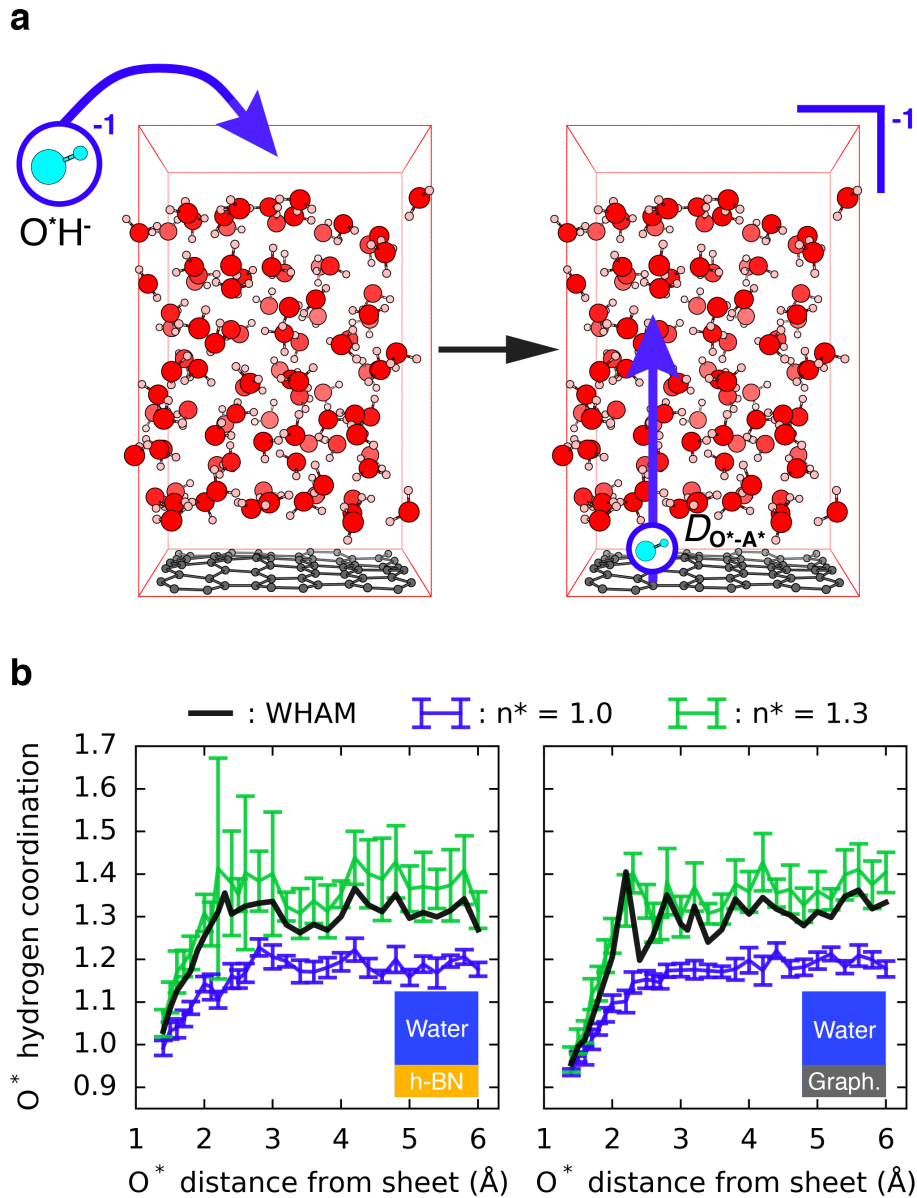
Figure 4.1: Simulation cell and protocol. a) Simulation cell: an anionic hydroxide is placed in a 12.83 Å × 12.35 Å × 21.0 Å orthorhombic cell containing a 60 atoms hexagonal graphene sheet in contact with a hundred water molecules (left) resulting in a charged cell (right) in which the hydroxide is progressively displaced (blue vertical arrow) from the surface to the bulk. The hydroxide, hydrogen, carbon and oxygen atoms are respectively represented in cyan, pink, grey and red. b) Free energy or Potential of Mean Force (PMF) simulation strategy for the water/hBN and water/graphene interfaces in the constraint's landscape. For each fixed distance of the hydroxide oxygen O^* from the sheets, two MD runs are performed while restraining the hydrogen coordination of O^* by a harmonic potential with a target of respectively $n^* = 1.0$ (blue curve) and $n^* = 1.3$ (green curve). The two sets of MD simulations thus obtained are represented by the mean hydrogen coordination and fluctuations around the mean (standard deviations as error bars). They are later combined into a third trajectory labelled WHAM (black curve) using the WHAM protocol at each ion-surface distance independently.

in a discontinuous motion of the hydroxide species during MD and subsequent loss of information regarding the identity of the hydroxide oxygen O^*. In order to keep track of the anion, one needs to apply two simultaneous constraints on O^* during the simulations: its spatial location with respect to a surface atom and its hydrogen coordination value. Figure 4.1a displays the simulation box where one hydroxide with no counterion is inserted into a water/graphene interface (water/hBN interface not shown) equivalent to an anion concentration of 0.57 M. We proposed an original PMF protocol as compared to others[166, 170] schematised in Fig. 4.1b that we summarise hereafter. The procedure is thoroughly detailed in chapter 2 section 2.4. The anion-surface distance $D_{O^*-A^*}$ is fixed by a constraint and is progressively varied by fixed values starting from the surface until the hydroxide has reached the bulk. The hydrogen coordination of the anion oxygen n_{O^*-H} is determined using a switch function (see Fig. 2.6) and is restrained around a target value n^* by applying a harmonic potential. Because of the hydroxide solvation varying between the surface and bulk water, its mean coordination takes up values respectively corresponding to 1.0 and 1.3 (see Fig. 2.7). Two sets of MD trajectories were therefore computed with $n^* = 1.0$ and $n^* = 1.3$, respectively represented by blue and green plots in Fig. 4.1b. In order to obtain the effective coordination per distance to the surface and accordingly deduce the free energy profile, we apply for each surface-anion distance a standard debiasing method based on the Weighted Histograms Analysis Method (WHAM)[144, 145] to the two sets of constrained MD runs (see section 2.4.3 of chapter 2). This yields an intertwined set of trajectories labelled WHAM (black lines in Fig. 4.1b) along which thermodynamic integration is performed to obtain the free energy profile (see section 2.4.3 of chapter 2).

4.2.2   Results

The resulting PMF curves are shown in Fig. 4.2a for hBN (top) and graphene (bottom) as a function of $D_{O^*-A^*}$ together with statistical error bars. While both free energy profiles yield positive surface excesses of hydroxides (see chapter 2, section 2.4.3), there are striking differences between the two interfaces.
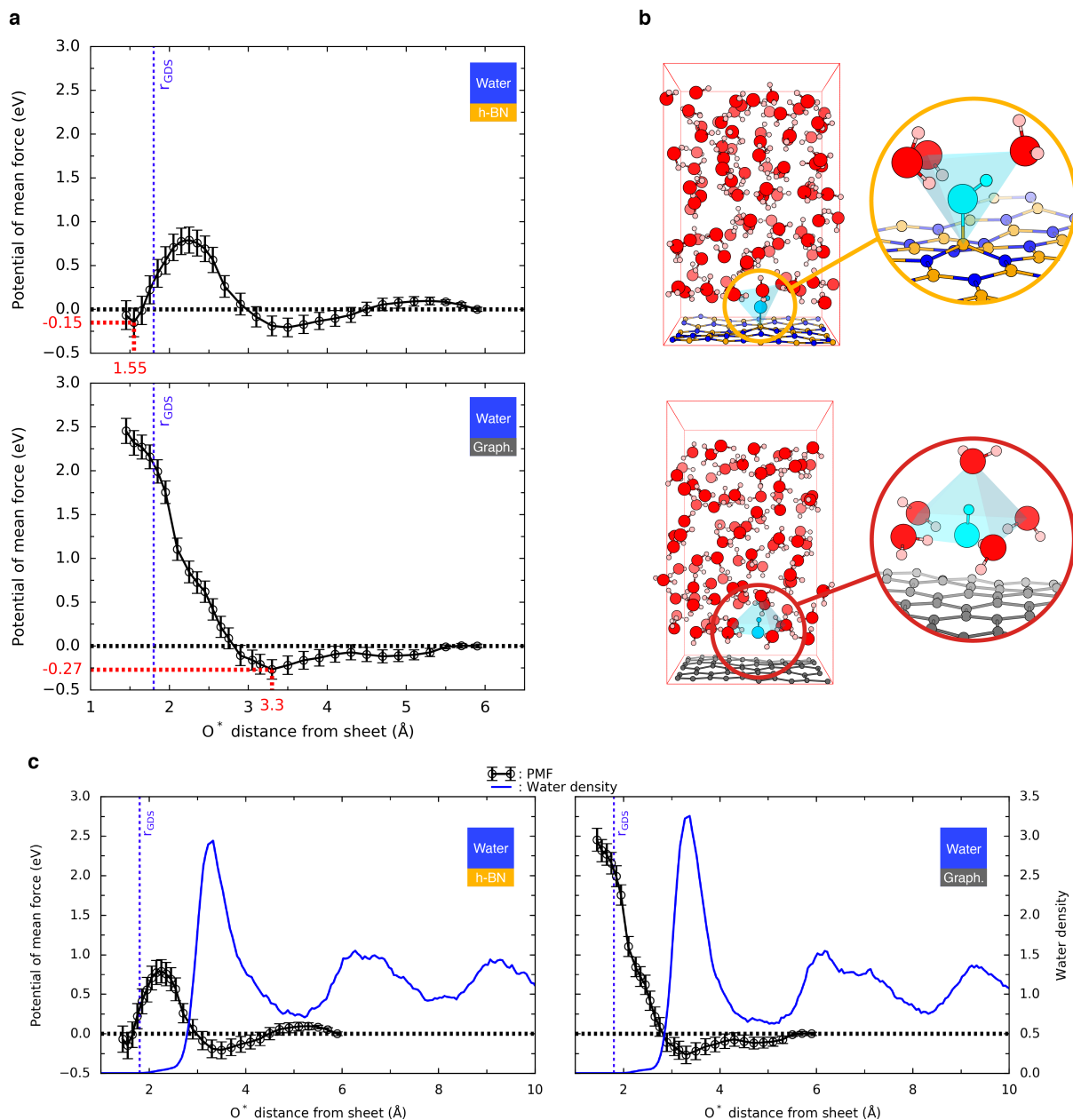
Figure 4.2: Free energy profiles and stable configurations. a) Potentials of mean force of an aqueous hydroxide $(O^*H)^-$ with respect to the O^* distance from the hBN (top) and the graphene (bottom) sheets. The position of the Gibbs dividing surface (GDS), derived by adapting the calculation of ref.[149], and the position of the free energy reference are respectively indicated by vertical blue and horizontal black dotted lines. Error bars correspond to standard deviations. b) Atomistic configurations corresponding to the chemisorbed hydroxide on hBN (top) and the anion physisorbed at 3.9 Å from graphene (bottom) are displayed with details of the solvation shells (insets). The hydroxide, hydrogen, boron, carbon, nitrogen and oxygen atoms are respectively represented in cyan, orange, grey, blue and red. c) Reproduction of the potentials of mean force of hBN (left) and graphene (right) alongside the density profile of water normal to the surface (blue plain line).

For hBN two minima are obtained: the first minimum is a stiff well at 1.5 Å lying at -0.15 ± 0.19 eV corresponding to a chemisorbed state predicted earlier (see chapter 3)[94] and in agreement with numerous examples of covalent hydroxylation of hBN[26, 39–57]. The second minimum is a shallow one at 3.5 Å lying at -0.21 ± 0.13 eV corresponding to a physisorbed state. The two adsorption states are separated by a free energy barrier of 0.79 ± 0.17 eV.

For the graphene surface, there is a large repulsion wall at close distance in line with the results of chapter 3[94] and a physisorbed state at 3.3 Å and -0.27 ± 0.13 eV. Interestingly the superposition of the water density on the PMF plots (see Fig. 4.2c) demonstrates that the first physisorption well on graphene matches the closest water layer while the chemisorption well on hBN lies beneath this first layer. An atomistic snapshot of the anion in both states illustrates one instant of the dynamical solvated picture: in Fig. 4.2b top panel, the hydroxide anion is chemically bonded to a boron atom and is at the centre of a tetrahedron formed by a covalently bonded boron atom and three higher-lying water molecules - two hydrogen bond donors and one hydrogen bond acceptor. In Figure 4.2b bottom panel, the hydroxide anion lies at the centre of a square planar complex formed by four H-bond donor water molecules lying in the first layer above graphene. A fifth water molecule lying further at the upper apex can also dynamically enter the solvation shell, thus forming a square pyramidal environment. In the latter solvation structure close to graphene, the hydroxide is greatly stabilised by around 11 $k_B T$.

Interestingly the continuous and smooth definition of the hydrogen coordination n_{O^*-H} of the hydroxide leads it to probe both the covalent and first solvation shells of O^* so that it includes information regarding solvent organisation in the vicinity of the anion. However this yields non-integer values of n_{O^*-H} comprised between 0.9 and 2 that can not be used for clear observations regarding the solvation shell of the hydroxide beyond identifying an overall increase or decrease of the solvation of the anion. To allow clearer observations on the solvation shell, similarly to n_{O^*-H}, one can define the oxygen coordination of O^*, n_{O^*-O}, using a coarser switch function -as no bias is meant to be derived from it- to
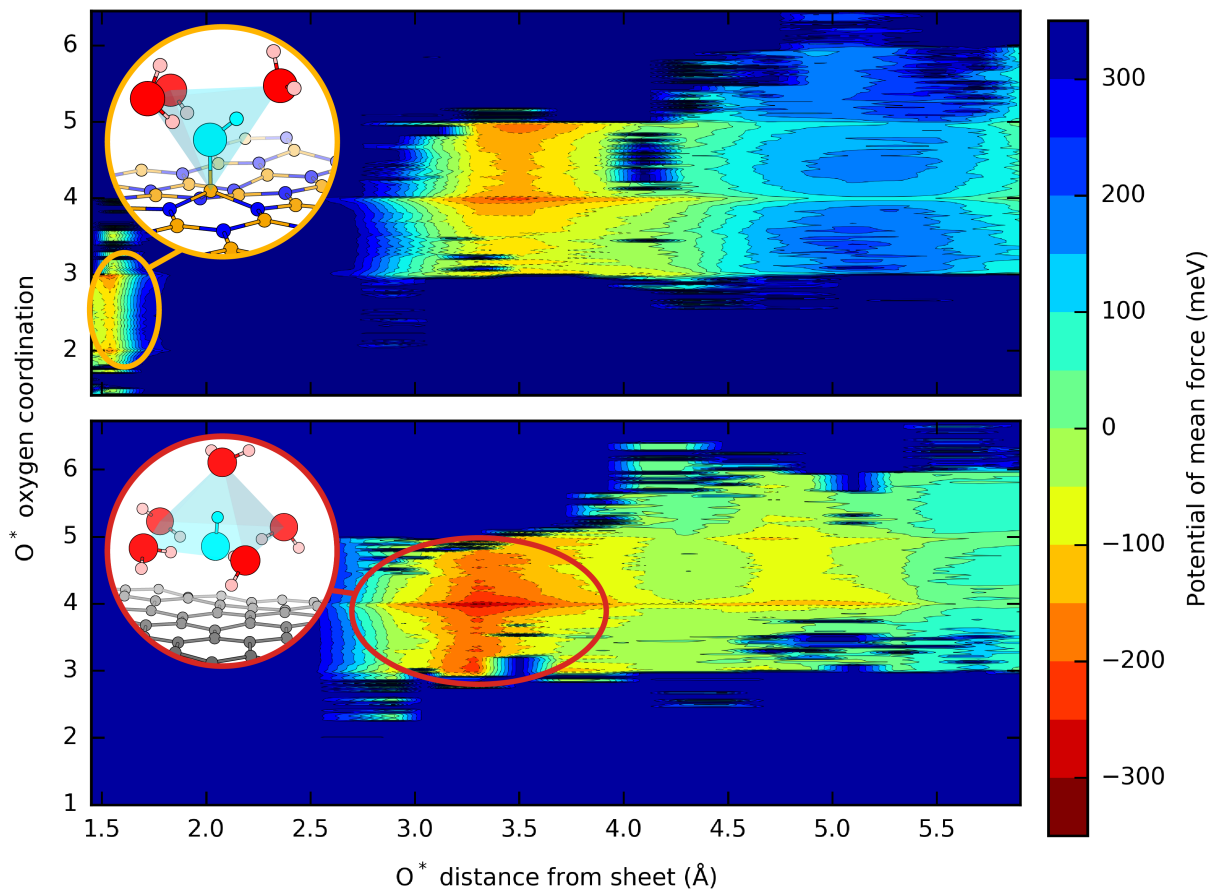
Figure 4.3: Free energy profiles of the anion with respect to its oxygen coordination and its distance from a single layer hBN (top) and graphene (bottom). The solvation configurations in insets correspond to the regions identified by ellipses: chemisorption on BN (top) and physisorption on graphene (bottom), with the hydroxide, hydrogen, boron, carbon, nitrogen and oxygen atoms respectively represented in cyan, pink, orange, grey, blue and red.

yield more comprehensible coordination numbers. The treatment described in section 2.4.3 (chapter 2) was applied to n_{O^*-O} to map the free energy of the hydroxide with respect to $D_{O^*-A^*}$ and n_{O^*-O} (see Fig. 4.3). Contrary to n_{O^*-H}, n_{O^*-O} mainly probes the first solvation shell of OH$^-$, taking near-integer values corresponding roughly to the number of solvating water molecules. One can therefore observe that while physisorbed the hydroxide is mainly solvated by four water molecules (in a square planar geometry) but it can dynamically be surrounded by either three (when the square planar environment is distorted) or five solvating molecules (when a molecule approaches close enough in apex position of a square planar pyramid to be accounted in the oxygen coordination, see the red inset). While chemisorbed on hBN, the oxygen coordination of the anion oscillates

between two and three as the H-bond acceptor solvating molecule moves closer or further from the hydroxide while two H-bond donors remain at short distances (see the orange inset).

4.3   Bias-Free Dynamics

Our computed PMFs infer a fresh view of the graphene and hBN interfaces in water and we also questioned the stability of the physisorption structures after removing all constraints. The resulting bias-free MD runs of 20 ps are visible in movies to which links are provided in Fig. 4.4. Figure 4.4a and c shows the corresponding time evolution of the distance of the hydroxide from the surface (black curve): the O^* lies mainly around 3 Å away from the sheet with some residence time at 4 Å . In Figure 4.4b the lateral displacement - x, y trajectory - of the hydroxide is displayed with colour codes corresponding to the changing index of the O^* atom. It can be seen that the hydroxide is not fixed in the xy plane and diffuses through proton transfers. The colour range permits to evaluate the average number of different oxygen atoms carrying the proton hole (about 10 in 20 ps time for graphene and two times more for hBN). The physisorption features of the PMFs were therefore further confirmed by the bias-free dynamics. The presence and absence of a chemisorption well in the respective cases of hBN and graphene were also successfully checked as illustrated by the corresponding movie which displays 500 fs of bias-free dynamics of the systems thermalised in a chemisorption. While the hydroxide remains bonded to the hBN layer the whole 500 fs (and longer as no spontaneous desorption was ever observed in the present study) it immediately leaves the graphene surface. All movies were generated using the Visual Molecular Dynamics (VMD) software[133–135].

The self-diffusion coefficients of the hydroxide were derived from the 20 ps physisorption trajectories by applying the Einstein equation with computed mean square displacements (see chapter 2, section 2.4.3). Both the lateral and the vertical diffusions of the anion in the vicinity of the surfaces were determined. A hydroxide in bulk water was also simulated as a reference system to compare with the interfaces, using the same DFT dynamics framework. The isodirectional diffusion coefficient of a hydroxide in bulk water was ob-
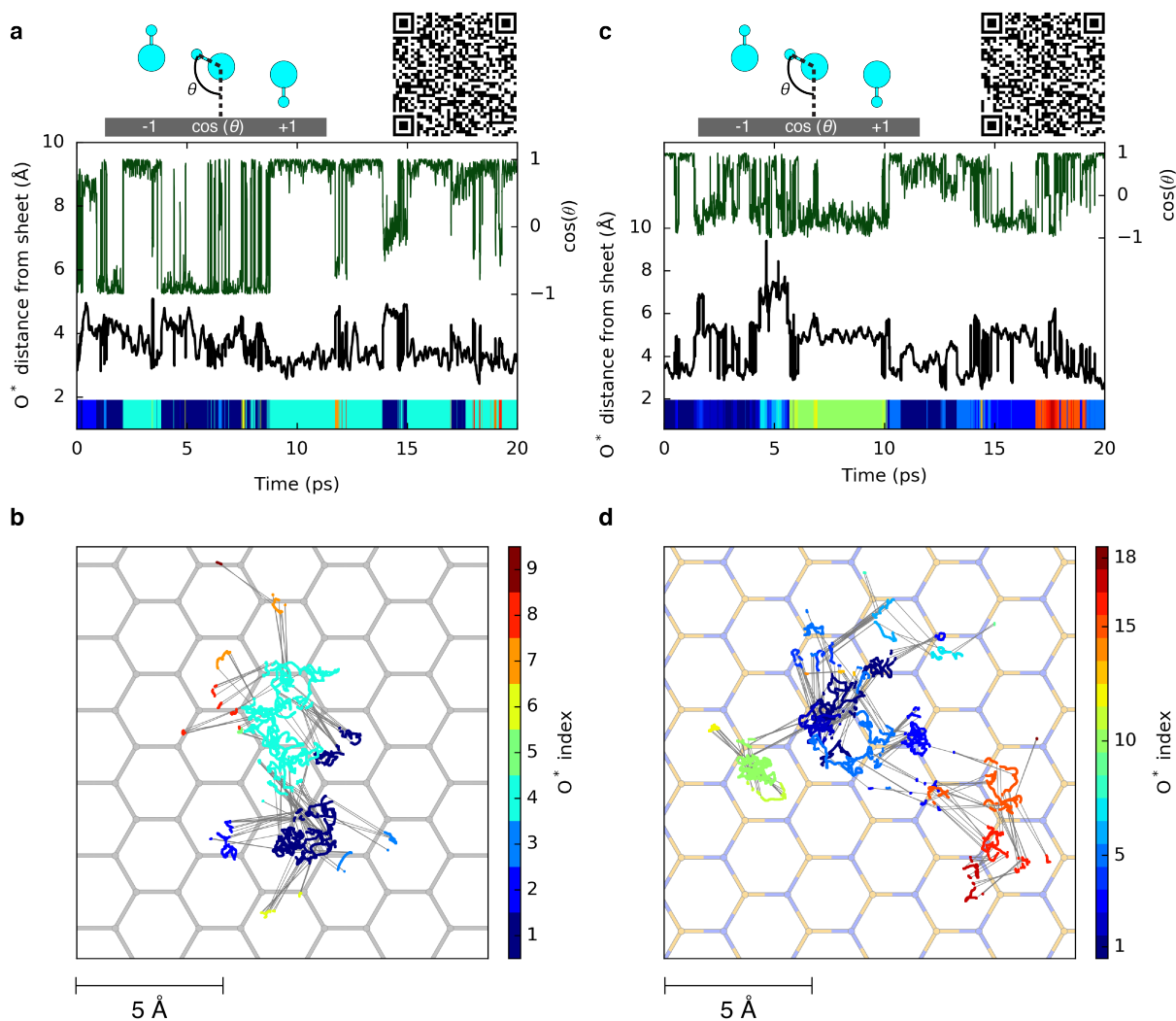
Figure 4.4: Unbiased displacements of OH$^-$ on graphene (a, b) and hBN (c, d). Time variations of the vertical displacement (a and c, black curves) and lateral displacement (b and d, coloured trajectories) of a free hydroxide starting at the physisorption distance from a single-layer. The cosine of the hydroxide orientation with respect to the surface is also plotted versus time (a and c, dark green curves). The index of the hydroxide oxygen O* is associated to a specific colour so that changes of colour represent successive proton transfers in time and hence hydroxide diffusion. Colour scale is different in b) and d). Proton transfers are also indicated by thin grey straight lines on top of the hexagonal grids (b and d). QR codes provide access to movies of the two trajectories, accessible via the following links: physisorption on graphene, physisorption on hBN.

Medium	Conditions	$D^{//}$	$D^{\perp}$	D^{iso}
hBN	PBE-D3	$\mathbf{7.10 \pm 1.62}$	$\mathbf{0.46 \pm 0.65}$	
Graphene	PBE-D3	$\mathbf{12.00 \pm 3.95}$	$\mathbf{0.07 \pm 0.11}$	
D$_2$O	PBE-D3			$\mathbf{4.46 \pm 1.31}$
D$_2$O	PBE			18.2 ± 3.7[67]
D$_2$O	PBE-TS			8.3 ± 1.6[67]
D$_2$O	PBE0-TS			3.7 ± 0.4[67]
H$_2$O	Exp.			5.4[67, 68], 5.2[67, 69]
D$_2$O	Exp.			3.2[67, 68], 3.1[67, 69]

Table 4.1: Computed and experimental diffusion coefficients of OH$^-$ in various media and conditions (units: 10^{-5}cm^2.s^{-1}). $D^{//}$ and $D^{\perp}$ respectively correspond to lateral and vertical diffusion with respect to the surface, while D^{iso} refers to isodirectional diffusion. Values obtained in the present work are written in bold font and the corresponding errors (standard deviations) were estimated by block analysis of linear regressions over mean square displacements of the anion.

tained from a 50 ps MD trajectory. The obtained values are in qualitative agreement with both experimental and simulation data from the literature (see Table 4.1)[67–69]. In particular a value of 0.49 ± 0.15 10^{-5}.cm^2.s^{-1} was obtained for the self-diffusion coefficient of D$_2$O, in the range derived previously by PBE-D3 based AIMD[147, 148]. Interestingly, although the diffusion of OH$^-$ at the hBN/water and graphene/water interfaces is vertically confined, its 2D motion remains in the same order of magnitude of that of the anion in bulk water, corroborating the picture of a mobile ion physisorbed on the hexagonal layers.

How to understand that fast proton transfer do not allow for hydroxide diffusion away from the graphene interface? The answer arises from the existence of hydrogen bonds within the first water layer as observed at water-vapour interfaces[171] and from a particular orientation of the hydroxide at the graphene-water interface. Indeed in Figure 4.4a and c the cosine versus time of the hydroxide tilt angle with respect to the surface (green curves) shows that the hydroxide can adopt two orientations with cosine values close to -1 and $+1$ (especially visible in the case of graphene), corresponding to two H-up (outwards the interface) or H-down (inwards the interface) conformations respectively. Notably in the H-down state -corresponding to cosine equals 1- the oxygen lies closer to the interface than in the H-up state (see Fig. 4.4a, c and corresponding movies).

When a hydroxide is lying H-down in close vicinity to the graphene, it can accept a

proton from a H-bond donor water molecule lying above the anion but still remaining in the first water layer. After the proton transfer, the hydroxide ion is then found H-up and lying further away from the graphene sheet so that it can only accept protons from water molecules below, closer to the surface, but not from water molecules in the second layer from the surface. As a result, the hydroxide diffuses rapidly via flip-flop moves within the hydrogen bond network of the first water layer and its transfer to the second water layer is kinetically hindered. Note that in the case of hBN, we find a slightly different picture with a smoother distribution of cosine angles enhancing the number of proton transfers by a factor of two during the 20 ps MD trajectory exploring a surface roughly two to three times larger than it does on graphene, yet with the hydroxide still mostly oriented perpendicularly to the surface.

It is also interesting to compare the solvation picture of the hydroxide ion described above to other environments. Figure 4.5 compares the radial distribution functions for physisorbed hydroxide on hBN (blue), chemisorbed hydroxide on hBN (orange), physisorbed hydroxide on graphene (red), hydroxide in bulk water (black) and H_2O molecule in bulk water (green). Integrals of $g(r)$ are superposed with dashed lines to quantify the number of water molecules in the solvation shells. Our results for the bulk systems agree well with the literature: the hydroxide (water) is found five-fold (four-fold) coordinated in a square-planar pyramid (tetrahedral) geometry in bulk water. The integral of the first peak of the $g(r)$ for all cases except the chemisorption case reaches a plateau value of about 4 which corresponds to the number of nearest neighbour water molecules arranged in either the square planar or the tetrahedral geometry. It should be noted that the fifth apex water molecule of the pyramidal structure visible in three panels (blue, red and black) is not reflected in this plateau value demonstrating that it is only dynamically present, as discussed in section 4.2.2 and illustrated in Fig. 4.3. Also, this integral of $g(r)$ reaches 3 in the chemisorption case (orange dashed line), illustrating the partial desolvation of the hydroxide covalently bonded to the hBN layer. Moreover we observed that the diffusion mechanism for the physisorbed anion mediated by proton transfer is similar to that in bulk water[163] albeit restrained to occur only within the first interfacial water layer.

Once the anion is in the active 4-fold solvation configuration (receiving three H-bonds), frequent proton transfers occur through the standard tetrahedral water network, until OH^- finds itself once again in an inactive 5-fold environment (receiving four H-bonds).
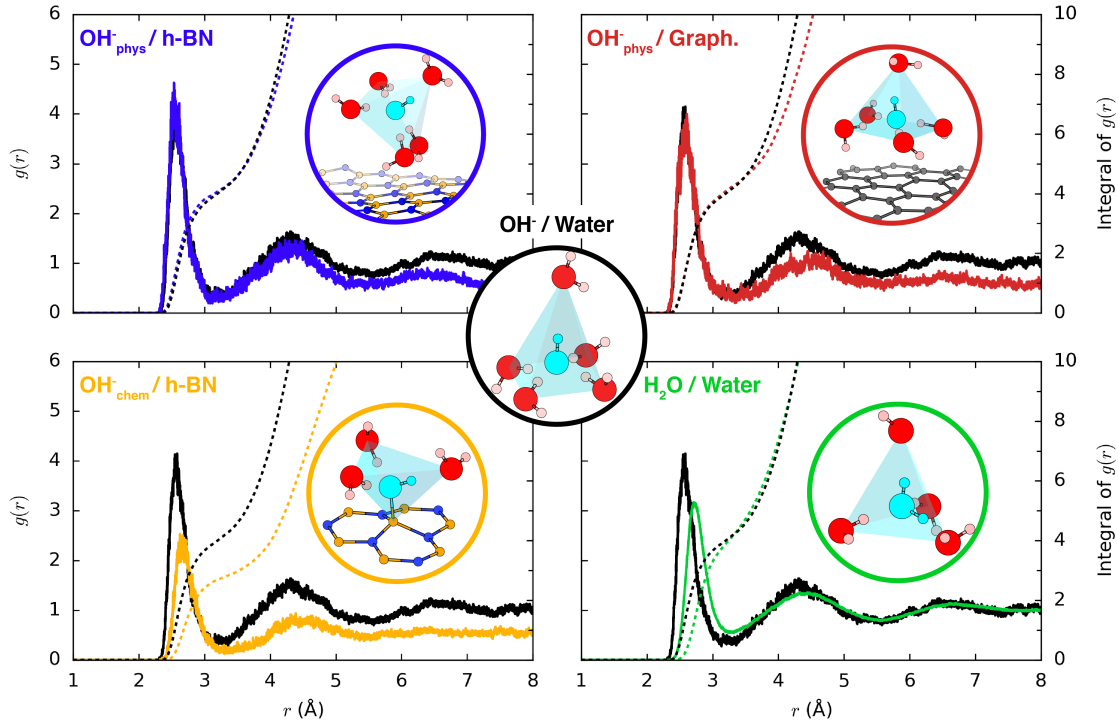
Figure 4.5: Radial distribution functions from unbiased trajectories. Radial distribution functions of oxygen atoms around the free hydroxide oxygen O* in different environments: bulk water (black), chemisorbed on hBN (orange), physisorbed on hBN (blue) and physisorbed on graphene (red). The $g(r)$ of a H_2O molecule in bulk water is shown in green. The integrals of the $g(r)$ are displayed as dotted line in the corresponding colour. Solvation geometries of the different configurations are shown within circles of the associated colour: square pyramid for the anion in bulk water (black) or physisorbed on hBN (blue) or on graphene (red), tetrahedron for a chemisorbed OH^- on hBN (orange) or for a bulk water molecule (green).

4.4 Comparison to Conductance Measurements in a Carbon Nanotube

These simulation results show that not only the graphene surface can be charged through physisorption of hydroxide but also that there is a concomitant appearance of a surface conductivity through hydroxide transport within the first water layer. To confirm this

picture, we compared our findings with the experimental conductance of single carbon nanotubes (CNT) measured by Secchi *et al.* [36]. These authors measured the conductance of single CNTs passing through a membrane separating two compartments containing a solution of KCl at concentration C_S and at a pH fixed by addition of KOH. In order to compare our results with experiments, it is necessary to take into account the electrostatic repulsion between adsorbed hydroxide ions and the presence of counter ions in the double layer of the surface for charge equalisation. These effects are missing in our simulation of a single hydroxide ion in absence of any counterion. Such effects however have been modelled successfully using mean-field approaches[172].

Here, for the sake of comparison, we employ the same charge equalisation model as in reference[36]. We start from the free energy of N adsorbed hydroxides on a graphene surface of area S at an electrostatic potential V_S:

$$F(N) = -k_B T \log \left(\frac{q^N}{N!} e^{-\frac{eV_S}{k_B T}} \right) \tag{4.1}$$

where $T = 300$ K and q is the partition function for one hydroxide. Since the calculated PMF corresponds to averaging over all other degrees of freedom except the O* translation, we may write

$$q = \frac{S}{\Lambda^3} \int_{r=0}^{r^*} e^{-\frac{U(r)}{k_B T}} \, dr, \tag{4.2}$$

where Λ is the De Broglie thermal wavelength, $U(r)$ the PMF, and r^* a cutoff distance separating adsorbed hydroxide from bulk hydroxide. In doing so, we have assumed that the PMF $U(r)$ does not depend on the lateral position of the hydroxide, x, y, while we have computed $U(r)$ for a given x, y, at an apical position over a carbon atom of the graphene layer. This assumption is validated by the fact that we observe no corrugation effect in the free trajectory for a physisorbed hydroxide and in fact for insight's sake a very mild corrugation below 10 meV was derived by AIMD for H$_2$O at the water/graphene interface by Tocci *et al.*[74]. For comparison with Secchi *et al.*[36] we further rewrite the one particle partition function as

$$q = \frac{Sd}{\Lambda^3} e^{-\frac{U_{\text{ads}}}{k_B T}}, \tag{4.3}$$

where U_{ads} is the bottom value of the PMF and the characteristic distance d is

$$d = \int_{r=0}^{r^*} e^{-\frac{(U(r) - U_{\text{ads}})}{k_B T}} \, dr. \tag{4.4}$$

We have computed d numerically taking $r^* = 5.9$ Å, the largest value of r for our calculated PMF, and found $d = 0.21$ Å. This value is nearly independent of r^* for $r^* > 4$ Å. It is then straightforward to obtain the chemical potential of adsorbed hydroxide ions as the derivative of $F(N)$ and using Stirling's approximation:

$$\mu_{\text{S}} = k_B T \log\left(\frac{\Sigma \Lambda^3}{d}\right) - eV_{\text{S}} + U_{\text{ads}}, \tag{4.5}$$

with $\Sigma = N/S$ the surface density of hydroxides. In the reservoirs far from the carbon nanotube (CNT) the chemical potential of the hydroxide is simply

$$\mu_{\text{B}} = k_B T \log\left(\frac{[\text{OH}^-]}{c^0} c^0 \mathcal{N}_a \Lambda^3\right), \tag{4.6}$$

where $[\text{OH}^-]$ is the hydroxide concentration in mol.L^{-1}, $\mathcal{N}_a$ is the Avogadro number and c^0 the standard concentration $c^0 = 1$ mol.L^{-1}, such that $[\text{OH}^-]c^0\mathcal{N}_a$ is the hydroxide number density. At equilibrium $\mu_{\text{S}} = \mu_{\text{B}}$ and we find

$$\Sigma = \frac{10^{\text{pH}}}{K_{\text{e}}} c^0 \mathcal{N}_a d e^{-\frac{U_{\text{ads}}}{k_B T}} e^{\frac{eV_{\text{S}}}{k_B T}}, \tag{4.7}$$

where $K_{\text{e}} = 10^{14}$ is the water dissociation constant. This equation is identical to the result of Secchi *et al.* with the quantities d and U_{ads} defined here from the calculated PMF. As V_{S} itself depends on the surface charge, this equation has to be solved self-consistently for Σ. We employ the same non-linear Poisson-Boltzmann charge equalization model as Secchi *et al.*[36], which leads to an experimentally observed power-law dependence of the surface charge on salt concentration at low ionic strength. Finally, to compute the conductance of the CNT, we have considered the experimental mobility for KCl $\lambda_{\text{KCl}} = \frac{1}{2}(\lambda_{\text{Cl}^-} + \lambda_{\text{K}^+}) =$
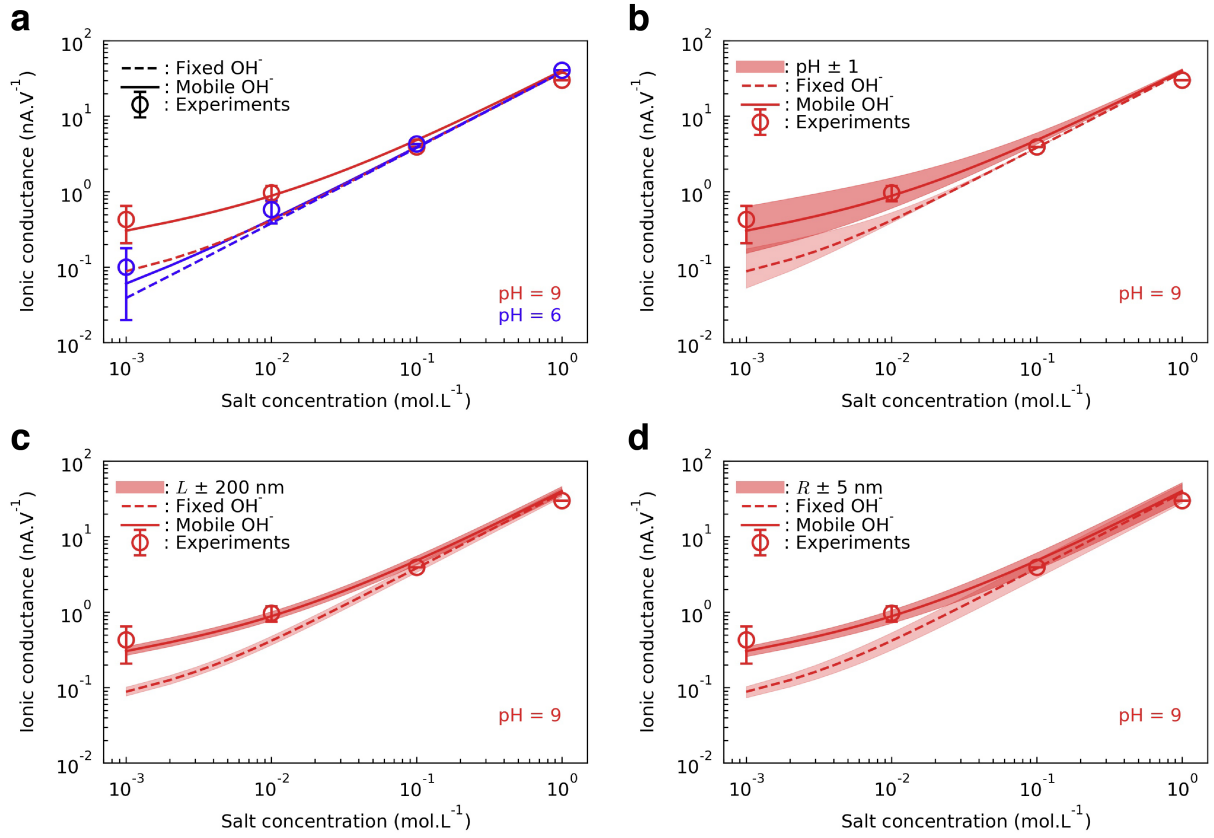
Figure 4.6: Ionic conductance, experiments versus analytic model. Ionic conductance G of a single 1500 nm long multiwall carbon nanotube with an inner diameter of 35 nm in function of the salt concentration at pH 6 (blue) and pH 9 (red). The circles correspond to experimental measurements $G = I/\Delta V$ (courtesy of Secchi *et al.*[36]). The dotted and plain curves are derived from analytic models respectively excluding and including the mobility of the hydroxide anion. a) Comparison of experimental points with the two models. The effect on both models applied to the conductance at pH 9 of a variation of 1 pH unit (b), 200 nm of tube length (c) and 5 nm of tube radius (d) is represented by coloured surfaces, with the upper (lower) bounds respectively corresponding to a pH increased (decreased) by 1 unit, a length decreased (increased) by 200 nm and a radius increased (decreased) by 5 nm.

4.8×10^{11} s.kg^{-1}. Similarly, we have considered the experimental bulk mobility of OH$^-$, inferred from its diffusion constant, $\lambda_{\text{OH}^-} = \frac{D_{\text{OH}^-}}{k_B T} = 13 \times 10^{11}$ s.kg^{-1}, since we found in our simulation a similar mobility for physisorbed hydroxide or for bulk hydroxide.

The conductance of the CNT is related to the surface concentration of hydroxide through the Poisson-Nernst-Planck equation adapted to confined geometry. However, the usual picture for the conductance assumes that the adsorbed charges are immobile. Here, we contradict this picture, showing that the physisorbed hydroxide retains a large surface mobility. We evaluate the contribution of the mobile surface charge by first noting that

the surface charge per unit length of a CNT of radius R is $2e\pi R\Sigma$, e being the elementary charge. The adsorbed ions have a mobility λ_{OH^-}, thus when submitted to an electric field V/L, where L is the CNT length and V the potential applied across the CNT, they acquire a velocity $v = \lambda_{OH^-} eV/L$. This leads to a contribution of the mobile surface charge to the conductance being equal to $G_{Surf} = 2e^2\lambda_{OH^-}\dfrac{\pi R}{L}\Sigma$. We thus correct the usual Poisson-Nernst-Planck result for the conductance, G, with the hydroxide mobility, such that we write

$$G = 2e^2\lambda_{KCl}\frac{\pi R^2}{L}\sqrt{C_S^2 + \frac{\Sigma^2}{R^2}} + 2e^2\lambda_{OH^-}\frac{\pi R}{L}\Sigma \tag{4.8}$$

where C_S is the salt (KCl) concentration. $\lambda_{KCl} = \frac{1}{2}(\lambda_{Cl^-} + \lambda_{K^+})$ is the KCl mobility. The first term thus accounts for the KCl contribution to the conductance, while the second term arises because of the mobile adsorbed charges. If we take $U_{ads} = -400$ meV, on the high side but within error bars of our predicted value, and $d = 0.21$ Å, as described above, we obtain results in quantitative agreement with experiments for the conductance of a CNT with $R = 35$ nm and $L = 1500$ nm, at pH $= 6$ and pH $= 9$, see Fig. 4.6a. The model reproduces well the pH dependence of the conductance at low salt concentration, coherent with hydroxide ions being adsorbed on the CNT surface. The fluctuations of analytic conductance derived by including or excluding the second term of equation 4.8 are displayed by coloured surfaces in Fig. 4.6b-d. Variations of 1 unit of pH (b), 200 nm of tube length (c) and of 5 nm of tube radius (d) are displayed. It appears that the geometry of the system has a negligible effect on its conductance contrary to an increase of pH which displays a notable influence.

4.5   Conclusion

In summary, we have shown by means of *ab initio* molecular dynamics that graphene and hBN single layers can both charge up in contact with alkaline water but in a different way. On a graphene surface the hydrated hydroxide anion is physisorbed albeit diffusing laterally via lateral proton hops. On hBN surface either the hydroxide anion covalently

binds to a boron surface atom or remains physisorbed and mobile. These findings originate from free energy profiles of one OH$^-$ near the surfaces and have been further confirmed by unbiased MD trajectories starting at the PMF adsorption wells. Analytic developments accounting for the unveiled surface mobility of the adsorbed charges are very consistent with ionic conductance measurements performed earlier in nanofluidic devices. It is noteworthy that experimental charges display a large magnitude even at neutral pH, with *e.g.* a surface charge of about 0.2 C.m^{-2} at pH 7 in the case of BNNT[35]. The presently evidenced reactivity is thus far from being an exceptional case under extreme conditions. This charging mechanism can possibly be further investigated experimentally at the molecular scale by means of sum-frequency generation spectroscopy as the OH$^-$ remains mainly in the vicinity of the graphene surface. Also, the confinement of the hydroxide at the interface, with proton transfer restrained to the first interfacial water layer raises the question of its validity in extremely confined channels such as the recently elaborated ångstrom slit-pores nanofluidic devices[160, 161, 173]. In fact, only up to two water layers can penetrate in between the graphite layers constituting those channels. As interfacial molecular information on such system is not accessible experimentally, this should be the object of future AIMD studies, in the same spirit of the recent hydroxide solvation modelling in inorganic mackinawite slit-pores[92]. Slit-pores channels made of non-metallic materials could also provide an appropriate substrate to probe the normal orientation of the hydroxide to the surfaces by the above-mentioned interfacial spectroscopy technique.

Apart from providing a satisfactorily explanation for the puzzling charging revealed by nanofluidic experiments using *ab initio* simulations, the present study unravelled an unexpected reactivity of BN and graphene allowing to envision peculiar chemistry at water interface with BN and carbon based sp^2 nanomaterials. Indeed, while constituting tools of choice for rationalising experiments requiring explanations at the molecular scale, first principles simulations also exhibit powerful predictive capabilities to which the following chapter is dedicated, building on the reactivity findings presented here.

Chapter 5

Water Dissociative Adsorption at hBN-Graphene Planar Heterojunctions

A large part of this work is undergoing submission process for publication starting in June 2019, with Anton Robert among co-authors[96]. Computational details and methodologies are thoroughly described in chapter 2, sections 2.2 and 2.5.

5.1   Motivation

Building up on the chemistry of hBN and graphene revealed in the studies presented in the preceding chapters we envisioned a special reactivity of an in-plane junction of the two materials towards the H_2O molecule. Knowing that OH^- strongly chemisorbs on top of a boron site of an hBN single-layer through an apparently charge-driven stabilisation of the adsorbed state due to the ionicity of the material, we expect this reactivity to be maintained as the firm insulating character of hBN is likely to keep the local charge and subsequent adsorption properties even while undergoing significant structure modification. On the contrary the metallic nature of graphene suggests that its reactivity can be dramatically tuned by doping, so that its capacity of chemisorbing H^+ would be activated by binding the carbon layer with a hBN one in a planar manner. Combining the two materials through a covalent junction would therefore be a way of taking advantage of the reactivity of BN while activating that of its carbon counterpart.

Experimental routes to produce such hybrid composites of BN and graphene (G) have been pioneered by Ci and coworkers[174] and recently summarised in a review[175]. Precisely several routes of synthesis have emerged either from bulk copolymerisation[176] or from growing catalytically on a variety of pure and alloy metal substrates, such as Cu[177–181], Ru[182–184], Rh[151], Ir[152, 185], Pt[186] or Cu-Ni alloy[187]. The latter fabrication of metal-supported monolayers are being obtained with high levels of control being reported on the nanometer scale thanks to the scanning tunnelling microscopy (STM) probe and sometimes real-time low energy electron microscopy (LEEM). In most of these studies, zigzag (ZZ) linking edges are preferentially formed with respect to the armchair (AC) interface. In particular on Rh, the ratio ZZ/AC amounts precisely to 3:1[151]. Moreover in the ZZ edge there is either a C-N interface or a C-B interface - defining donor and acceptor interface states respectively -, the latter being found more favourable[152].

Beyond synthesis and characterisation, there is much less progress on the reactivity of the composite border. Using zero Kelvin DFT framework the dissociative reactivity of a few gaseous molecules like dioxygen[176, 188] and water[34] have been performed on other kinds of hybridised materials issued from G and BN, in one case as a support to experimental reactivity[176]. But these molecules were always treated as single frozen species, far from their true environment in the liquid water. Indeed liquid water requires a full quantum treatment to properly include dynamical proton transfers between H-bonding water molecules[67]. To our knowledge, a realistic simulation of the interface between water solvent and hybrid in-plane BN-G heterostructures remains highly promising albeit challenging and is lacking to date which is the major goal of our study.

In the present study we undertook a screening of the possible border configurations when matching BN and G materials in a planar fashion. On all borders we first computed the dissociative adsorption of water in vacuum and corrected in a dielectric solvent. On the most favourable ones - the ones being exothermic and slightly endothermic, we ran *ab initio* molecular dynamics (AIMD) with an explicit interface with bulk water. On one border an interfacial H_2O molecule was found to spontaneously chemisorb onto one boron atom and to eventually dissociate by transferring a proton to the surrounding

water. These reactive events occur within the few ps of the simulation unveiling the facile reactivity of the hybrid composites.

5.2 H$_2$O Dissociative Co-Adsorption by Static DFT

When water dissociates on a two-dimensional substrate there are a number of possible adsorption scenarios and we focus here on one possible outcome: the adsorption of both OH and H components of water, with them both being on one side of the substrate, namely, *cis*(OH-H) using the same notation as previously[34]. Hence other possible products like *trans*(OH-H) and (OH + H$_{gas}$) are discarded in this static survey study but are not ruled out in the forthcoming *ab initio* molecular dynamics part detailed below. Adapting the protocol used in chapter 3 the dissociative adsorption energies of H$_2$O called E_{ads} on different edges bridging BN and G monolayers into co-adsorbed hydroxide and proton were computed first in vacuum and secondly in implicit water at $T = 0$ K. To do so, the value of E_{ads} is obtained by comparing the total energy of the adsorbed ions on the surface $E_{ads/surf}$ with that of the flat pristine surface $E_{pristine}$ added to that of the pristine water molecule E_{H_2O} *i.e.* $E_{ads} = E_{ads/surf} - (E_{pristine} + E_{H_2O})$. In fact contrarily to the case of an adsorbing OH$^-$ (see chapter 3) the study of the neutral H$_2$O allows for the separation of the adsorbate and the pristine surface into two distinct simulation cells to describe the adsorption reference state. The adsorption energy calculation scheme is illustrated in Fig. 2.12.

Pristine atomic layers of BN and G were also included for sake of references but yielded unfavourable dissociative adsorption energies above 2.5 eV (see Table 5.1) in good agree-

Material	Configuration	E_{ads}^{vac}	E_{ads}^{sol}
hBN	ortho	2.59	2.59
	para	3.34	3.01
Graphene	ortho	2.56	2.69
	para	2.92	3.00
	meta	3.46	3.57

Table 5.1: Dissociative adsorption energy of H$_2$O on 60 atoms hBN and graphene single layers in vacuum (E_{ads}^{vac}) and in implicit water (E_{ads}^{sol}). All energies are in eV. On hBN the OH$^-$ and H$^+$ fragments are respectively on top of a boron and a nitrogen atom.
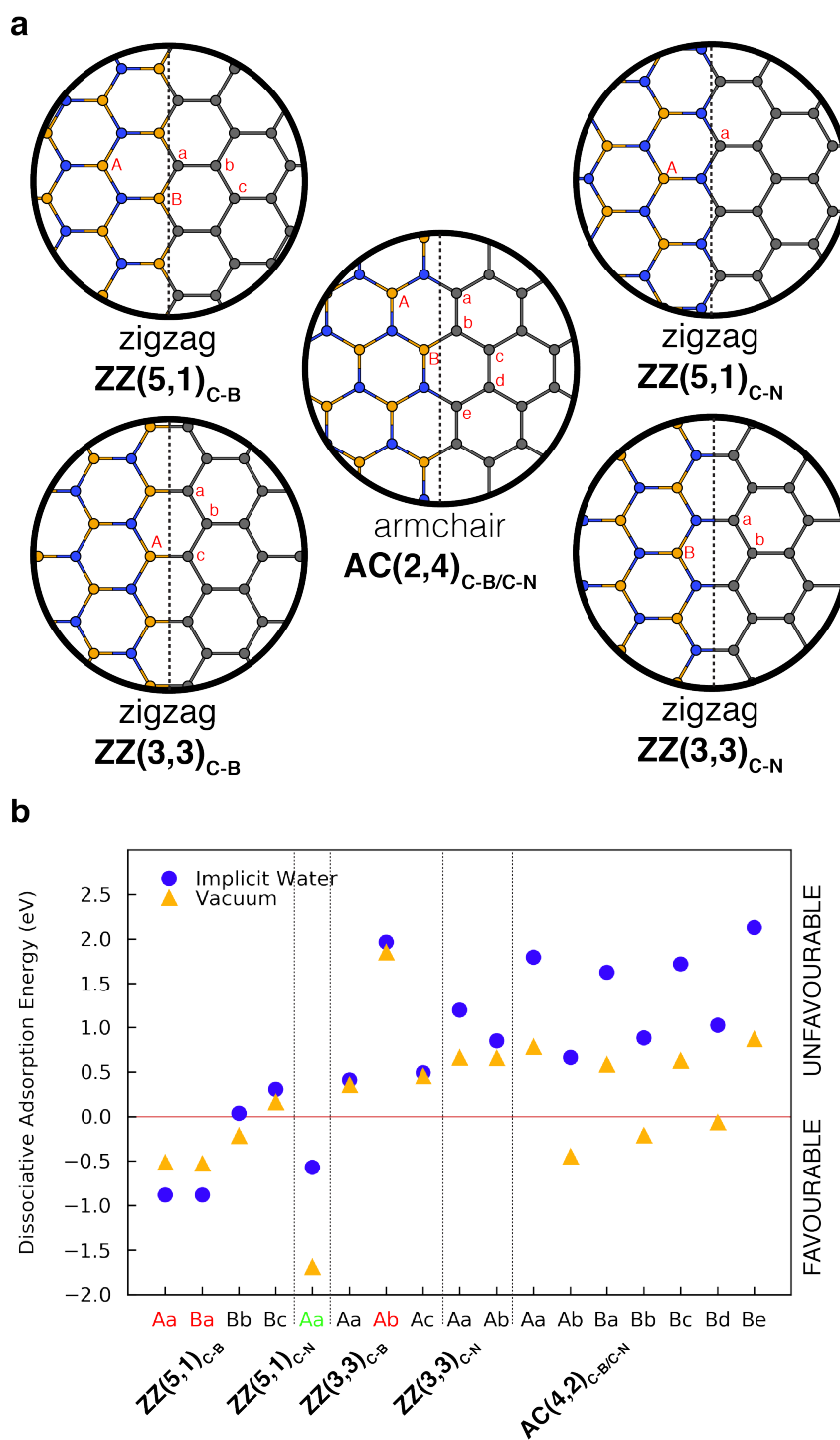
Figure 5.1: a) Junction geometries and associated adsorption configurations. The junction is schematically represented by a grey dotted line while the boron, carbon and nitrogen atoms are respectively displayed in orange, grey and blue. Red uppercase letters label hydroxide adsorption sites (boron atoms close to the junction) while red lowercase letters indicate associated proton adsorption sites (carbon atoms constituting a hexagon with a boron atom of the junction region). b) Dissociative adsorption energies of H_2O in vacuum (orange triangles) and implicit water (blue circles) for various adsorption configurations on 5 distinct junction geometries. Coloured labels indicate configuration which metastability was also tested in explicit water by *ab initio* molecular dynamics. Spontaneous dissociative adsorption of H_2O was observed on the green labelled geometry.

ment with previous results[34]. Nevertheless, hydroxides were previously shown to be prone to strong chemisorption on boron atoms from BN layer in contrast with the carbon atoms from G with which no covalent bond could be stabilised in water (see chapters 3 and 4)[94, 95]. Following the idea of combining the hBN reactivity towards OH^- and the activation of that of graphene towards H^+, we thus modelled a few BN-G planar heterojunctions as candidates for water dissociative adsorption, keeping in mind that boron atoms retain their ability to bind hydroxides while carbon atoms would bind the remaining proton. The five different junctions are displayed in Fig. 5.1a, and the corresponding simulation cells are displayed in Fig. 5.2. Note that each cell contains two border regions due to periodic boundary conditions. Here we considered three different cells containing four zigzag (ZZ) configurations and one armchair (AC). In the sharp interface the border hexagons are necessarily a composite BCN one: for ZZ (AC) border there is an odd (even) number of each material. As a result we have considered the borders $ZZ(3,3)_{C-B}$; $ZZ(5,1)_{C-B}$; $ZZ(3,3)_{C-N}$; $ZZ(5,1)_{C-N}$ and $AC(2,4)_{C-B/C-N}$. For instance, the border hexagons of the $ZZ(5,1)_{C-B}$ geometry correspond to a brute formula of $B_3N_2C_1$ and include C-B bonds. Note that we only consider one type of composite asymmetric junction ZZ(5,1) because the ZZ(1,5) corresponds to the row of hexagons next to the ZZ(5,1) therefore already included in the (5,1) simulation cells. Moreover for the asymmetric junction ZZ(5,1), the border region has an extended width of two hexagons while the border region is limited to one hexagon in any other border geometries (see Fig. 5.2). For each junction, several H_2O dissociative adsorption configurations are possible and we restrict them to the ones where i) the hydroxide is chemisorbed on a boron atom, ii) the proton is chemisorbed on a carbon atom, iii) the co-adsorption occurs within the same hexagon. In total, 17 adsorption configurations are compared on 5 junction geometries and their dissociative adsorption energies are displayed in Fig. 5.1b. As a general trend already observed in our previous study (see chapter 3)[94], the dissociative adsorption energies tend to be destabilised in implicit water versus in vacuum (see the orange triangles in the plot Fig. 5.1b are mostly lying in the energy scale below the blue circles). In some cases however the energy does not change too much when introducing
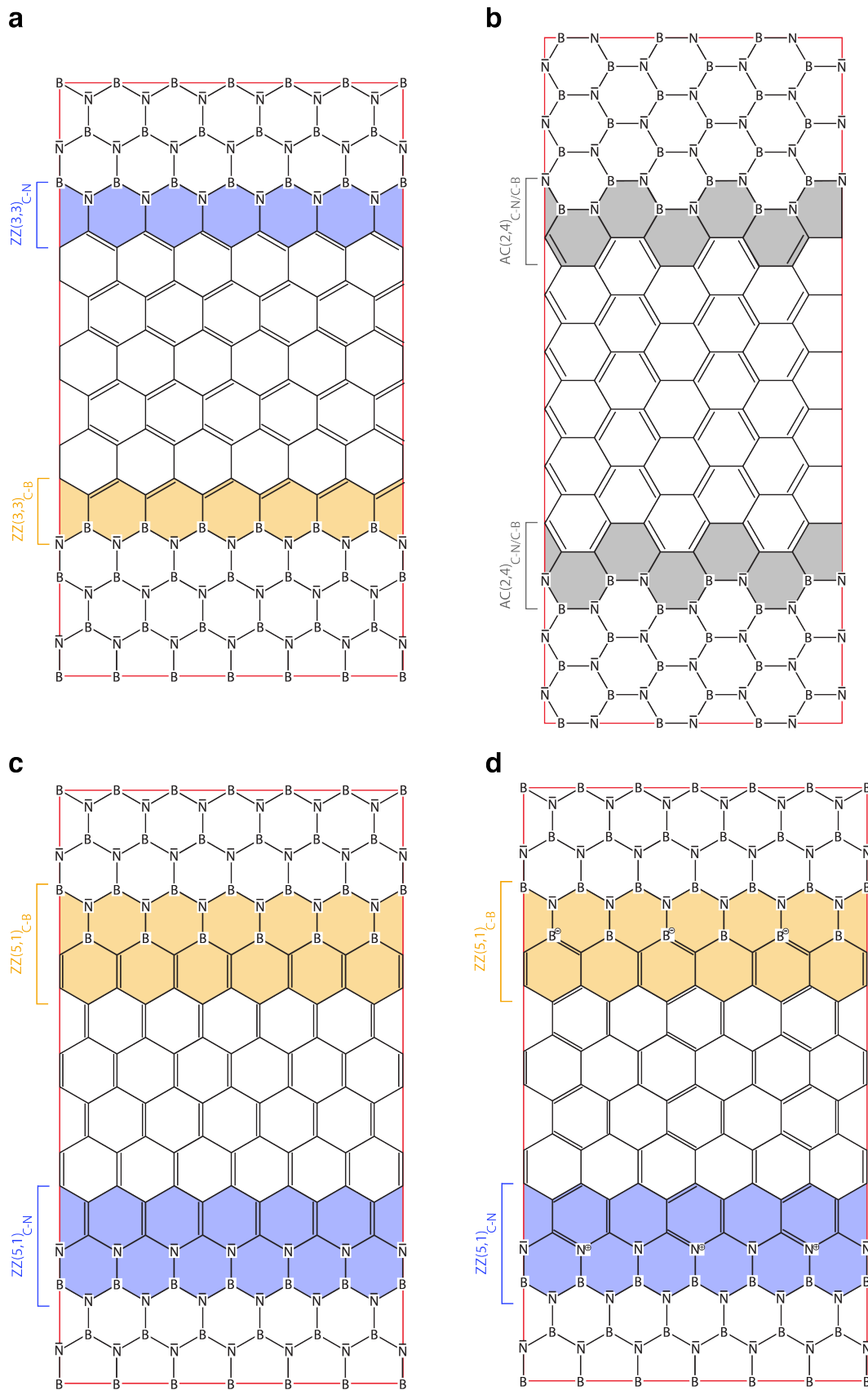
Figure 5.2: (Caption next page.)

Figure 5.2: (Previous page.) Neutral Lewis structure of the simulation cells containing the two types of ZZ(3, 3) edge (a), the AC(2,4) junction (b) and the two types of ZZ(5,1) edges (c). Zwitterionic Lewis structure of ZZ(5,1) edges (d) in agreement with analysis of the projected density of states and observation of the localisation of Wannier orbital centers and of the highest occupied molecular orbital. Dimensions of the cells are 14.77 Å × 25.58 Å for the ZZ edges and 12.78 Å × 29.55 Å for the AC edges. The C-N, C-B and C-N/C-B junctions are respectively highlighted in blue, orange and grey while the limit of the cell is represented in red.

a solvent correction. The reason of that non-constant energetic destabilisation originates from the cavity spherical model that accounts for the solvation cage. In the adsorbed system the surface of the cavity is obviously less than the sum of two cavities of the reference systems: the molecule and the bare substrate. The reference systems are thus more solvated and then more stabilised by the implicit water solvation model than the adsorbed system. Our energetic results show that the ZZ edge configurations (on the left side of the plot in Fig. 5.1b) are more reactive towards water dissociative adsorption than the AC egde configurations (right side). In addition the experimentally-observed ZZ edges - ZZ(33) - are globally less reactive than the asymmetric ZZ edges - ZZ(5,1) - tested here. Precisely, Fig. 5.1b exhibits three adsorbed configurations with negative (favourable) dissociative adsorption energies in the implicit water case: $ZZ(5,1)_{C-B}$ Aa (-0.88 eV) and $ZZ(5,1)_{C-B}$ Ba (-0.88 eV), and $ZZ(5,1)_{C-N}$ Aa (-0.57 eV). These results contrast with the positive energies obtained for the pure boron nitride and graphene layers, corroborating the prediction of the activation of those composite planar layers for water dissociative adsorption. Furthermore, the magnitude of the favourable adsorption energies indicate a strong interaction between the adsorbates and the surface, calling for more realistic dynamical quantum studies on the reactivity of H_2O at the liquid water/BN-G planar heterojunction interface, that we detail below.

5.3   Metastability of Co-Adsorbed Hydroxide and Proton by AIMD

Hydrogen bonds are of primordial importance for the water solvent. Therefore implicit solvation schemes can not fully satisfactorily describe the adsorption of H_2O fragments on BN and G atomic layers as illustrated by the preceding chapter. In fact, the water self-ions OH^- and H^+ are transient species in water because they are subject to fast reactions with H-bonded water molecules through proton transfers. Hydrogen bonds are essential to account for the fast mobility of these ions and therefore to their final stabilisation when adsorbed at an interface with liquid water. In order to properly simulate such systems and assess the metastability of adsorbates, one must resort to computationally expensive *ab initio* molecular dynamics (AIMD) simulations in which water molecules are comprehensively described.

We therefore computed 10 ps long unbiased AIMD trajectories of several adsorption configurations in contact with 195 water molecules equilibrated at 323 K (see chapter 2 section 2.5.3). An example of an AIMD simulation cell without adsorbates is displayed in Fig. 5.3. The dissociated configurations tested by AIMD correspond to coloured (red and green) labels in Fig. 5.1b: the 3 configurations identified as favourable in implicit
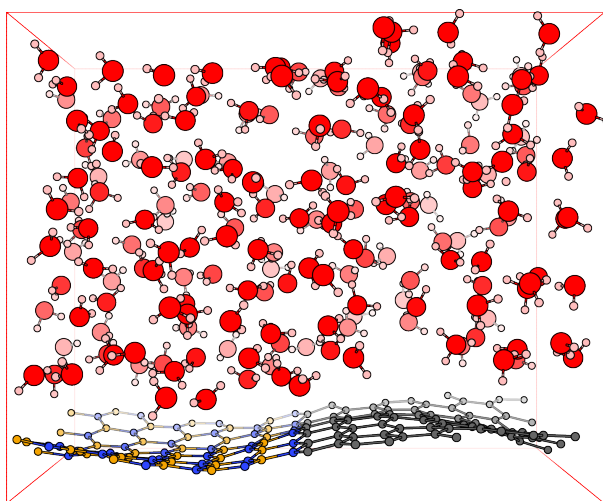
Figure 5.3: Example of simulation cell with explicit water. The $ZZ(5,1)_{C-N}$ junction geometry is represented along with 195 H_2O. Hydrogen, boron, carbon, nitrogen and oxygen atoms are respectively represented in pink, orange, grey, blue and red.

water by static DFT ($ZZ(5,1)_{C-B}$ Aa, Ba and $ZZ(5,1)_{C-B}$ Aa) and the configuration of the experimentally observed junction geometry identified as the most unfavourable case among the ZZ edges: $ZZ(3,3)_{C-N}$ Ab. In all 4 cases, the co-adsorbed fragments OH^- and H^+ were found metastable, as none of the ions was desorbing during the 10 ps of the dynamics. More interestingly the most unfavourable of the 4 configurations ($ZZ(3,3)_{C-N}$ Ab) was also found metastable, despite a static adsorption energy computed as high as +1.97 eV. Hence it is likely that all of the 17 configurations considered in the present work would be found metastable if tested similarly *i.e.* by free AIMD simulations. This points out that the theoretical results originating solely from static DFT results might convey a partial picture of the reactivity in water solvent. This stresses even further the necessity of an explicit and quantum description of solvents like water at the interface of 2D materials. Due to computational costs only 4 of the 17 configurations could be tested by AIMD, yet the metastability of them all is also supported by the very high chemical activity of the BN/G heterostructures as described in the next part.

5.4 Spontaneous Adsorption and Dissociation of H_2O

It is crucial to stress that the timescale and the number of chemical objects that one can simulate with AIMD do not allow for the observation of rare chemical events, so that one can only hope to witness extremely easy reactions along a bias-free trajectory. The observation of any spontaneous reaction is therefore a strong indication of the extremely high reactivity of those surfaces. To better study the water dissociative adsorption mechanism, a water interface with a pristine $ZZ(5,1)_{C-N}$ junction *i.e.* free of fragments, was thermalized at 323 K while preventing all water molecules to approach the surface below 2 Å. Upon release of the latter constraint, a water molecule starting at a large distance of 2.8 Å from the surface (see Fig. 5.4a, cyan line) *i.e.* within the interfacial solvent layer (see the inset of Fig. 5.4b, water density peak at 3.3 Å), was found to chemisorb on a boron atom of the junction after $t = 1.2$ ps of free MD (see Fig. 5.4c, inset 2). The water adsorbates then rapidly dissociates into an adsorbed hydroxide and an aqueous hydronium at $t = 1.3$ ps (see Fig. 5.4c, inset 3). Although the ions dynamically recombine at certain
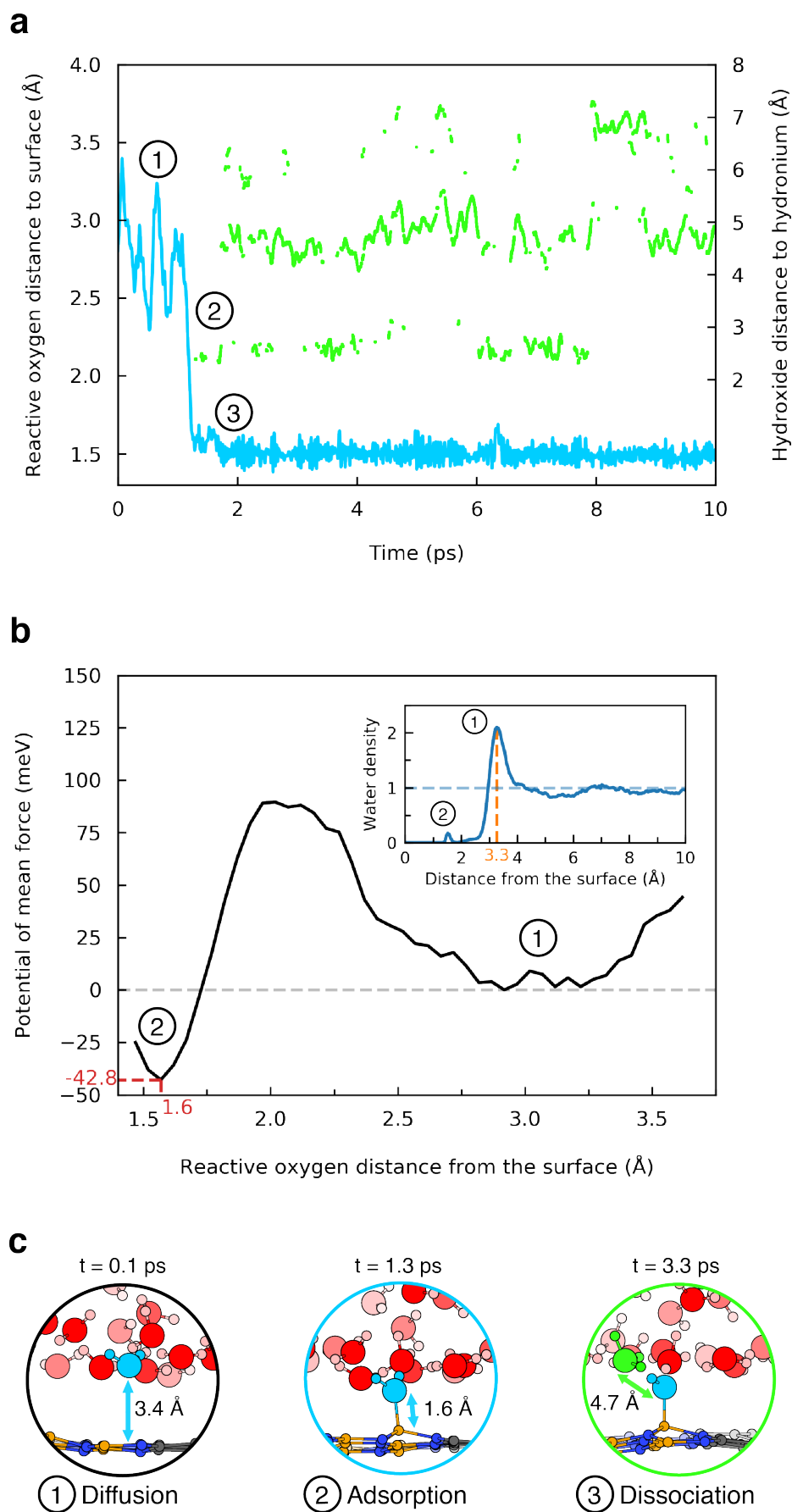
Figure 5.4: (Caption next page.)

Figure 5.4: (Previous page.) 10 ps long AIMD simulation of the ZZ(5,1)$_{C-N}$ junction in explicit water leading to the observation of the spontaneous adsorption of a H_2O molecule followed by its dissociation into an adsorbed hydroxide and an aqueous hydronium. a) The distance to the surface of the oxygen eventually adsorbing on a boron atom and the distance between the dissociated OH^- and H_3O^+ are respectively represented by a cyan line and green dots along the 10 ps trajectory. b) Potential of mean force of a H_2O with respect to its distance to the surface (black line), with the energy reference represented by a grey dotted horizontal line. The energy and position of the chemisorption well is indicated in red. Inset: The water density with respect to the distance of the surface with the horizontal and vertical lines respectively indicating the bulk density value and the position of the interfacial layer. The density corresponds to an average over the whole cell. c) Snapshots of the dynamics with associated times and distances. The reactive H_2O and OH^- are both represented in cyan. Circled numbers correspond to the ones in a) and b).

points of the 10 ps long trajectory, the as created hydronium cation diffuses further away from the first solvation shell of the fixed adsorbed OH^-. To identify the dissociation state from the atomic configurations, we associate each hydrogen atom to the closest oxygen to it. The atoms with respectively one and three associated hydrogen are then defined as corresponding to the hydroxide and the hydronium. During the simulation the adsorbate is in a OH^- state only 94% of the time and in a H_2O state 6% of the remaining time.

The distance from the surface of the oxygen that adsorbates and the distance between the two water self-ions are respectively displayed in cyan and green in Fig. 5.4a. The chaotic trajectory (green line) of the hydronium ion in water is simply the manifestation of its intrinsic reactivity in water: it will transfer one proton to a neighbouring water that will become the hydronium species. This results into large diffusion jumps of the hydronium cation and blinking effects when tracking it in the dynamical simulation.

We therefore identified a reaction in three steps, as illustrated in Fig. 5.4c: diffusion of H_2O near the junction, chemisorption onto a border boron atom and subsequent but immediate dissociation. The last step indeed occurs only once the adsorbed state reached, not during the approach of H_2O to the surface. Interestingly, studying *a posteriori* the magnetism of this active edge, the spin-constrained structures in water were found less stable by about 0.5 to 1 eV than non spin-polarised ones with or without adsorbates.

Starting from a different atomic configuration, another trajectory simulating the same reactive interface was computed for 21 ps. The chemisorption was once again observed -
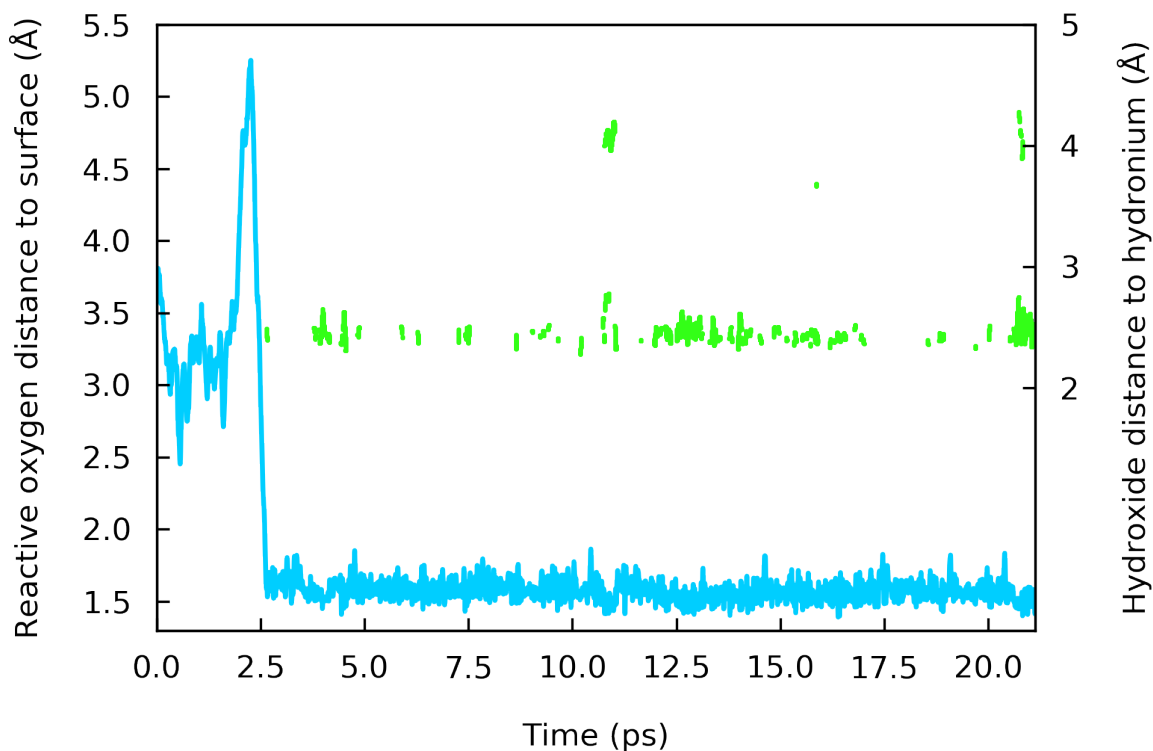
Figure 5.5: Non-dissociative spontaneous adsorption of water. Distance between the reactive oxygen atom and the surface (cyan) and between OH^- and H_3O^+ ions along a 20 ps long non-biased trajectory of the $ZZ(5,1)_{C-N}$/water interface. A water molecule spontaneously adsorbs on the surface but dissociates only dynamically.

at $t = 2.5$ ps -, corroborating the likeliness of this reaction (see Fig. 5.5). Yet, although one proton of the adsorbates appears to be shared with a solvating water molecule, no clear dissociation occurs, *i.e.* with diffusion of the excess proton further than the first solvation layer. With the method described above to identify the water self-ions from simulation, the adsorbate is in a OH^- state only 15% of the time and in a H_2O state 85% of the remaining time. Thus by comparing the two trajectories on the same junction it appears that the organisation of the solvation shell of the water adsorbate is playing a key role for its dissociation. We therefore hypothesise that the dissociation is likely to occur immediately after adsorption, before the solvent reorganises around the newly formed adsorbed state.

In the following, we aim at quantifying the reactivity of H_2O with the $ZZ(5,1)_{C-N}$ junction by determining the free energy of adsorption of a water molecule. This was derived from the potential of mean force (PMF) obtained by umbrella sampling while moving the

adsorbate away from the surface to the first interfacial layer of solvent by restraining the oxygen distance of the interacting water to the surface (see chapter 2, section 2.5.3). Because of the very high reactivity of the interface, preventing all other water molecules of the simulation cell from approaching the surface at less than 2 Å was proven necessary to avoid spontaneous adsorption. The resulting free energy profile shown in Fig. 5.4b displays a chemisorption well of -43 meV located 1.6 Å away from the surface and a barrier of 90 meV at 2 Å. The basin around 3 Å corresponds to the water density peak of the first water layer at 3.3 Å from the surface. The minimum of this basin was taken as reference energy for the PMF (see Fig. 5.4b, horizontal grey dotted line). Interestingly, the barrier height corresponds solely to about 4 $k_B T$, while a large number of potentially reacting molecules are present close to the junction as H_2O is the solvent, which furthermore displays a density peak in the vicinity of the surface. The density of water near the surface is relatively homogeneous on top of the whole simulation cell as displayed by detailed profiles in Fig. 5.6 and obtained from analysis of the 10 and 21 ps free trajectories leading to spontaneous reactions. The distribution of water near the surface is very similar to that on top of hBN and graphene pristine layers, as displayed in chapter 4 (see Fig. 4.2c). Taking into account periodic boundary conditions (PBC) of the simulation, the spontaneous dissociative adsorption of H_2O occurs at least once every 1.5 nm which corresponds to roughly 1/6 of the border boron sites being bonded to an oxygen atom. This estimate being based on the observation of the reaction in a limited time - 10 ps long AIMD trajectory-, we expect the actual occurrence to be much higher.

How realistic are our predicted reactive junctions towards liquid water? Experimentally the observed ZZ border is mostly the ZZ(3,3)$_{C-B}$ one[152, 179] and not the one that we found highly reactive *i.e.* ZZ(5,1)$_{C-N}$. Hence we tested a similar reactivity at the ZZ(3,3)$_{C-B}$ border[152, 179] by thermalizing, *i.e.* running MD at room temperature, a simulation cell consisting of one H_2O adsorbed on the border boron atom in plain water by restraining the adsorbed water molecule at 1.6 Å from the surface. Upon release of the latter restraint the water molecule was found to spontaneously desorb within a few hundreds of femtoseconds. Nevertheless, the adsorption configuration ZZ(3,3)$_{C-B}$ Ba was
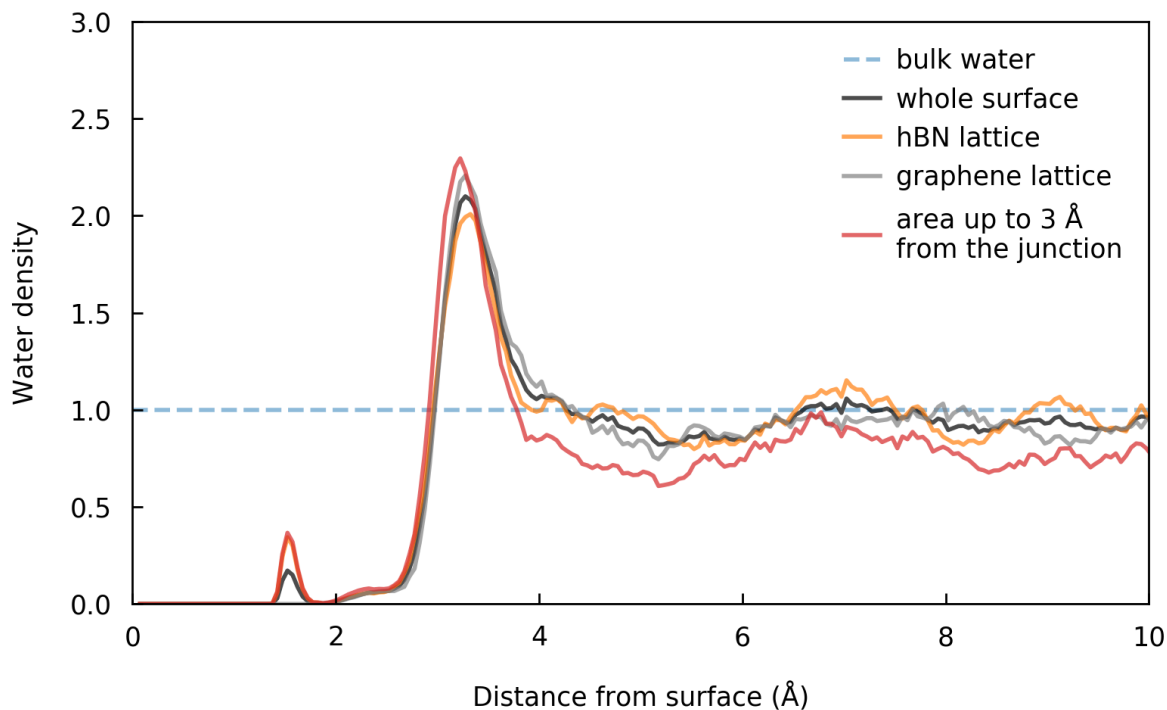
Figure 5.6: Water density profiles on top of the $ZZ(5,1)_{C-N}$ heterostructure averaged over two trajectories of 10 and 21 ps. The density over the whole surface, the hBN lattice, the graphene lattice and the junction are respectively represented in black, orange, grey and red. The junction region was arbitrarily defined as the area up to 3 Å away from the edge. The bulk density of liquid water is represented by a blue horizontal line as an indication.

also identified as metastable *i.e.* the OH and H co-fragments remain stable during free MD. Hence the co-adsorption of the dissociated fragments OH^- and H^+ can not occur after adsorption of H_2O at this junction. Instead, we postulate that the metastable adsorption state of the water fragment could be reached from ions already separated in solution or via concerted formation of the B-O bond and rupture of one O-H bond.

Finally the high reactivity found by our simulations on the $ZZ(5,1)_{C-N}$ edge can be understood from its versatile mesomeric forms, as displayed in Fig. 5.2. In fact, the position of the centers of the Wannier orbitals, the projected density of states and the observation of the electronic density of the HOMO point altogether towards a zwitterionic mesomeric form of the $ZZ(5,1)_{C-N}$ edge in water rather than the uncharged mesomeric form. Under this zwitterionic form, a net charge of $+1$ (-1) is carried by one of the edge nitrogen (boron) atoms of the $ZZ(5,1)_{C-N}$ ($ZZ(5,1)_{C-B}$) edge respectively. As a result the electrophily of the negatively charged $ZZ(5,1)_{C-B^-}$ edge is reduced while that of

the counterpart positively charged ZZ(5,1)$_{C-N^+}$ junction is greatly enhanced and further concentrated on boron atoms near it. Comparatively the positions of the centers of the Wannier orbitals of the ZZ(3,3) and AC(2,4) edges point towards neutral mesomeric form, stressing the peculiarity and chemical richness of the ZZ(5,1) borders.

5.5 Conclusion

Through the present *ab initio* simulations study, we have evidenced a covalent chemistry on BN-G planar heterostructures immersed in water, as compared to pristine materials. A large variety of border geometries were tested and the dissociative adsorption of H_2O to form B-OH$^-$ and C-H$^+$ fragments was found energetically favourable in a few cases. One junction geometry was identified as particularly reactive with spontaneous adsorption of H_2O and subsequent dissociation into an adsorbed hydroxide and an aqueous hydronium. This reactive junction corresponds to an asymmetric zigzag border hexagon and comprises one row of BN hexagons with one C atom substituting B and the next adjacent row of G hexagons with one N atom substituting C. Although supported qualitatively by AIMD simulations and quantitatively by derived adsorption free energy, the reaction occurs at a 1D junction geometry that has not been experimentally reported so far. However, such asymmetric composite hexagons echo substitutional doping in 2D materials and hence may be also observed in patchy BN islands embedded in a graphene sheet and vice versa[176, 189]. The use of state-of-the-art techniques such as atomic force microscopy in water is an exquisite tool of choice to seek experimental evidence for the water adsorption and dissociation at the hBN-graphene junction. This unique tool requires an ultimate reduction of the noise and has been developed recently[190, 191]. We also envision that the interfaces could be further activated in many diverse ways including heating the solution, applying some pressure or polarising the conductive carbon part of the substrate. We hope that our prediction will trigger more reactivity studies on the hBN-graphene planar heterostructures, as they appear disregarded when compared to their van der Waals counterparts (*i.e.* BN and G stacked into a combined graphitic arrangement), with only a dozen experimental studies since their structure discovery.

Chapter 6

Perspectives and Conclusion

This chapter presents three sub-projects that are still ongoing and likely to exhibit significant progress in the following months. Methodologies and computational details are described in chapter 2, section 2.6.

6.1 AIMD of the Nanotubes/Water Interfaces

The puzzling experimental phenomenon we aimed to rationalise through this study was observed also for nanotubes of large diameter (up to 40 nm)[35, 36] therefore justifying modelling the materials by planar surfaces. The effect of the curvature was probed within the static DFT framework (see chapter 3 section 3.4) in the extreme case of tubes of diameters of 1 nm, below the smallest experimental values. A strong effect was identified in particular for BN, with an enhancement of the chemisorption strength of OH^- of about 1 eV. However the question of the effect of the curvature in more realistic conditions and on the physisorption state still remains. We therefore wish to transfer our AIMD framework at 323.15 K with explicit solvation to the BNNT/water and CNT/water interfaces, with tube diameters of 2 nm, corresponding to the lowest experimental values. To model the rigidity of multi-wall nanotubes used experimentally, (15, 15) tubes of a diameter of 2 nm were simulated with fixing the surface atoms during the dynamics. Peculiar water structure was previously evidenced by classical MD studies on similar diameter tubes[192–195] which are typically filled by long simulations of their contact with water

97

reservoirs[81, 193, 196], an efficient construction method inapplicable to AIMD calculations since they require nanoseconds of simulation of large systems[81]. Interestingly a 2008 review article summarising molecular dynamics efforts over the water/nanotube interfaces reveals differing results obtained with almost identical simulation systems and conditions (tube dimensions, water density, pressure, temperature etc.) and points towards either an effect of different water models or water/surface interaction Lennard-Jones parameters[197]. This was is indeed well illustrated in the 2003 study by Werder *et al.*, who derived a significant variation (0 to 140°) of a water droplet contact angle on graphite when tuning the water-carbon interaction energy (over a 12.2 kJ.mol^{-1} range) or changing the empirical water model[198]. Despite the concerns raised by empirical and semi-empirical parametrisations on this type of systems, classical models have been widely preferred for obvious cost considerations with, to our knowledge, only a surprisingly small number of AIMD studies which furthermore focused solely on aqueous systems confined in extreme tube sizes (below ∼1 nm in diameter) in which only one to two water wires can penetrate[199–206]. Thus there appears to be no previous study at the quantum chemical level of pristine nanotubes large enough to host water in a reasonably liquid state.
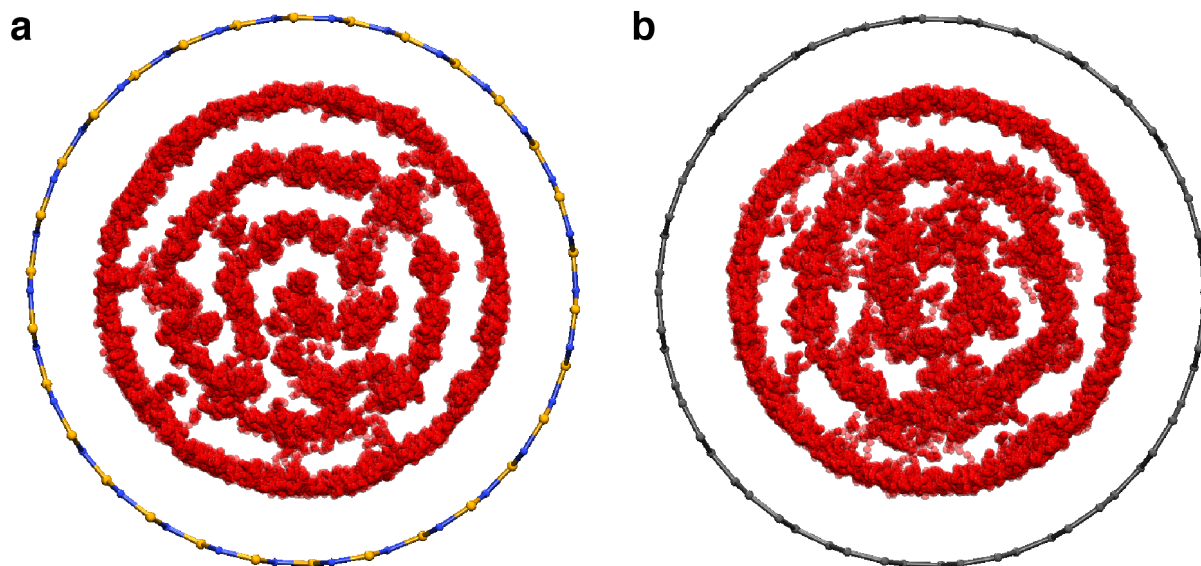
Figure 6.1: a) 6 ps trajectory of a boron nitride nanotube filled with 143 H$_2$O. b) 5 ps trajectory of a carbon nanotube containing 125 water molecules. Boron, carbon and nitrogen atoms are respectively represented in orange, grey and blue. The position of the oxygen atoms - represented by red transparent spheres - each 2.5 fs are superposed to display water structure. Hydrogen atoms are hidden for clarity.

The lack of experimental data and the variations of simulation information regarding water density and structure while confined in a tube of 2 nm diameter makes the process of constructing starting MD configurations particularly complex. Up to now our simulations of these interfaces have therefore been focused on the construction of the simulation cells. However our set-up protocol implies the computation of MD trajectories to derive pressure and structural quantities in order to check the relevance of the obtained structure. Several trajectories at different water densities (around 1) were therefore computed and showed promising observations in agreement with literature. Indeed a peculiar structuring of the liquid was also found, in contrast with observations on the water/single-layers interfaces. Considering Fig. 6.1 and the associated dynamics (not displayed), one can define three regions of the liquid: two well separated water layers close to the surface with few exchange of molecules between them and a more amorphous center. Liquid density profiles at the hBN/water and graphene/water interfaces were obtained by averaging on 20-50 ps long trajectories (*i.e.* a much larger statistic) and exhibited a clear interfacial peak (see Fig. 4.2c). However, no qualitative observations as clear as the ones made on the water/tube interfaces were possible, namely we did not observe well separated interfacial water layers. Considering the trapping of the physisorbed hydroxide described in chapter 4 it is very likely that the enhanced structuring of interfacial water in the tube would lead to an increased confinement of OH$^-$ and therefore larger surface charges. This hypothesis will be tested using a similar framework as the one reported in chapter 4, by deriving free energy profiles of OH$^-$ and bias-free trajectories of the anion pre-positioned in the different water regions.

6.2 AIMD of the Hydronium at the Interfaces

We have shown a peculiar confinement of OH$^-$ at the hBN/water and graphene/water interfaces with implication of the Grotthuss mechanism in the limited diffusion of the ion to bulk water. Although its solvation geometry and proton transfer rate significantly differs[67], the question of the existence of a similar confinement of a hydronium ion at these interfaces is most intriguing and was already observed in AIMD simulation of a
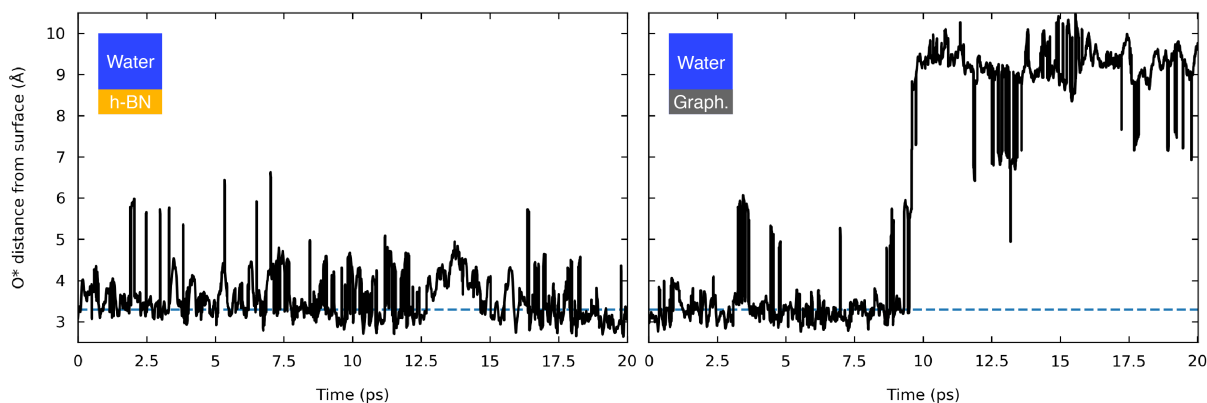
Figure 6.2: Distance of a hydronium oxygen from a hBN (left) and graphene (right) surface in water over the course of a 20 ps long trajectory. The position of the first interfacial water layer is displayed by a blue dotted horizontal line at the position of the maximum density, 3.3 Å.

fully hydrogenated graphene layer in contact with water[165]. Building on the experience with the OH^- species the physisorption of H_3O^+ was first probed via bias-free trajectories that echo the ones described in chapter 4 section 4.3: the cation was frozen at a fixed distance of 3.1 Å away from the surface and released during a 20 ps trajectory after thermalization. The cation was found to remain mostly within the first interfacial water layer close to hBN and although punctually exploring a bit further it stayed in the vicinity of the sheet for the whole 20 ps run (see Fig. 6.2 left). Although it behaved similarly at the graphene/water interface, the cation left the interface after about 10 ps before rapidly diffusing up to the middle of the simulation cell (10.5 Å) (see Fig. 6.2 right). Nonetheless the vicinity of H_3O^+ with graphene was not transient as it remained 10 ps, a time long enough for numerous proton transfers to occur, as illustrated by discontinuities in the back plot on the right of Fig. 6.2. These two bias-free trajectories therefore attest of an at least metastable physisorption state of the hydronium at the hBN/water and graphene/water interfaces.

To quantitatively estimate the affinity of the cation with the interfaces, potential of mean force were derived by performing an umbrella sampling of the ion-surface distance, with the advantage of keeping the freedom of the particle parallelly to the interface, as compared to blue moon sampling used to probe the same collective variable in chapter 4. Indeed in the latter case the ion is frozen and forced to solely explore the direction normal to
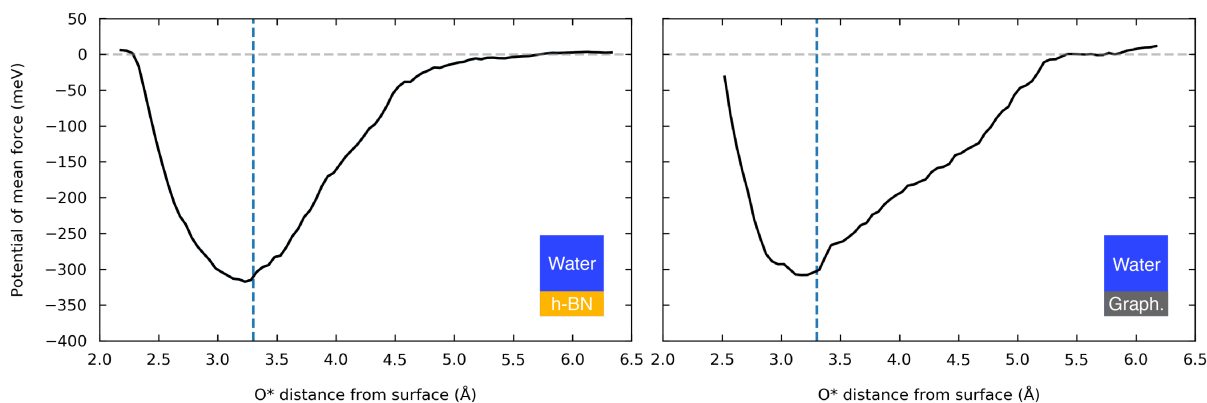
Figure 6.3: Potential of mean force of a hydronium with respect to the distance of its oxygen to a hBN (left) and graphene (right) surface in water. The free energy reference represented by a grey dotted horizontal line was taken as the average of the PMF over the last 1 Å. The position of the first interfacial water layer is displayed by a blue dotted vertical line at the position of the maximum density, 3.3 Å.

the surface. Here for the hydronium we restrained our exploration to the 2 - 6.2 Å region and did not probe chemisorption. This latter process is in fact less direct than it is with OH^- as protonation from water implies adsorption but also dissociation of H_3O^+. This greatly complexifies the derivation of the free energy of protonation in water by means of simulations, so much that an intricate and computationally extremely expensive (typically $\sim$ 200000-240000 DFT cycles) protocol is required to derive pK_a values[207] that are to our knowledge missing in the literature for pristine graphene and hBN. In contrast physisorption PMFs are easier to obtain in particular when compared to the case of OH^- which requires restriction of the ion's solvation shell (see chapter 4) while harmonic restraints on its three O-H bonds suffice to keep track of H_3O^+. The PMFs obtained to characterise possible physisorption states are displayed in Fig. 6.3.

Energy profiles of each interface seemingly present a physisorption well feature, centered at about 3.3 Å which corresponds to the position of the maximum of water density near the surfaces similarly to what was observed for the physisorption of OH^- at the same interfaces (see Fig. 4.2c). However the profiles are peculiar with in particular an approximately linear part between 3.3 Å and 4.5-5.5 Å i.e. until the flat part far from the surface. The existence of a possible electrostatic simulation artefact due to relying on a neutralising charged background was verified by studying the evolution of the electric potential normal to the surface with varying ion-surface distance. This showed no aberration that could be
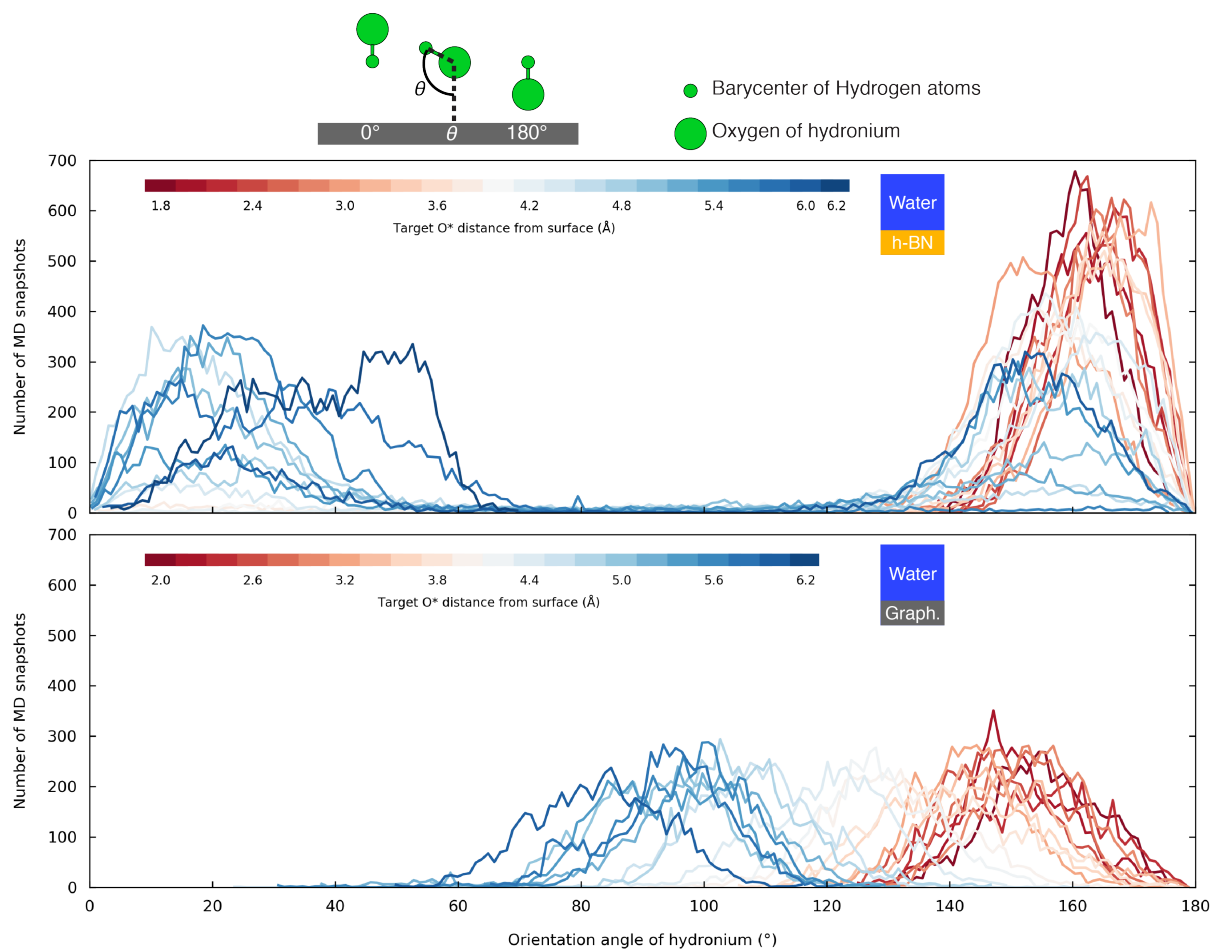
Figure 6.4: Distribution of the angle formed by the closest surface atom to the hydronium oxygen O*, O* and the barycenter of the three hydrogen atoms of the cation, on top of a hBN (top) and graphene (bottom) surface along biased trajectories. The colour of each plot corresponds to the value of the target of the restraint applied to the O*-surface distance. The bin size for the distributions is taken as one degree of angle.

responsible for the drift in the PMFs, in agreement with a similar verification conducted on the simulation of OH$^-$ at the interfaces, a case in which such a drift was not observed. Instead we envision an effect originating in the negligible sampling of the orientation of the cation. The distribution of the angle formed by the closest surface atom to the hydronium oxygen O*, O* itself and the barycenter of the three hydrogen atoms of the cation is displayed in Fig. 6.4 for each MD run used in the derivation of the PMFs.

In agreement with literature the cation displays a clear preferential orientation while in the vicinity of the surfaces and in particular between the material and the first water layer[165, 208–210]. Indeed the hydronium tends to point its oxygen towards the surface so that it can donate three hydrogen bonds to the water layer. The tendency seems

to reverse at larger distances in the case of hBN where a two-centered distribution still remains. Nonetheless the very progressive evolution of the hydronium ion's orientation with respect to its distance of the graphene layer indicates that it likely is a key collective variable that was possibly insufficiently probed during the acquisition of the PMFs. Indeed as mentioned above there exists strong link between the orientation of the water self-ion and its possibilities of forming stabilising hydrogen bonds. Based on this analysis of the distributions of orientation we can propose further interpretation of the PMFs displayed in Fig. 6.3. The first part up to $\sim$ 3.3 Å seemingly presents a correct shape since the hydronium spontaneously adopts its preferential orientation at the interface over short dynamic times as it is strongly driven by the presence of water in only one direction to form three stabilising hydrogen bonds. Far from the surface *i.e.* around the 6 Å distance modeling bulk water in the present case there should be no sharp preferences of orientation as the hydronium is entirely surrounded by water, leading to the expected flat end of the energy profiles. In-between however a transitory regime could be expected with some residual orientation preference insufficiently pronounced to be adopted over the course of the short biased MD trajectories used to perform umbrella sampling, hence an artefact on the free energy profiles. Future work will therefore include a two-dimensional umbrella sampling with which both the ion-surface distance and its orientation will be probed by jointly restraining them.

Although still ongoing the present simulation results on the interaction of H_3O^+ at hBN/water and graphene/water interfaces strongly point towards a physisorption of the cation in the vicinity of both surfaces surely in a complex competition with that of OH^- involving electrical double layer phenomena. The modeling of such effect requires to work with a number of chemical objects much larger than what is attainable with DFT. Ultimately one could perform a more comprehensive simulation of the hBN and graphene interfaces with water containing counter-ions in realistic proportions by relying on classical forcefields benefiting from the addition to their parametrisation of the free energy profiles derived here for OH^- and H_3O^+.

6.3   Reactivity of a hBN Point Defect in Water

Thanks to the experience gathered on the modeling of the water self-anion OH^- at the hBN/water interface, we were contacted by Jean Comtet and Aleskandra Radenovic to provide relevant AIMD data to the perplexing experimental results they obtained on hBN flakes in contact with water.

Briefly, upon laser illumination at 2.21 eV an emission centered at 2.12 eV of the hBN flake is measured when the material is in contact with water, but no emission is observed in air. The emission, previously observed on hBN[211–215], originate from point defects that can therefore be imaged as luminescent points. Surprisingly the optically active points were found to migrate at the 1-100 ms timescale pointing to an alternation of active/inactive states of the emitters with a chemical species migrating from defect to defect. A large variety of experiments including among others study in pH, isotopic effect, imaging of the migrating defects and variation of the number of emitters upon illumination time constituted a compelling body of evidence towards a reversible protonated luminescent form, so that following the migration of the defects is equivalent to imaging a proton moving through interfacial water from a non-emissive non-protonated defect to the next similar defect. The experimentalists thus envisioned a three-state model of the phenomenon where the optically active protonated form (ON state) is in acid/base equilibrium with the non-emissive deprotonated counterpart (OFF state). The third state corresponds to the excited protonated defect which can either relax by emitting at 2 eV or by releasing the proton and returning to the non-emissive state (see Fig. 6.5). The experimentalists indeed observed that the number of emitters on the hBN flake varies over the exposure time to the irradiation, namely decreasing to reach a steady-state with much less emitters while the initial number of emitters is completely recoverable after an appropriately long time in the dark *i.e.* without laser excitation, a behaviour consistent with the idea of an acid/base equilibrium of the defect chemical state shifted by the irradiation, as discussed below.

Our role has been to study the reactivity of the supposed luminescent defect with water and with hydronium ions by means of AIMD simulations. In a recent DFT study,

West *et al.*[216] simulated energy levels of point defects in bulk hBN. Using a hybrid functional called HSE aiming at reasonably describing excited states albeit heavy computational cost, the authors suggested that the protonated boron vacancies are most likely to form and named this complex V_{B}H as a plausible candidate for the 2 eV emission line. Although those bulk calculations were not performed on a single layer in contact with explicit water, the guess for the chemical identity of the emitter is consistent with the experimental evidences here at stake. As it was validated through the work reported in
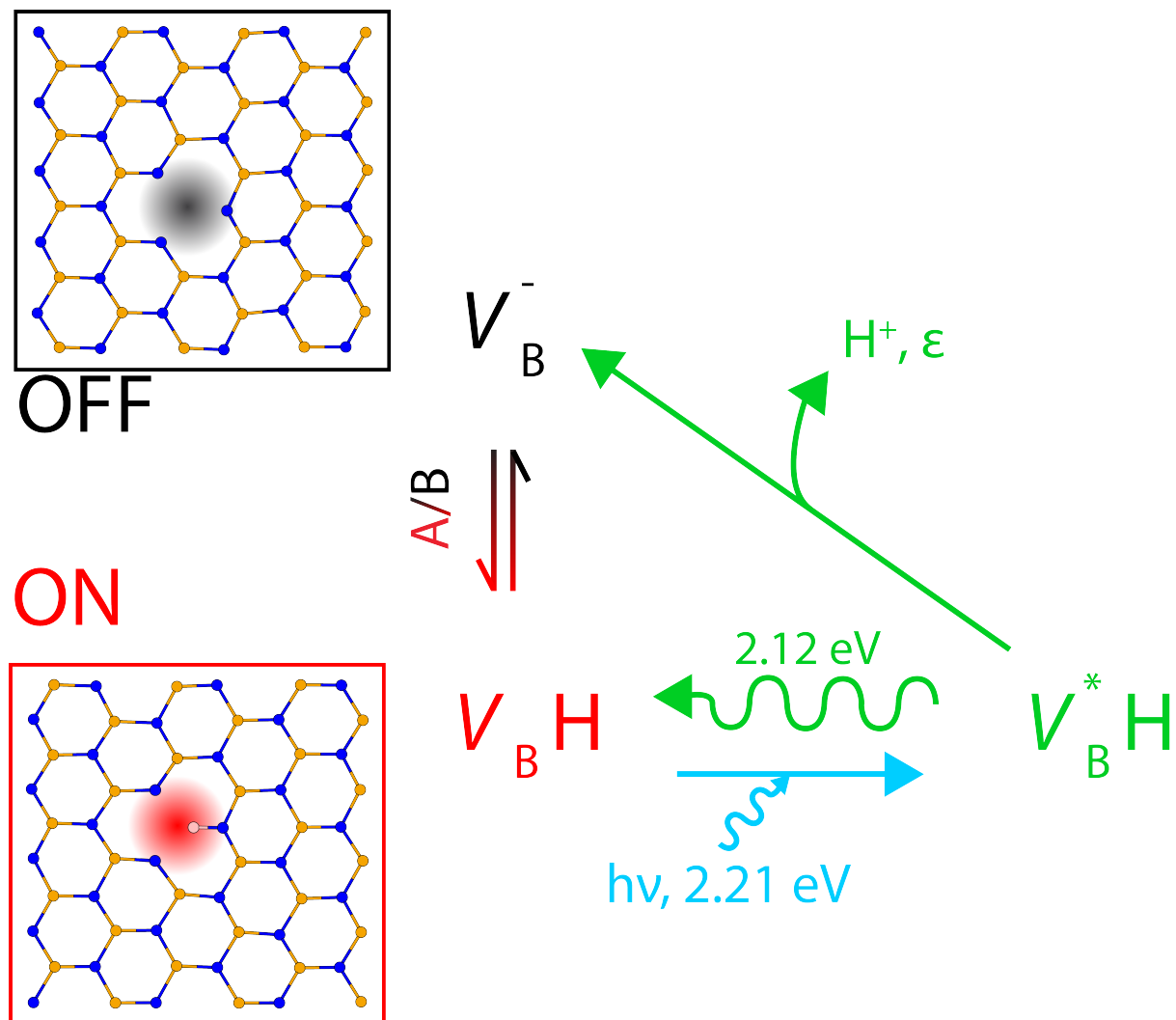
Figure 6.5: Three-states model for the emission: acid/base equilibrium between the emissive state (red) and the non-emissive state (black). Upon illumination by the laser (blue arrow), the acid form of the defect, envisioned as a boron vacancy reversibly protonated, reaches its excited state (green) which relaxes either by emitting at 2 eV or by deprotonation (green arrows), the latter process shifting the acid/base equilibrium. The surfaces used to model the OFF and ON states are represented on the left with the hydrogen, boron and nitrogen respectively displayed in pink, orange and blue.

the preceding chapters, we used the same AIMD framework as described in the present document to model the interface formed by a hBN sheet with a single boron vacancy and liquid water at room conditions. The simulation cell was simply obtained by removal of a boron atom from the atomic configurations generated in the work described in chapter 4. The aim is to assess the chemical stability of the two defect states ON/OFF of the luminescence mechanism (see Fig. 6.5) when taking into account the solvent environment at the quantum level. These defects are the negatively charged vacancy V_{B}^{-} (as expected from common knowledge on doping) and the complex in its ground state $V_{\mathrm{B}}\mathrm{H}$. As we employ the non-hybrid functional PBE, unable to simulate excited states, $V_{\mathrm{B}}^{*}\mathrm{H}$ cannot be correctly modeled. The reactivity of the defect with the surrounding aqueous medium was investigated with 2.5 to 5 ps long bias-free dynamics as it appeared sufficient to observe significant changes in the chemical system. The starting atomic configurations are obtained after a careful thermalizing process during which the hydrogen coordination of pending nitrogen atoms in the vicinity of V_{B} are restrained and their altitude constrained to remain in the hBN plane in order to inhibit hydrogen bonding with interfacial water molecules.

As a result V_{B}^{-} was found to be a base of significant strength as it would within 2.5 ps of time form a hydrogen bond with a donating water molecule that subsequently loses its shared proton to form the complex $V_{\mathrm{B}}\mathrm{H}$ and a solvated hydroxide ion O^{-} (see Fig. 6.6 a, b and c). This reactivity was also tested with a hydronium equilibrated at 3 Å away from V_{B} but one $\mathrm{H_2O}$ molecule reacted again to form $V_{\mathrm{B}}\mathrm{H}$ instead of $\mathrm{H_3O^+}$. It is noteworthy that as described in section 6.2 the water positive self-ion tends to point its oxygen atom towards the surface and form three stabilising hydrogen bonds with the water (see Fig. 6.6d), therefore necessitating first a significant reorientation before reaching a conformation prone to protonate the defect instead of a neighbouring water molecule. It is important to stress that because of the time scale and the number of objects that AIMD is able to simulate, only extremely likely reactions can be spontaneously observed over the course of a bias free trajectory. To bypass the initial energy cost of the reorientation of $\mathrm{H_3O^+}$, one can equilibrate the system while forcing the cation to point its oxygen away
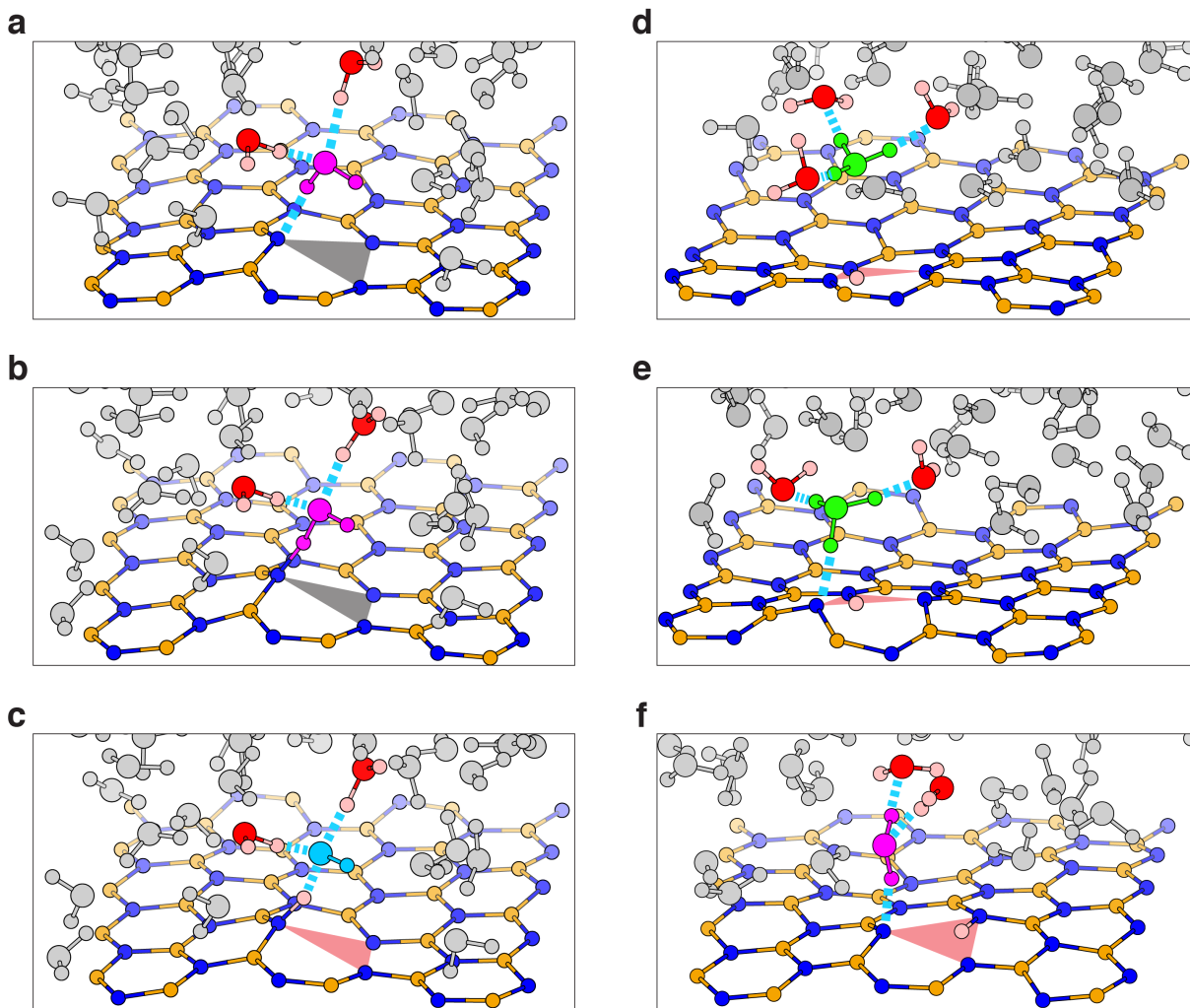
Figure 6.6: Simulation snapshots of a) H_2O hydrogen bonded to V_B^-, b) H_2O sharing a proton with V_B^-, c) OH^- hydrogen bonded to the H of VBH after proton transfer, d) H_3O^+ in its down orientation, e) H_3O^+ in its up orientation, hydrogen bonded to a pending N of VBH and f) H_2O hydrogen bonded to a pending N of V_BH. Hydrogen, boron, nitrogen and oxygen atoms are respectively represented in pink, orange, blue and red while the H_2O of interest, OH^- and H_3O^+ are respectively displayed in purple, cyan and green. For clarity the water molecules that are not forming hydrogen bonds with the species of interest are displayed in grey while the position of the emissive (non-emissive) surface defect is materialised by a red (black) transparent triangle whose apexes correspond to the three nitrogen atoms surrounding V_B^- or V_BH. Dotted cyan lines represent hydrogen bonds which correspond here to distances comprised between 1.4 and 1.8 Å. In b) the shared proton is equidistant to the N and the O, with a distance of 1.24 Å.

from the surface. We respectively denote this latter orientation up (reactive) and the former one down (non reactive) orientations (see Fig. 6.6 d and e). The reactivity of V_BH was tested in similar conditions, *i.e.* with and without H_3O^+ in its up orientation. In both cases no protonation was observed over the 5 ps of dynamics while a water

molecule was found to form a strong hydrogen bond with a pending nitrogen (see Fig. 6.6 f). The return to the V_{B}^- defect state through deprotonation was neither observed, in agreement with the form $V_{\mathrm{B}}H$ to be more stable and presumably the light emitter. Finally we suggest that the promoted electron in the excited complex V_{B}^*H would occupy the N-H antibonding molecular orbital σ^* and hence weaken this bond, in full consistency with experimental behaviours over changes of pH. In fact populating the N-H σ^* orbital upon illumination would shift the $V_{\mathrm{B}}H/V_{\mathrm{B}}^-$ acid/base equilibrium towards formation of V_{B}^-, in agreement with a bleaching of the light emitters over exposure time to the laser excitation as observed experimentally. Indeed as the simulated reactivity of V_{B}^- towards water indicates, the pK_a of the $V_{\mathrm{B}}H/V_{\mathrm{B}}^-$ couple should be very high so that $V_{\mathrm{B}}H$ would always predominate in water unless an intense light stimulus may shift the equilibrium.

In an attempt to simulate excited states of the differently protonated boron vacancy, we also performed bias-free dynamics of the interface with additional negative charges to model the excited vacancy, assuming a charge separation with an electron promoted into a state in the gap hence its localisation on V_{B} and the counterpart hole mobile in the valence band. Following the emission levels identified by West *et al.*[216] we modelled the interface of water with V_{B}^0, V_{B}^-, V_{B}^{-2}, V_{B}^0H, V_{B}^-H, $V_{\mathrm{B}}^{-2}H$ and $V_{\mathrm{B}}^0H_2$. Although such modelling of excited states being spurious and not representative of the experimental system, several spontaneous protonation were observed over a 2.5-5 trajectories, further supporting the high reactivity of this hBN point defect with the water medium. For each protonation and charge states, we observed strong hydrogen bonds formed between donating H_2O and pending nitrogen atoms of the hBN surface. The overall chemical exploration of the state of the boron vacancy in contact with water is illustrated in Fig. 6.7.

Motivated by a specific experimental phenomenon we therefore modelled an example of a point defect of hBN, V_{B}, and found it particularly reactive with water with spontaneous protonation events occurring within only a few picoseconds stressing even further the non-trivial chemistry of the hBN/water interface. This combined experimental and AIMD study is under review and published in arXiv[97].
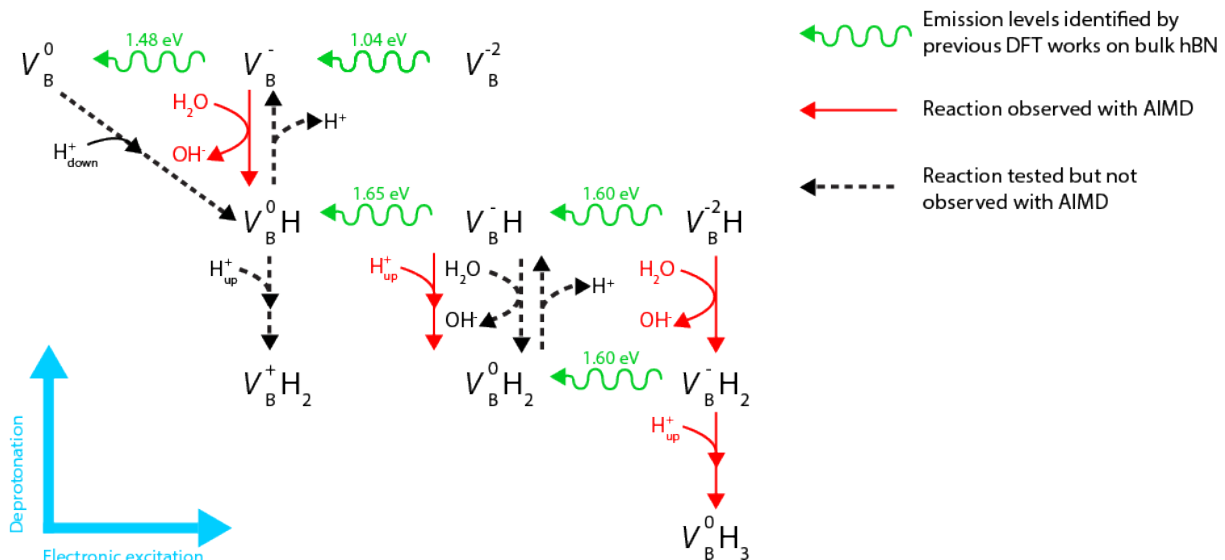
Figure 6.7: Map representing the chemical exploration performed with AIMD simulations. Spontaneous reactions are noted in red while the ones that were tested but not observed are in black with dotted lines for the arrows. The emission levels represented in green correspond to the predictions of West *et al.*[216] made on bulk hBN modelled by DFT with the HSE functional. The boron vacancy is progressively protonated from top to bottom and electronically excited from left to right.

6.4 Conclusion

This work was initially motivated by the experimental evidence of a tremendous surface charge of carbon and boron nitride based nanomaterials in room aqueous conditions, as revealed by ionic conductance measurements within state-of-the-art nanofluidic devices[35, 36, 160, 161, 173]. The surface charge - being found negative and dramatically growing with increasing pH - was presumed to emerged from adsorption of hydroxides at the water/sp^2 surface interface, with no facile experimental confirmation possible as only indirect measurements are currently conceivable at the molecular scale of such systems typically consisting in a single nanotube embedded in a mineral membrane surrounded by aqueous reservoirs closed by centimetre-thick polymer walls. Considering typical tube length and radius, *e.g.* 1000 and 10 nm, the total interfacial area on which one could average say spectroscopic data is indeed in the order of 0.1-0.01 μm^2.

Our study focused on the use of the remaining tool of choice on the quest of a proof of the charging mechanism, molecular simulations and in particular first-principles ones, able to satisfactorily model an interfacial system and its chemical reactivity without substantial

prerequisite parametrisation. Using static DFT alongside an implicit solvation scheme we validated the hypothesis of the charging mechanism of the BN surfaces via chemisorption of hydroxides but revealed a contrasting behaviour of the carbon counterparts with which no bond was formed by the anion (see chapter 3)[94]. Conducting heavier calculations replacing the implicit description of the solvent by the modeling of explicit water molecules in an *ab initio* molecular dynamics framework, we not only confirmed the static DFT results but also evidenced the physisorption of OH^- on each of the twin materials providing a concluding answer to the puzzling surface charging mechanism (see chapter 4). Beyond the equilibrium distribution of hydroxides at the interface we revealed a peculiar kinetic confinement of the anion linked to its solvation geometry and leaving it capable of fast diffusion in the vicinity of the surface, allowing for a correction of the analytic model for the ionic conductance of single nanotubes by including the contribution of the mobility of the surface charges, yielding excellent agreement with experimental results[95]. This study provided arguments for the benefits of comprehensive explicit description of the solvent at the quantum chemistry level when modeling interfacial systems at the molecular scale, as the shortcomings of static methods with implicit solvation schemes greatly limited the findings and understandings of the phenomena at stake.

Currently transferring the protocols used on the AIMD simulation of OH^- at the BN/water and graphene/water interfaces our results in progress point towards co-physisorption of hydronium and strong effect of the surfaces' curvature on confinement of hydroxides via increased interfacial water structuring. The possible competition between the self-ions of water calls for simulations at a wider scale, including a full description of the electric double-layers[86], typically by resorting to classical methods parametrised on quantum chemical quantitative data.

Beyond rationalisation of previous experiments, the still recently unexpected chemistry of the hBN and graphene with water has lead us to predictive simulations on activation of the atomic layers when chemically bound into a planar heterostructure. Exacerbated reactivity with H_2O was indeed revealed by simulations, predicting dissociative co-adsorption of the OH^- and H^+ fragments at the junction. The envisioned activity of the frontier was

serendipitously further stressed by observation of spontaneous water dissociative adsorption into chemisorbed OH^- and aqueous hydronium in less than 3 ps.

The reactivity of H_2O as well as the affinity of OH^- and H_3O^+ with BN and carbon based nanomaterials, alongside observations of spontaneous protonation events during few picoseconds long simulations of defected hBN form a compelling and conclusive body of evidence that these materials are in fact far from being "chemically inert" with in particular a rich chemistry when in contact of water in very mild conditions in which the usually negligible intrinsic co-existence of self-ions leads to enormous surface charges. The reactivity evidenced by ionic conductance measurements and AIMD simulations could be ultimately confirmed at the molecular scale by either interfacial spectroscopy of OH^- in slit-pore devices[92] and by state-of-the-art atomic force microscopy techniques allowing for imaging of single H_2O molecules in liquid medium at aqueous interfaces[190, 191].

Also, the highly reactive character predicted for hBN/graphene heterostructures combined with their intrinsically versatile structure calls for further experimental efforts on the catalytic possibilities of these widely disregarded materials. In fact one could take advantage of the reactivity at the junction by conjointly polarising the metallic carbon while keeping the local activity of the ionic counterpart.

Far beyond the inherent fundamental interest of studying the nature of the surface charging phenomena described here, understanding the molecular mechanisms at stake is an unavoidable step to identify the materials adequate for industrial applications in blue energy production and water desalination[61, 62, 102] in the following years, as a proper industry of the nanoscale has yet to grow functional before the construction of a power plant based on the insertion of nanotubes into membranes could be considered. In case of success these applications are promised to a high social impact as several large regions bordering for instance the sea of Cortez or the Mediterranean one with access to unlimited amount of salt water but regularly facing severe droughts could greatly benefit from advances in desalination processes in which the peculiar interaction of water with boron nitride and carbon based nanomaterials has a very promising role to play.

Bibliography

[1] Kroto, H. W., Heath, J. R., OBrien, S. C., Curl, R. F. & Smalley, R. E. C_{60}: Buckminsterfullerene. *Nature* **318**, 162–163 (1985).

[2] Novoselov, K. S. *et al.* Electric field effect in atomically thin carbon films. *Science* **306**, 666–669 (2004).

[3] Iijima, S. Helical microtubules of graphitic carbon. *Nature* **354**, 56–58 (1991).

[4] Chopra, N. G. *et al.* Boron nitride nanotubes. *Science* **269**, 966–967 (1995).

[5] Wang, Y., Li, Z., Wang, J., Li, J. & Lin, Y. Graphene and graphene oxide: biofunctionalization and applications in biotechnology. *Trends Biotechnol.* **29**, 205–212 (2011).

[6] Wolf, E. L. Applications of graphene: An overview. *Springer Briefs in Materials* (2014).

[7] Jiang, X.-F. *et al.* Recent progress on fabrications and applications of boron nitride nanomaterials: A review. *J. Mater. Sci. Tech.* **31**, 589–598 (2015).

[8] Zhang, J. Chemically derived graphene: Functionalization, properties and applications. *RSC Publishing* (2018).

[9] Chen, Y. Nanotubes and nanosheets: Functionalization and applications of boron nitride and other nanomaterials. *CRC Press* (2015).

[10] Choi, W. & won Lee, J. Graphene: Synthesis and applications. *CRC Press* (2016).

[11] Liu, Z. *et al.* Ultrathin high-temperature oxidation-resistant coatings of hexagonal boron nitride. *Nat. Comm.* **4**, 2541 (2013).

[12] Eftekhari, A. & Garcia, H. The necessity of structural irregularities for the chemical applications of graphene. *Mater. Today Chem.* **4**, 1–16 (2017).

[13] Taniguchi, T. & Watanabe, K. Synthesis of high-purity boron nitride single crystals under high pressure by using Ba–BN solvent. *J. Cryst. Growth* **303**, 525–529 (2007).

[14] Blake, P. *et al.* Graphene-based liquid crystal device. *Nano Lett.* **8**, 1704–1708 (2008).

[15] Golberg, D. *et al.* Boron nitride nanotubes and nanosheets. *ACS Nano* **4**, 2979–2993 (2010).

[16] Choi, W., Lahiri, I., Seelaboyina, R. & Kang, Y. S. Synthesis of graphene and its applications: A review. *Crit. Rev. Solid State Mater. Sci.* **35**, 52–71 (2010).

[17] Chou, T.-W., Gao, L., Thostenson, E. T., Zhang, Z. & Byun, J.-H. An assessment of the science and technology of carbon nanotube-based fibers and composites. *Adv. Mater. Interfaces* **70**, 1–19 (2010).

[18] Zheng, J., Ren, Z., Guo, P., Fang, L. & Fan, J. Diffusion of Li ion on graphene: A DFT study. *Appl. Surf. Sci.* **258**, 1651–1655 (2011).

[19] Liem, H. & Choy, H. Superior thermal conductivity of polymer nanocomposites by using graphene and boron nitride as fillers. *Solid State Commun.* **163**, 41–45 (2013).

[20] Liao, L., Peng, H. & Liu, Z. Chemistry makes graphene beyond graphene. *J. Am. Chem. Soc.* **136**, 12194–12200 (2014).

[21] Kroes, J. M. H., Fasolino, A. & Katsnelson, M. I. Density functional based simulations of proton permeation of graphene and hexagonal boron nitride. *Phys. Chem. Chem. Phys.* **19**, 5813–5817 (2017).

[22] Akbari, A. *et al.* Large-area graphene-based nanofiltration membranes by shear alignment of discotic nematic liquid crystals of graphene oxide. *Nat. Comm.* **7** (2016).

[23] Chen, Y., Gao, Z., Zhang, B., Zhao, S. & Qin, Y. Graphene coated with controllable n-doped carbon layer by molecular layer deposition as electrode materials for supercapacitors. *J. Power Sources* **315**, 254–260 (2016).

[24] Fazio, G., Ferrighi, L., Perilli, D. & Valentin, C. D. Computational electrochemistry of doped graphene as electrocatalytic material in fuel cells. *Int. J. Quantum Chem.* **116**, 1623–1640 (2016).

[25] Cruz, S., Girão, A., Gonçalves, G. & Marques, P. Graphene: The missing piece for cancer diagnosis? *Adv. Mater. Interfaces* **16**, 137 (2016).

[26] Arunachalam, V. & Vasudevan, S. Understanding aqueous dispersibility of boron nitride nanosheets from ^{1}H solid state NMR and reactive molecular dynamics. *J. Phys. Chem. C* **122**, 4662–4669 (2018).

[27] Sahu, J. *et al.* Enhanced tribo-chemical properties of oxygen functionalized mechanically exfoliated hexagonal boron nitride nanolubricant additives. *Mater. Chem. Phys.* **207**, 412–422 (2018).

[28] Zhang, L. *et al.* Charge-tunable water transport through boron nitride nanotubes. *J. Mol. Liq.* **258**, 98–105 (2018).

[29] Georgakilas, V. Functionalization of graphene. *Wiley-VCH* (2014).

[30] Araujo, P. T., Franklin, A., Kim, Y. A. & Krueger, M. Carbon nanotubes - synthesis, properties, functionalization, and applications. *Materials Research Society Proceedings* (2015).

[31] Thakur, V. K. & Thakur, M. K. Chemical functionalization of carbon nanomaterials: Chemistry and applications. *CRC Press* (2015).

[32] Cividanes, L. & Thim, G. Functionalizing graphene and carbon nanotubes: A review. *Springer Briefs in Applied Sciences and Technology* (2016).

[33] Jawaid, M., Bouhfid, R. & el Kacem Qaiss, A. Functionalized graphene nanocomposites and their derivatives: Synthesis, processing and applications. *Elsevier, Micro and Nano Technologies* (2018).

[34] Al-Hamdani, Y. S., Alfè, D., von Lilienfeld, O. A. & Michaelides, A. Tuning dissociation using isoelectronically doped graphene and hexagonal boron nitride: Water and other small molecules. *J. Chem. Phys.* **144**, 154706 (2016).

[35] Siria, A. *et al.* Giant osmotic energy conversion measured in a single transmembrane boron nitride nanotube. *Nature* **494**, 455–458 (2013).

[36] Secchi, E., Niguès, A., Jubin, L., Siria, A. & Bocquet, L. Scaling behavior for ionic transport and its fluctuations in individual carbon nanotubes. *Phys. Rev. Lett.* **116**, 154501 (2016).

[37] Behrens, S. H. & Grier, D. G. The charge of glass and silica surfaces. *J. Chem. Phys.* **115**, 6716–6721 (2001).

[38] Lagaly, G., Dékány, I. & Bergaya, F. Handbook of clay science, chapter 8: Colloid clay science. *Elsevier, Developments in Clay Science* (2013).

[39] Sun, Q. *et al.* Charge-controlled switchable CO_2 capture on boron nitride nanomaterials. *J. Am. Chem. Soc.* **135**, 8246–8253 (2013).

[40] Shin, H. *et al.* Covalent functionalization of boron nitride nanotubes via reduction chemistry. *ACS Nano* **9**, 12573–12582 (2015).

[41] Fu, L. *et al.* An ultrathin high-performance heat spreader fabricated with hydroxylated boron nitride nanosheets. *2D Mater.* **4**, 025047 (2017).

[42] Zhi, C. *et al.* Chemically activated boron nitride nanotubes. *Chem. Asian J.* **4**, 1536–1540 (2009).

[43] Sainsbury, T. *et al.* Oxygen radical functionalization of boron nitride nanosheets. *J. Am. Chem. Soc.* **134**, 18758–18771 (2012).

[44] Tang, C. *et al.* Fluorination and electrical conductivity of BN nanotubes. *J. Am. Chem. Soc.* **127**, 6552–6553 (2005).

[45] Cui, Z., Oyer, A. J., Glover, A. J., Schniepp, H. C. & Adamson, D. H. Large scale thermal exfoliation and functionalization of boron nitride. *Small* **10**, 2352–2355 (2014).

[46] Shi, L. *et al.* Edge hydroxylated boron nitride for oxidative dehydrogenation of propane to propylene. *ChemCatChem* 1788–1793 (2017).

[47] Weng, Q. *et al.* Highly water-soluble, porous, and biocompatible boron nitrides for anticancer drug delivery. *ACS Nano* **8**, 6123–6130 (2014).

[48] Jing, L. *et al.* Biocompatible hydroxylated boron nitride nanosheets/poly(vinyl alcohol) interpenetrating hydrogels with enhanced mechanical and thermal responses. *ACS Nano* **11**, 3742–3751 (2017).

[49] Wu, L. *et al.* Largely enhanced energy storage density of poly(vinylidene fluoride) nanocomposites based on surface hydroxylation of boron nitride nanosheets. *J. Mater. Chem. A* **6**, 7573–7584 (2018).

[50] Lin, Y. *et al.* Aqueous dispersions of few-layered and monolayered hexagonal boron nitride nanosheets from sonication-assisted hydrolysis: Critical role of water. *J. Phys. Chem. C* **115**, 2679–2685 (2011).

[51] Lee, D. *et al.* Scalable exfoliation process for highly soluble boron nitride nanoplatelets by hydroxide-assisted ball milling. *Nano Lett.* **15**, 1238–1244 (2015).

[52] Qiu, S. *et al.* Self-assembled supermolecular aggregate supported on boron nitride nanoplatelets for flame retardant and friction application. *Chem. Eng. J.* **349**, 223–234 (2018).

[53] Wu, K. *et al.* Preparation of a thermally conductive biodegradable cellulose nanofiber/hydroxylated boron nitride nanosheet film: the critical role of edge-hydroxylation. *J. Mater. Chem. A* (2018).

[54] Pakdel, A., Bando, Y. & Golberg, D. Plasma-assisted interface engineering of boron nitride nanostructure films. *ACS Nano* **8**, 10631–10639 (2014).

[55] Weng, Q., Wang, X., Wang, X., Bando, Y. & Golberg, D. Functionalized hexagonal boron nitride nanomaterials: Emerging properties and applications. *Chem. Soc. Rev.* **45**, 3989–4012 (2016).

[56] Zheng, Z., Cox, M. & Li, B. Surface modification of hexagonal boron nitride nanomaterials: A review. *J. Mater. Sci.* **53**, 66–99 (2017).

[57] Zhao, G. *et al.* One-step exfoliation and hydroxylation of boron nitride nanosheets with enhanced optical limiting performance. *Adv. Opt. Mater.* **4**, 141–146 (2015).

[58] Bocquet, L., Biance, A.-L., Poncharal, P. & Siria, A. Method and device for producing energy. *US Patent Number* **9564652** (2017).

[59] Mottet, B., Bocquet, L., Siria, A. & Bechelany, M. Device for producing energy by salinity gradient through titanium oxide nanofluid membranes. *US Patent Publication Number* **20180353906** (filed in 2016, published in 2018).

[60] Jia, Z., Wang, B., Song, S. & Fan, Y. Blue energy: Current technologies for sustainable power generation from water salinity gradient. *Renew. Sust. Energ. Rev.* **31**, 91–100 (2014).

[61] Striolo, A., Michaelides, A. & Joly, L. The carbon-water interface: Modeling challenges and opportunities for the water-energy nexus. *Annu. Rev. Chem. Biomol. Eng.* **7**, 533–556 (2016).

[62] Siria, A., Bocquet, M.-L. & Bocquet, L. New avenues for the large-scale harvesting of blue energy. *Nat. Rev. Chem.* **1**, 0091 (2017).

[63] Tuckerman, M., Laasonen, K., Sprik, M. & Parrinello, M. Ab initio molecular dynamics simulation of the solvation and transport of H_3O^+ and OH^- ions in water. *J. Phys. Chem.* **99**, 5749–5752 (1995).

[64] Tuckerman, M. E. On the quantum nature of the shared proton in hydrogen bonds. *Science* **275**, 817–820 (1997).

[65] Tuckerman, M. E., Chandra, A. & Marx, D. Structure and dynamics of $OH^-_{(aq)}$. *Acc. Chem. Res.* **39**, 151–158 (2006).

[66] Marx, D., Chandra, A. & Tuckerman, M. E. Aqueous basic solutions: Hydroxide solvation, structural diffusion, and comparison to the hydrated proton. *Chem. Rev.* **110**, 2174–2216 (2010).

[67] Chen, M. *et al.* Hydroxide diffuses slower than hydronium in water because its solvated structure inhibits correlated proton transfer. *Nat. Chem.* **10**, 413–419 (2018).

[68] Halle, B. & Karlström, G. Prototropic charge migration in water. part 2.—interpretation of nuclear magnetic resonance and conductivity data in terms of model mechanisms. *J. Chem. Soc., Faraday Trans. 2* **79**, 1047–1073 (1983).

[69] Sluyters, J. H. & Sluyters-Rehbach, M. The mechanism of the hydrogen ion conduction in liquid light and heavy water derived from the temperature dependence of their limiting conductivities. *J. Phys. Chem. B* **114**, 15582–15589 (2010).

[70] Agmon, N. The Grotthuss mechanism. *Chem. Phys. Lett.* **244**, 456–462 (1995).

[71] Vuilleumier, R. & Borgis, D. An extended empirical valence bond model for describing proton transfer in $H^+(H_2O)_n$ clusters and liquid water. *Chem. Phys. Lett.* **284**, 71–77 (1998).

[72] Vuilleumier, R. & Borgis, D. Transport and spectroscopy of the hydrated proton: A molecular dynamics study. *J. Chem. Phys.* **111**, 4251–4266 (1999).

[73] Day, T. J. F., Schmitt, U. W. & Voth, G. A. The mechanism of hydrated proton transport in water. *J. Am. Chem. Soc.* **122**, 12027–12028 (2000).

[74] Tocci, G., Joly, L. & Michaelides, A. Friction of water on graphene and hexagonal boron nitride from ab initio methods: Very different slippage despite very similar interface structures. *Nano Lett.* **14**, 6872–6877 (2014).

[75] Ohto, T., Tada, H. & Nagata, Y. Structure and dynamics of water at water–graphene and water–hexagonal boron-nitride sheet interfaces revealed by ab initio sum-frequency generation spectroscopy. *Phys. Chem. Chem. Phys.* **20**, 12979–12985 (2018).

[76] Joseph, S. & Aluru, N. R. Why are carbon nanotubes fast transporters of water? *Nano Lett.* **8**, 452–458 (2008).

[77] Suk, M. E. & Aluru, N. R. Water transport through ultrathin graphene. *J. Phys. Chem. Lett.* **1**, 1590–1594 (2010).

[78] Falk, K., Sedlmeier, F., Joly, L., Netz, R. R. & Bocquet, L. Molecular origin of fast water transport in carbon nanotube membranes: Superlubricity versus curvature dependent friction. *Nano Lett.* **10**, 4067–4073 (2010).

[79] Bonthuis, D. J. *et al.* Theory and simulations of water flow through carbon nanotubes: prospects and pitfalls. *J. Phys.: Condens. Matter* **23**, 184110 (2011).

[80] Cohen-Tanugi, D. & Grossman, J. C. Nanoporous graphene as a reverse osmosis membrane: Recent insights from theory and simulation. *Desalination* **366**, 59–70 (2015).

[81] Fu, L., Merabia, S. & Joly, L. Understanding fast and robust thermo-osmotic flows through carbon nanotube membranes: Thermodynamics meets hydrodynamics. *J. Phys. Chem. Lett.* **9**, 2086–2092 (2018).

[82] Simoncelli, M. *et al.* Blue energy and desalination with nanoporous carbon electrodes: Capacitance from molecular simulations to continuous models. *Phys. Rev. X* **8** (2018).

[83] Ganfoud, N. *et al.* Effect of the carbon microporous structure on the capacitance of aqueous supercapacitors. *Energy Storage Mater.* (2019).

[84] Cole, D. J., Ang, P. K. & Loh, K. P. Ion adsorption at the graphene/electrolyte interface. *J. Phys. Chem. Lett.* **2**, 1799–1803 (2011).

[85] Al-Hamdani, Y. S., Michaelides, A. & von Lilienfeld, O. A. Exploring dissociative water adsorption on isoelectronically BN doped graphene using alchemical derivatives. *J. Chem. Phys.* **147**, 164113 (2017).

[86] Merlet, C. *et al.* The electric double layer has a life of its own. *J. Phys. Chem. C* **118**, 18291–18298 (2014).

[87] Futamura, R. *et al.* Partial breaking of the coulombic ordering of ionic liquids confined in carbon nanopores. *Nat. Mater.* **16**, 1225–1232 (2017).

[88] Griffin, J. M. *et al.* In situ NMR and electrochemical quartz crystal microbalance techniques reveal the structure of the electrical double layer in supercapacitors. *Nat. Mater.* **14**, 812–819 (2015).

[89] Péan, C. *et al.* On the dynamics of charging in nanoporous carbon-based supercapacitors. *ACS Nano* **8**, 1576–1583 (2014).

[90] Péan, C. *et al.* Single electrode capacitances of porous carbons in neat ionic liquid electrolyte at 100 °C: A combined experimental and modeling approach. *J. Electrochem. Soc.* **162**, A5091–A5095 (2015).

[91] Péan, C. *et al.* Confinement, desolvation, and electrosorption effects on the diffusion of ions in nanoporous carbon electrodes. *J. Am. Chem. Soc.* **137**, 12627–12632 (2015).

[92] Muñoz-Santiburcio, D. & Marx, D. On the complex structural diffusion of proton holes in nanoconfined alkaline solutions within slit pores. *Nat. Comm.* **7**, 12625 (2016).

[93] Kayal, A. & Chandra, A. Orientational order and dynamics of interfacial water near a hexagonal boron-nitride sheet: An ab initio molecular dynamics study. *J. Chem. Phys.* **147**, 164704 (2017).

[94] Grosjean, B. *et al.* Chemisorption of hydroxide on 2D materials from dft calculations: Graphene versus hexagonal boron nitride. *J. Phys. Chem. Lett.* **7**, 4695–4700 (2016).

[95] Grosjean, B., Bocquet, M.-L. & Vuilleumier, R. Versatile electrification of two-dimensional nanomaterials in water. *Nat. Comm.* **10** (2019).

[96] Grosjean, B., Robert, A., Vuilleumier, R. & Bocquet, M.-L. *Submitted* (2019).

[97] Comtet, J. *et al.* Direct observation of water mediated single proton transport between hBN surface defects. **arXiv:1906.09019** (2019).

[98] Guillot, B. A reappraisal of what we have learnt during three decades of computer simulations on water. *J. Mol. Liq.* **101**, 219–260 (2002).

[99] Björneholm, O. *et al.* Water at interfaces. *Chem. Rev.* **116**, 7698–7726 (2016).

[100] Cohen-Tanugi, D. & Grossman, J. C. Water desalination across nanoporous graphene. *Nano Lett.* **12**, 3602–3608 (2012).

[101] Cohen-Tanugi, D., Dave, S. H., McGovern, R. K., Lienhard, V. J. H. & Grossman, J. C. Novel nanomaterials for water desalination technology. In *2013 1st IEEE Conference on Technologies for Sustainability (SusTech)* (IEEE, 2013).

[102] Cohen-Tanugi, D. & Grossman, J. C. Water permeability of nanoporous graphene at realistic pressures for reverse osmosis desalination. *J. Chem. Phys.* **141**, 074704 (2014).

[103] Graziano, G., Klimeš, J., Fernandez-Alonso, F. & Michaelides, A. Improved description of soft layered materials with van der Waals density functional theory. *J. Phys.: Condens. Matter* **24**, 424216 (2012).

[104] Stradi, D., Jelver, L., Smidstrup, S. & Stokbro, K. Method for determining optimal supercell representation of interfaces. *J. Phys.: Condens. Matter* **29**, 185901 (2017).

[105] Charlier, J.-C., Blase, X. & Roche, S. Electronic and transport properties of nanotubes. *Adv. Mater. Interfaces* **79**, 677–732 (2007).

[106] Kresse, G. & Hafner, J. Ab initio molecular dynamics for liquid metals. *Phys. Rev. B* **47**, 558–561 (1993).

[107] Kresse, G. & Furthmüller, J. Efficiency of ab-initio total energy calculations for metals and semiconductors using a plane-wave basis set. *Adv. Mater. Interfaces* **6**, 15–50 (1996).

[108] Kresse, G. & Furthmüller, J. Efficient iterative schemes for ab initio total-energy calculations using a plane-wave basis set. *Phys. Rev. B* **54**, 11169–11186 (1996).

[109] Ziesche, P., Kurth, S. & Perdew, J. P. Density functionals from LDA to GGA. *Adv. Mater. Interfaces* **11**, 122–127 (1998).

[110] Al-Hamdani, Y. S., Alfè, D. & Michaelides, A. How strongly do hydrogen and water molecules stick to carbon nanomaterials? *J. Chem. Phys.* **146**, 094701 (2017).

[111] Brandenburg, J. G. *et al.* Physisorption of water on graphene: Subchemical accuracy from many-body electronic structure methods. *J. Phys. Chem. Lett.* **10**, 358–368 (2019).

[112] Perdew, J. P., Burke, K. & Ernzerhof, M. Generalized gradient approximation made simple. *Phys. Rev. Lett.* **77**, 3865–3868 (1996).

[113] Klimeš, J., Bowler, D. R. & Michaelides, A. Van der Waals density functionals applied to solids. *Phys. Rev. B* **83** (2011).

[114] Klimeš, J. & Michaelides, A. Perspective: Advances and challenges in treating van der Waals dispersion forces in density functional theory. *J. Chem. Phys.* **137**, 120901 (2012).

[115] Kresse, G. & Joubert, D. From ultrasoft pseudopotentials to the projector augmented-wave method. *Phys. Rev. B* **59**, 1758–1775 (1999).

[116] Mathew, K., Sundararaman, R., Letchworth-Weaver, K., Arias, T. A. & Hennig, R. G. Implicit solvation model for density-functional study of nanocrystal surfaces and reaction pathways. *J. Chem. Phys.* **140**, 084106 (2014).

[117] Lespes, N. & Filhol, J.-S. Using implicit solvent in ab initio electrochemical modeling: Investigating Li/Li electrochemistry at a Li/solvent interface. *J. Chem. Theory Comput.* **11**, 3375–3382 (2015).

[118] Sakong, S., Naderian, M., Mathew, K., Hennig, R. G. & Groß, A. Density functional theory study of the electrochemical interface between a Pt electrode and an aqueous electrolyte using an implicit solvent method. *J. Chem. Phys.* **142**, 234107 (2015).

[119] Steinmann, S. N., Michel, C., Schwiedernoch, R., Filhol, J.-S. & Sautet, P. Modeling the $HCOOH/CO_2$ electrocatalytic reaction: When details are key. *ChemPhysChem* **16**, 2307–2311 (2015).

[120] Garcia-Ratés, M. & López, N. Multigrid-based methodology for implicit solvation models in periodic DFT. *J. Chem. Theory Comput.* **12**, 1331–1341 (2016).

[121] Hutter, J., Iannuzzi, M., Schiffmann, F. & VandeVondele, J. CP2K: atomistic simulations of condensed matter systems. *Wiley Interdiscip. Rev. Comput. Mol. Sci.* **4**, 15–25 (2013).

[122] VandeVondele, J. *et al.* Quickstep: Fast and accurate density functional calculations using a mixed gaussian and plane waves approach. *Comput. Phys. Commun.* **167**, 103–128 (2005).

[123] Lippert, G., Hutter, J. & Parrinello, M. A hybrid gaussian and plane wave density functional scheme. *Mol. Phys.* **92**, 477–488 (1997).

[124] VandeVondele, J. & Hutter, J. Gaussian basis sets for accurate calculations on molecular systems in gas and condensed phases. *J. Chem. Phys.* **127**, 114105 (2007).

[125] Goedecker, S., Teter, M. & Hutter, J. Separable dual-space gaussian pseudopotentials. *Phys. Rev. B* **54**, 1703–1710 (1996).

[126] Hartwigsen, C., Goedecker, S. & Hutter, J. Relativistic separable dual-space gaussian pseudopotentials from H to Rn. *Phys. Rev. B* **58**, 3641–3662 (1998).

[127] Krack, M. Pseudopotentials for for H to Kr optimized for gradient-corrected exchange-correlation functionals. *Theor. Chem. Acc.* **114**, 145–152 (2005).

[128] Grimme, S., Antony, J., Ehrlich, S. & Krieg, H. A consistent and accurate ab initio parametrization of density functional dispersion correction (DFT-d) for the 94 elements H-Pu. *J. Chem. Phys.* **132**, 154104 (2010).

[129] Grimme, S., Ehrlich, S. & Goerigk, L. Effect of the damping function in dispersion corrected density functional theory. *J. Comput. Chem.* **32**, 1456–1465 (2011).

[130] Nosé, S. A molecular dynamics method for simulations in the canonical ensemble. *Mol. Phys.* **52**, 255–268 (1984).

[131] Nosé, S. A unified formulation of the constant temperature molecular dynamics methods. *J. Chem. Phys.* **81**, 511–519 (1984).

[132] Gillan, M. J., Alfè, D. & Michaelides, A. Perspective: How good is DFT for water? *J. Chem. Phys.* **144**, 130901 (2016).

[133] Visual Molecular Dynamics, http://www.ks.uiuc.edu/research/vmd/ (2018).

[134] Humphrey, W., Dalke, A. & Schulten, K. VMD – Visual Molecular Dynamics. *J. Mol. Graph.* **14**, 33–38 (1996).

[135] Stone, J. An efficient library for parallel ray tracing and animation. *Master Thesis, Comput. Sci. Dep., Univ. of Missouri-Rolla* (1998).

[136] Delley, B. An all-electron numerical method for solving the local density functional for polyatomic molecules. *J. Chem. Phys.* **92**, 508–517 (1990).

[137] Delley, B. From molecules to solids with the DMol^3 approach. *J. Chem. Phys.* **113**, 7756–7764 (2000).

[138] Delley, B. Fast calculation of electrostatics in crystals and large molecules. *J. Phys. Chem.* **100**, 6107–6110 (1996).

[139] Reuter, K. & Scheffler, M. Composition and structure of the RuO_2 (110) surface in an O_2 and CO environment: Implications for the catalytic formation of CO_2. *Phys. Rev. B* **68** (2003).

[140] Loffreda, D. Theoretical insight of adsorption thermodynamics of multifunctional molecules on metal surfaces. *Surf. Sci.* **600**, 2103–2112 (2006).

[141] Hill, T. An introduction to statistical thermodynamics. *Addison-Wesley Series in Chemistry, Dover Publications* (1960).

[142] Gaiduk, A. P., Gygi, F. & Galli, G. Density and compressibility of liquid water and ice from first-principles simulations with hybrid functionals. *J. Phys. Chem. Lett.* **6**, 2902–2908 (2015).

[143] Iannuzzi, M., Laio, A. & Parrinello, M. Efficient exploration of reactive potential energy surfaces using Car-Parrinello molecular dynamics. *Phys. Rev. Lett.* **90** (2003).

[144] Kumar, S., Rosenberg, J. M., Bouzida, D., Swendsen, R. H. & Kollman, P. A. The weighted histogram analysis method for free-energy calculations on biomolecules. *J. Comput. Chem.* **13**, 1011–1021 (1992).

[145] Souaille, M. & Roux, B. Extension to the weighted histogram analysis method: combining umbrella sampling with free energy calculations. *Comput. Phys. Commun.* **135**, 40–57 (2001).

[146] Allen, M. P. & Tildesley, D. J. Computer simulation of liquids. *Oxford University Press* (2017).

[147] Lin, I.-C., Seitsonen, A. P., Tavernelli, I. & Rothlisberger, U. Structure and dynamics of liquid water from ab initio molecular dynamics—comparison of BLYP, PBE, and revPBE density functionals with and without van der Waals corrections. *J. Chem. Theory Comput.* **8**, 3902–3910 (2012).

[148] Bankura, A., Karmakar, A., Carnevale, V., Chandra, A. & Klein, M. L. Structure, dynamics, and spectral diffusion of water from first-principles molecular dynamics. *J. Phys. Chem. C* **118**, 29401–29411 (2014).

[149] Bonthuis, D. J., Gekle, S. & Netz, R. R. Dielectric profile of interfacial water and its effect on double-layer capacitance. *Phys. Rev. Lett.* **107**, 166102 (2011).

[150] Horinek, D. & Netz, R. R. Specific ion adsorption at hydrophobic solid surfaces. *Phys. Rev. Lett.* **99**, 226104 (2007).

[151] Gao, Y. *et al.* Toward single-layer uniform hexagonal boron nitride–graphene patchworks with zigzag linking edges. *Nano Lett.* **13**, 3439–3443 (2013).

[152] Drost, R. *et al.* Electronic states at the graphene–hexagonal boron nitride zigzag interface. *Nano Lett.* **14**, 5128–5132 (2014).

[153] Martínez, L., Andrade, R., Birgin, E. G. & Martínez, J. M. PACKMOL: A package for building initial configurations for molecular dynamics simulations. *J. Comput. Chem.* **30**, 2157–2164 (2009).

[154] Bussi, G., Donadio, D. & Parrinello, M. Canonical sampling through velocity rescaling. *J. Chem. Phys.* **126**, 014101 (2007).

[155] Klimeš, J., Bowler, D. R. & Michaelides, A. Chemical accuracy for the van der Waals density functional. *J. Phys.: Condens. Matter* **22**, 022201 (2009).

[156] The PLUMED consortium: A community effort to promote openness, transparency and reproducibility in molecular simulations. *In Revision* (2019).

[157] Tribello, G. A., Bonomi, M., Branduardi, D., Camilloni, C. & Bussi, G. PLUMED 2: New feathers for an old bird. *Comput. Phys. Commun.* **185**, 604–613 (2014).

[158] Ghaderi, N. & Peressi, M. First-principle study of hydroxyl functional groups on pristine, defected graphene, and graphene epoxide. *J. Phys. Chem. C* **114**, 21625–21630 (2010).

[159] Niyogi, S. *et al.* Chemistry of single-walled carbon nanotubes. *Acc. Chem. Res.* **35**, 1105–1113 (2002).

[160] Radha, B. *et al.* Molecular transport through capillaries made with atomic-scale precision. *Nature* **538**, 222–225 (2016).

[161] Mouterde, T. *et al.* Molecular streaming and its voltage control in ångström-scale channels. *Nature* **567**, 87–90 (2019).

[162] Chen, B., Ivanov, I., Park, J. M., Parrinello, M. & Klein, M. L. Solvation structure and mobility mechanism of OH^-: A Car-Parrinello molecular dynamics investigation of alkaline solutions. *J. Phys. Chem. B* **106**, 12006–12016 (2002).

[163] Tuckerman, M. E., Marx, D. & Parrinello, M. The nature and transport mechanism of hydrated hydroxide ions in aqueous solution. *Nature* **417**, 925–929 (2002).

[164] Asthagiri, D., Pratt, L. R., Kress, J. D. & Gomez, M. A. From The Cover: Hydration and mobility of HO-(aq). *Proc. Natl. Acad. Sci. U.S.A.* **101**, 7229–7233 (2004).

[165] Kudin, K. N. & Car, R. Why are water-hydrophobic interfaces charged? *J. Am. Chem. Soc.* **130**, 3915–3919 (2008).

[166] Mundy, C. J., Kuo, I.-F. W., Tuckerman, M. E., Lee, H.-S. & Tobias, D. J. Hydroxide anion at the air–water interface. *Chem. Phys. Lett.* **481**, 2–8 (2009).

[167] Chen, J. & Michaelides, A. Sticky when wet. *Nat. Chem.* **10**, 376–377 (2018).

[168] Baer, M. D., Kuo, I.-F. W., Tobias, D. J. & Mundy, C. J. Toward a unified picture of the water self-ions at the air–water interface: A density functional theory perspective. *J. Phys. Chem. B* **118**, 8364–8372 (2014).

[169] Mamatkulov, S. I., Allolio, C., Netz, R. R. & Bonthuis, D. J. Orientation-induced adsorption of hydrated protons at the air-water interface. *Angew. Chem., Int. Ed.* **56**, 15846–15851 (2017).

[170] Leung, K., Nielsen, I. M. B. & Kurtz, I. Ab initio molecular dynamics study of carbon dioxide and bicarbonate hydration and the nucleophilic attack of hydroxide on CO_2. *J. Phys. Chem. B* **111**, 4453–4459 (2007).

[171] Pezzotti, S., Galimberti, D. R. & Gaigeot, M.-P. 2D H-bond network as the topmost skin to the air–water interface. *J. Phys. Chem. Lett.* **8**, 3133–3141 (2017).

[172] Bocquet, L. & Charlaix, E. Nanofluidics, from bulk to interfaces. *Chem. Soc. Rev.* **39**, 1073–1095 (2010).

[173] Esfandiar, A. *et al.* Size effect in ion transport through ångström-scale slits. *Science* **358**, 511–513 (2017).

[174] Ci, L. *et al.* Atomic layers of hybridized boron nitride and graphene domains. *Nat. Mater.* **9**, 430–435 (2010).

[175] Hus, S. M. & Li, A.-P. Spatially-resolved studies on the role of defects and boundaries in electronic behavior of 2D materials. *Prog. Surf. Sci.* **92**, 176–201 (2017).

[176] Chen, S. *et al.* Designing boron nitride islands in carbon materials for efficient electrochemical synthesis of hydrogen peroxide. *J. Am. Chem. Soc.* **140**, 7851–7859 (2018).

[177] Levendorf, M. P. *et al.* Graphene and boron nitride lateral heterostructures for atomically thin circuitry. *Nature* **488**, 627–632 (2012).

[178] Kim, S. M. *et al.* Synthesis of patched or stacked graphene and hBN flakes: A route to hybrid structure discovery. *Nano Lett.* **13**, 933–941 (2013).

[179] Han, G. H. *et al.* Continuous growth of hexagonal graphene and boron nitride in-plane heterostructures by atmospheric pressure chemical vapor deposition. *ACS Nano* **7**, 10129–10138 (2013).

[180] Liu, L. *et al.* Heteroepitaxial growth of two-dimensional hexagonal boron nitride templated by graphene edges. *Science* **343**, 163–167 (2014).

[181] Zhuang, P. *et al.* Growth of lateral graphene/h-BN heterostructure on copper foils by chemical vapor deposition. *Nanotechnology* **30**, 03LT01 (2018).

[182] Sutter, P., Cortes, R., Lahiri, J. & Sutter, E. Interface formation in monolayer graphene-boron nitride heterostructures. *Nano Lett.* **12**, 4869–4874 (2012).

[183] Sutter, P., Huang, Y. & Sutter, E. Nanoscale integration of two-dimensional materials by lateral heteroepitaxy. *Nano Lett.* **14**, 4846–4851 (2014).

[184] Liu, M. *et al.* Quasi-freestanding monolayer heterostructure of graphene and hexagonal boron nitride on Ir(111) with a zigzag boundary. *Nano Lett.* **14**, 6342–6347 (2014).

[185] Petrović, M., von Hoegen, M. H. & zu Heringdorf, F.-J. M. Lateral heterostructures of hexagonal boron nitride and graphene: BCN alloy formation and microstructuring mechanism. *Appl. Surf. Sci.* **455**, 1086–1094 (2018).

[186] Nguyen, T. H. *et al.* Microscopic insight into the single step growth of in-plane heterostructures between graphene and hexagonal boron nitride. *Adv. Mater. Interfaces* **12**, 675–682 (2019).

[187] Zhang, S., Li, J., Wu, H., Li, X. & Guo, W. Direct synthesizing in-plane heterostructures of graphene and hexagonal boron nitride in designed pattern. *Adv. Mater. Interfaces* **5**, 1800208 (2018).

[188] Sun, Q., Sun, C., Du, A., Dou, S. & Li, Z. In-plane graphene/boron-nitride heterostructures as an efficient metal-free electrocatalyst for the oxygen reduction reaction. *Nanoscale* **8**, 14084–14091 (2016).

[189] Lu, J. *et al.* Order–disorder transition in a two-dimensional boron–carbon–nitride alloy. *Nat. Comm.* **4** (2013).

[190] Schlesinger, I., Kuchuk, K. & Sivan, U. An ultra-low noise optical head for liquid environment atomic force microscopy. *Rev. Sci. Instrum.* **86**, 083705 (2015).

[191] Kuchuk, K. & Sivan, U. Hydration structure of a single DNA molecule revealed by frequency-modulation atomic force microscopy. *Nano Lett.* **18**, 2733–2737 (2018).

[192] Mendonça, B. H. S., Ternes, P., Salcedo, E., de Oliveira, A. B. & Barbosa, M. C. Direct observation of water mediated single proton transport between hBN surface defects. **arXiv:1811.10490v2** (2018).

[193] da Silva, L. B. Structural and dynamical properties of water confined in carbon nanotubes. *J. Nanostructure Chem.* **4** (2014).

[194] Köhler, M. H. & da Silva, L. B. Size effects and the role of density on the viscosity of water confined in carbon nanotubes. *Chem. Phys. Lett.* **645**, 38–41 (2016).

[195] Köhler, M. H., Bordin, J. R., da Silva, L. B. & Barbosa, M. C. Structure and dynamics of water inside hydrophobic and hydrophilic nanotubes. *Physica A Stat. Mech. Appl.* **490**, 331–337 (2018).

[196] Nicholls, W. D., Borg, M. K., Lockerby, D. A. & Reese, J. M. Water transport through (7,7) carbon nanotubes of different lengths using molecular dynamics. *Microfluid. Nanofluid.* **12**, 257–264 (2011).

[197] Alexiadis, A. & Kassinos, S. Molecular simulation of water in carbon nanotubes. *Chem. Rev.* **108**, 5014–5034 (2008).

[198] Werder, T., Walther, J. H., Jaffe, R. L., Halicioglu, T. & Koumoutsakos, P. On the water-carbon interaction for use in molecular dynamics simulations of graphite and carbon nanotubes. *J. Phys. Chem. B* **107**, 1345–1352 (2003).

[199] Dellago, C., Naor, M. M. & Hummer, G. Proton transport through water-filled carbon nanotubes. *Phys. Rev. Lett.* **90** (2003).

[200] II, J. K. C. & Paddison, S. J. Ab initio molecular dynamics simulations of water and an excess proton in water confined in carbon nanotubes. *Phys. Chem. Chem. Phys.* **16**, 17756 (2014).

[201] Mann, D. J. & Halls, M. D. Water alignment and proton conduction inside carbon nanotubes. *Phys. Rev. Lett.* **90** (2003).

[202] Chen, J., Li, X.-Z., Zhang, Q., Michaelides, A. & Wang, E. Nature of proton transport in a water-filled carbon nanotube and in liquid water. *Phys. Chem. Chem. Phys.* **15**, 6344 (2013).

[203] II, J. K. C., Habenicht, B. F. & Paddison, S. J. Ab initio molecular dynamics simulations of aqueous triflic acid confined in carbon nanotubes. *J. Nanostructure Chem.* **16**, 16465–16479 (2014).

[204] Habenicht, B. F. & Paddison, S. J. Ab initio simulations of the effects of nanoscale confinement on proton transfer in hydrophobic environments. *J. Phys. Chem. B* **115**, 10826–10835 (2011).

[205] Sirkin, Y. A. P., Hassanali, A. & Scherlis, D. A. One-dimensional confinement inhibits water dissociation in carbon nanotubes. *J. Phys. Chem. Lett.* **9**, 5029–5033 (2018).

[206] Rossi, M., Ceriotti, M. & Manolopoulos, D. E. Nuclear quantum effects in H+

and OH⁻ diffusion along confined water wires. *J. Phys. Chem. Lett.* **7**, 3001–3007 (2016).

[207] Sulpizi, M. & Sprik, M. Acidity constants from DFT-based molecular dynamics simulations. *J. Phys.: Condens. Matter* **22**, 284116 (2010).

[208] Mucha, M. *et al.* Unified molecular picture of the surfaces of aqueous acid, base, and salt solutions. *J. Phys. Chem. B* **109**, 7617–7623 (2005).

[209] Levering, L. M., Sierra-Hernández, M. R. & Allen, H. C. Observation of hydronium ions at the air-aqueous acid interface: Vibrational spectroscopic studies of aqueous HCl, HBr, and HI. *J. Phys. Chem. C* **111**, 8814–8826 (2007).

[210] Vácha, R., Horinek, D., Berkowitz, M. L. & Jungwirth, P. Hydronium and hydroxide at the interface between water and hydrophobic media. *Phys. Chem. Chem. Phys.* **10**, 4975 (2008).

[211] Chejanovsky, N. *et al.* Structural attributes and photodynamics of visible spectrum quantum emitters in hexagonal boron nitride. *Nano Lett.* **16**, 7037–7045 (2016).

[212] Exarhos, A. L., Hopper, D. A., Grote, R. R., Alkauskas, A. & Bassett, L. C. Optical signatures of quantum emitters in suspended hexagonal boron nitride. *ACS Nano* **11**, 3328–3336 (2017).

[213] Jungwirth, N. R. & Fuchs, G. D. Optical absorption and emission mechanisms of single defects in hexagonal boron nitride. *Phys. Rev. Lett.* **119** (2017).

[214] Feng, J. *et al.* Imaging of optically active defects with nanometer resolution. *Nano Lett.* **18**, 1739–1744 (2018).

[215] Comtet, J. *et al.* Wide-field spectral super-resolution mapping of optically active defects in hexagonal boron nitride. *Nano Lett.* **19**, 2516–2523 (2019).

[216] Weston, L., Wickramaratne, D., Mackoit, M., Alkauskas, A. & de Walle, C. G. V. Native point defects and impurities in hexagonal boron nitride. *Phys. Rev. B* **97** (2018).

Appendix

CP2K Input File For Biased Trajectories of Chapter 4

Typical example of a CP2K input file used for biased MD trajectories.

```
# CP2K input file example"
@SET SYSTEM     system
@SET DATA_PATH /home/cp2k-data/
&FORCE_EVAL
  METHOD Quickstep
  &DFT
    CHARGE -1
    BASIS_SET_FILE_NAME ${DATA_PATH}/BASIS_SETS
    POTENTIAL_FILE_NAME ${DATA_PATH}/GTH_POTENTIALS
    &MGRID
      CUTOFF 600
    &END MGRID
    &QS
      EPS_DEFAULT 1.0E-14
      MAP_CONSISTENT TRUE
      EXTRAPOLATION ASPC
      EXTRAPOLATION_ORDER 4
    &END QS
    &PRINT
```

```
    &MULLIKEN

      FILENAME ${SYSTEM}

      &EACH

       MD 10

      &END EACH

     &END MULLIKEN

   &END PRINT

   &SCF

     MAX_SCF 10

     SCF_GUESS RESTART

     EPS_SCF 1.0E-7

     &OUTER_SCF

       EPS_SCF 1.0E-7

       MAX_SCF 1000

     &END OUTER_SCF

     &OT ON

       MINIMIZER DIIS

       N_DIIS 5

     &END OT

   &END SCF

   &XC

     &XC_FUNCTIONAL PBE

     &END XC_FUNCTIONAL

     &vdW_POTENTIAL

         DISPERSION_FUNCTIONAL PAIR_POTENTIAL

         &PAIR_POTENTIAL

            TYPE DFTD3

            CALCULATE_C9_TERM .TRUE.

            REFERENCE_C9_TERM .TRUE.
```

```
            LONG_RANGE_CORRECTION .TRUE.

            PARAMETER_FILE_NAME ${DATA_PATH}/dftd3.dat

            VERBOSE_OUTPUT .TRUE.

            REFERENCE_FUNCTIONAL PBE

            R_CUTOFF [angstrom] 11.0

            EPS_CN 1.0E-6

          &END PAIR_POTENTIAL

      &END vdW_POTENTIAL

      &XC_GRID

        XC_SMOOTH_RHO NN50

        XC_DERIV NN50_SMOOTH

      &END

    &END XC

  &END DFT

  &SUBSYS

    &CELL

      ABC [angstrom] 12.83 12.35 21.0

    &END CELL

    &TOPOLOGY

      COORD_FILE_FORMAT xyz

      COORD_FILE_NAME ${SYSTEM}.xyz

    &END TOPOLOGY

      &COLVAR

        &COORDINATION

         ATOMS_FROM 122

         KINDS_TO H

  R0 [angstrom] 1.2

  NN 12

  ND 20
```

```
          &END COORDINATION

        &END COLVAR

      &KIND H

        BASIS_SET DZVP-MOLOPT-SR-GTH

        POTENTIAL GTH-PBE-q1

        MASS 2

      &END KIND

      &KIND O

        BASIS_SET DZVP-MOLOPT-SR-GTH

        POTENTIAL GTH-PBE-q6

      &END KIND

      &KIND B

        BASIS_SET DZVP-MOLOPT-SR-GTH

        POTENTIAL GTH-PBE-q3

      &END KIND

      &KIND N

        BASIS_SET DZVP-MOLOPT-SR-GTH

        POTENTIAL GTH-PBE-q5

      &END KIND

      &KIND C

       BASIS_SET DZVP-MOLOPT-SR-GTH

       POTENTIAL GTH-PBE-q4

      &END KIND

    &END SUBSYS

  &END FORCE_EVAL

  &GLOBAL

    PROJECT ${SYSTEM}

    RUN_TYPE MD

    PRINT_LEVEL LOW
```

```
   WALLTIME  82800

&END GLOBAL

&MOTION

   &MD

      ENSEMBLE NVT

      STEPS 10000

      TIMESTEP 0.5

      TEMPERATURE 323.15

      &THERMOSTAT

         &NOSE

            LENGTH 4

            YOSHIDA 9

            TIMECON [fs] 500.0

            MULTIPLE_TIME_STEPS 2

         &END NOSE

      &END THERMOSTAT

   &END MD

   &CONSTRAINT

      &FIXED_ATOMS

         COMPONENTS_TO_FIX XYZ

         LIST 122 43

      &END FIXED_ATOMS

     &COLLECTIVE

      COLVAR 1

      TARGET 1

      INTERMOLECULAR .TRUE.

      &RESTRAINT

       K 0.05

      &END RESTRAINT
```

```
      &END COLLECTIVE
    &END CONSTRAINT
   &PRINT
     &TRAJECTORY  SILENT
       FILENAME =${SYSTEM}-1.xyz
       &EACH
         MD 1
       &END EACH
     &END TRAJECTORY
     &VELOCITIES  SILENT
       FILENAME =${SYSTEM}-1.vel
       &EACH
         MD 1
       &END EACH
     &END VELOCITIES
     &FORCES  SILENT
       FILENAME =${SYSTEM}-1.force
       &EACH
         MD 1
       &END EACH
     &END FORCES
     &RESTART
       FILENAME =${SYSTEM}-1.restart
       &EACH
         MD 1
       &END EACH
     &END RESTART
   &END PRINT
&END MOTION
```

CP2K Input File For Biased Trajectories of Chapter 5

Typical example of a CP2K input file used for biased MD trajectories.

```
@SET SYSTEM system
@SET DATA_PATH /home/cp2k-data
&FORCE_EVAL
  METHOD Quickstep
  &DFT
    BASIS_SET_FILE_NAME ${DATA_PATH}/BASIS_SETS
    POTENTIAL_FILE_NAME ${DATA_PATH}/GTH_POTENTIALS
    &MGRID
      CUTOFF 600
    &END MGRID
    &QS
      EPS_DEFAULT 1.0E-14
      MAP_CONSISTENT TRUE
      EXTRAPOLATION ASPC
      EXTRAPOLATION_ORDER 4
    &END QS
    &PRINT
     &MULLIKEN
      FILENAME =${SYSTEM}-1.mulliken
      &EACH
       MD 1
      &END EACH
     &END MULLIKEN
    &END PRINT
    &SCF
      MAX_SCF 10
      SCF_GUESS RESTART
```

```
    EPS_SCF 1.0E-7

    &OUTER_SCF

      EPS_SCF 1.0E-7

      MAX_SCF 1000

    &END OUTER_SCF

    &OT ON

      MINIMIZER DIIS

      N_DIIS 5

    &END OT

  &END SCF

  &XC

    &XC_FUNCTIONAL PBE

    &END XC_FUNCTIONAL

    &vdW_POTENTIAL

      DISPERSION_FUNCTIONAL PAIR_POTENTIAL

      &PAIR_POTENTIAL

        TYPE DFTD3

        CALCULATE_C9_TERM .TRUE.

        REFERENCE_C9_TERM .TRUE.

        LONG_RANGE_CORRECTION .TRUE.

        PARAMETER_FILE_NAME ${DATA_PATH}/dftd3.dat

        VERBOSE_OUTPUT .TRUE.

        REFERENCE_FUNCTIONAL PBE

        R_CUTOFF [angstrom] 11.0

        EPS_CN 1.0E-6

      &END PAIR_POTENTIAL

    &END vdW_POTENTIAL

    &XC_GRID

      XC_SMOOTH_RHO NN50
```

```
      XC_DERIV NN50_SMOOTH

    &END

  &END XC

&END DFT

&SUBSYS

  &CELL

    ABC [angstrom] 14.766 25.5755 21.0

  &END CELL

  &TOPOLOGY

    COORD_FILE_FORMAT xyz

    COORD_FILE_NAME coordinate.xyz

  &END TOPOLOGY

  &COLVAR

   &DISTANCE

    ATOMS 16 17

   &END DISTANCE

  &END COLVAR

  &COLVAR

   &DISTANCE

    ATOMS 16 18

   &END DISTANCE

  &END COLVAR

  &KIND H

    BASIS_SET DZVP-MOLOPT-SR-GTH

    POTENTIAL GTH-PBE-q1

    MASS 2

  &END KIND

  &KIND O

    BASIS_SET DZVP-MOLOPT-SR-GTH
```

```
          POTENTIAL GTH-PBE-q6

      &END KIND

      &KIND B

        BASIS_SET DZVP-MOLOPT-SR-GTH

        POTENTIAL GTH-PBE-q3

      &END KIND

      &KIND N

        BASIS_SET DZVP-MOLOPT-SR-GTH

        POTENTIAL GTH-PBE-q5

      &END KIND

      &KIND K

       BASIS_SET DZVP-MOLOPT-SR-GTH

       POTENTIAL GTH-PBE-q9

      &END KIND

      &KIND C

       BASIS_SET DZVP-MOLOPT-SR-GTH

       POTENTIAL GTH-PBE-q4

      &END KIND

   &END SUBSYS

&END FORCE_EVAL

&GLOBAL

   PROJECT ${SYSTEM}

   RUN_TYPE MD

   PRINT_LEVEL LOW

   WALLTIME  1500

&END GLOBAL

&MOTION

   &FREE_ENERGY

      &METADYN
```

```
            USE_PLUMED .TRUE.

            PLUMED_INPUT_FILE ./plumed.in

      &END METADYN

  &END FREE_ENERGY

   &MD

      ENSEMBLE NVT

      STEPS 1000

      TIMESTEP 0.5

      TEMPERATURE 323.15

      &THERMOSTAT

         TYPE NOSE

         REGION GLOBAL

         &NOSE

            TIMECON 500

LENGTH 4

YOSHIDA 9

MULTIPLE_TIME_STEPS 2

         &END NOSE

      &END THERMOSTAT

   &END MD

   &CONSTRAINT

    &COLLECTIVE

      COLVAR 1

      TARGET [angstrom] 1.00

      INTERMOLECULAR .TRUE.

      &RESTRAINT

       K 0.025

      &END RESTRAINT

     &END COLLECTIVE
```

```
   &COLLECTIVE

    COLVAR 2

    TARGET [angstrom] 1.00

    INTERMOLECULAR .TRUE.

    &RESTRAINT

     K 0.025

    &END RESTRAINT

   &END COLLECTIVE

  &END CONSTRAINT

 &PRINT

  &TRAJECTORY  SILENT

    FILENAME =${SYSTEM}-1.xyz

    &EACH

      MD 1

    &END EACH

  &END TRAJECTORY

  &VELOCITIES  SILENT

    FILENAME =${SYSTEM}-1.vel

    &EACH

      MD 1

    &END EACH

  &END VELOCITIES

  &FORCES  SILENT

    FILENAME =${SYSTEM}-1.force

    &EACH

      MD 1

    &END EACH

  &END FORCES

  &RESTART
```

```
      FILENAME =${SYSTEM}-1.restart

        &EACH

          MD 1

        &END EACH

      &END RESTART

    &END PRINT

&END MOTION
```

PLUMED Input File For Biased Trajectories of Chapter 5

Typical PLUMED input file used for biased MD trajectories in combination with the preceding CP2K input file. Only one example of LOWER_WALL definition is included instead of the thousands used in the simulations.

```
surface_atoms: GROUP ATOMS=586-729

O: GROUP ATOMS=1

DISTANCES GROUPA=surface_atoms GROUPB=O MIN={BETA=500.0} LABEL=d_O_surface

RESTRAINT ...

LABEL=d_O_surface_restraint

ARG=d_O_surface.min AT=1.6 KAPPA=500.0

... RESTRAINT

PRINT ARG=d_O_surface.min,d_O_surface_restraint.bias FILE=plumed.out


DISTANCE ATOMS=4,586  LABEL=d4_586

LOWER_WALLS ARG =d4_586 AT=2.0 KAPPA=500.0 EXP=2 EPS=1 OFFSET=0 LABEL=lwall_1
```

VASP Input File For Static DFT Calculations of Chapter 5

Typical VASP input file used for static DFT calculations in implicit water.

```
ISTART = 0

ICHARG = 2

LREAL = Auto

PREC  = Accurate

LSOL = .TRUE.

ENCUT = 800

EDIFF = 1e-6

NELM  = 250

ALGO  = NORMAL

NSW = 101

IBRION = 2

EDIFFG = -0.05

GGA = OR

LUSE_VDW = .TRUE.

AGGAC = 0.0000

ISMEAR = 0

SIGMA  = 0.025
```

Funding